Enhancement of nonlinear effects using silicon plasmonic structures

Jihua Zhang

THESE DE DOCTORAT
DE L'UNIVERSITE PARIS-SACLAY,
préparée à l'Université Paris-Sud

ÉCOLE DOCTORALE N°575
Electrical, Optical, Bio – physics and Engineering (EOBE)

Spécialité de doctorat : Physique

Par

M. Jihua ZHANG

Enhancement of nonlinear effects using silicon plasmonic structures

Numéro de NNT : 2015SACLS171

Thèse présentée et soutenue à Orsay, le 02 décembre 2015 :

Composition du Jury :

- M. Guillaume Bachelier, Maître de conférences HDR, Université Joseph Fourier, Rapporteur
- M. Gilles Renversez, Professeur, Université d'Aix-Marseille, Rapporteur
- M. Alexandre Bouhelier, DR-CNRS, Université Bourgogne Franche-Comté, Président du jury
- Mme. Béatrice Dagens, DR-CNRS, Université Paris-Sud, Examinateur
- M. Eric Cassan, Professeur, Université Paris-Sud, Directeur de thèse

université PARIS-SACLAY
ÉCOLE DOCTORALE
Physique et ingénierie : électrons, photons, sciences du vivant (EOBE)

Titre : Structures plasmoniques pour le renforcement des effets nonlinaires et la réalisation de fonctions tout-optiques en photoniques sur silicium

Mots clés : Photonique silicium, plasmonique, optique nonlinéaire

Résumé :

L'augmentation des flux d'information sur puce conduit l'électronique intégrée à un certain nombre de limitations, liées en particulier à la saturation des débits binaires transmissibles entre blocs et cœurs et au niveau excessif de puissance dissipée. Dans ce contexte, la photonique silicium a été proposée il y a plusieurs années comme une solution intéressante pour lever certains verrous. Ce domaine, qui a connu un intérêt marqué depuis, repose sur le développement de liens optiques sur puce, donc sur le développement de toutes les structures nécessaires pour l'émission, le guidage, la modulation, et la détection des signaux optiques. Au stade actuel, les progrès ont été spectaculaires mais des difficultés demeurent : d'une part, la puissance consommée par les composants optoélectroniques, en particulier de modulation, se situe toujours au-dessus des niveaux requis par les applications ; d'autre part, la taille des composants optiques intégrées classiques ne peut pas être miniaturisée en-dessous de la limite de diffraction (de l'ordre de 250nm dans les cas usuels de la photonique silicium, dans la fenêtre des longueurs d'onde télécoms λ=1,55 µm), ce qui ne permet pas d'envisager une co-intégration poussée de l'optique avec l'électronique CMOS.

Dans cette thèse, nous avons exploré les potentialités de l'utilisation de matériaux organiques non-linéaires au sein de structures métalliques pour la réalisation de guides d'ondes plasmoniques nonlinéaires. Les propriétés de la plasmonique autorisant la réalisation de structures sub-longueur d'onde à confinement extrême du champ électromagnétique, les composants qui en découlent sont caractérisés par un renforcement significatif des effets optiques non-linéaires et leur co-intégration avec l'électronique devient envisageable en terme de compacité et d'encombrement.

Nous avons développé une approche basée sur la théorie des modes couplées applicable à des guides à pertes (absorption par les métaux) et, couplées à des calculs par éléments finis, nous l'avons appliquée à l'exploration des plusieurs effets. Deux types de guides ont été considérés, guides plasmoniques et guides plasmoniques hybrides. Les phénomènes de génération de seconde harmonique et de rectification optique (assistée électriquement ou pas) ont été étudiés principalement ; les compromis entre pertes de propagation (par absorption) et confinement du champ électromagnétique ont été explorés et l'ensemble a conduit à proposer plusieurs configurations caractérisées par des longueurs d'interaction de quelques dizaines de µm typiquement et des efficacités (de conversion de longueur d'onde, de rectification, etc) se situant au-delà de l'état de l'art actuel.

Ces propositions théoriques ont été complétées par un volet expérimental, concrétisé par la fabrication de structures plasmoniques, et qui a permis de valider la possibilité d'une injection efficace de la lumière depuis une fibre optique vers des guides plasmoniques très sub-longueur d'onde.

Université Paris-Saclay
Espace Technologique / Immeuble Discovery
Route de l'Orme aux Merisiers RD 128 / 91190 Saint-Aubin, France

Acknowledgement

First, I would like to thank my supervisors Prof. Eric Cassan and Prof. Xinliang Zhang for providing me with the opportunity to complete my joint PhD thesis at University Paris-Sud and Huazhong University of Science and Technology. Prof. Eric Cassan is the most easy-going professor I have even seen. He always amazes me with his endless energy, passion, and knowledge. Prof. Xinliang Zhang has been supportive and has given me the freedom to pursue various directions without objection. They were and remains my best role model for a scientist, mentor, and teacher.

I would also like to thank my committee members, Prof. Guillaume Bachelier. Prof. Gilles Renversez, Prof. Alexandre Bouhelier and Prof. Béatrice Dagens for serving as my committee members. Thank you for letting my defense be an enjoyable moment, and for your brilliant comments and suggestions.

I am also very grateful to all the professors in the two labs Prof. Laurent Vivien, Prof. Delphine Marris-Morini, Prof. Jianji Dong, Prof. Yu Yu and Prof. Lei Shi for their help, scientific advice and insightful discussions. I want to thank present and past group members for the good atmosphere they have built in the lab and good time we have shared together. Thanks to Ping Zhao and Yuan Yu for helping me get used to the graduate life and for sharing their knowledge.

A special thanks to my family for their unconditional support and love. Words cannot express how grateful I am to my mother ShuZhen Zhang, my father Shiyun Zhang and my brother Jixin Zhang for all of the sacrifices that they have made for me. I also want to thank my girlfriend Mengwan Lv for her faith, support and love.

Jihua Zhang

December 2015

Orsay, France

Abstract

With the rapid increasing bandwidth of data transmission and signal processing, integrated electronics encounters strong challenges due to its intrinsic bandwidth bottleneck and large power consumption at high data rate. Silicon photonics provides a low-cost solution to overcome these challenges by replacing some parts of the original electronic integrated circuits with photonic integrated circuits. After a decade of development, silicon photonics is now the most active discipline and most promising platform within the field of integrated optics. However, in the process of further development, new stumbling blocks emerge. The sizes of photonic devices are restricted by the diffraction limit and thus result in a strong mismatch between photonic and electronic components in their co-integration. In addition, lack of second-order nonlinearity and existence of free carrier effects in silicon tend to limit the versatility and operating speed of nonlinear optical signal processing, which plays a key role in multiple photonic functionalities.

Plasmonics is a good candidate to overcome the first obstacle due to its ability to confine the optical field into nanoscale beyond the diffraction limit. Moreover, the localized strong field enhancement in plasmonic structures enhances interaction of light and matter, which is promising for enhancing the efficiency and reducing the power consumption in nonlinear applications. For the second limit, organic materials with large nonlinear susceptibility and free of carrier effects have attracted a growing attention in the last years and their integration on silicon have been proposed to be an efficient silicon organic hybrid platform.

In this dissertation, we combine the plasmonic and organic technologies onto the silicon photonics platform to investigate silicon plasmonic organic structures and explore the nonlinear effects induced in them. Silicon plasmonic organic structures, which combine the advantages of silicon with the ultra-compact and strong-field performance of plasmonics and the ultrafast and large-nonlinearity property of organic

materials, have great potentials for nonlinear integrated optics.

A full-vectorial nonlinear coupled-wave equation model valid for lossy plasmonic waveguides is proposed and then used to analyze nonlinear effects in silicon plasmonic waveguides. This dissertation addresses the use of two kinds of plasmonic waveguides: plasmonic slot waveguides (PSW) and hybrid plasmonic waveguides (HPW).

Specifically, an enhanced second harmonic generation (SHG) is proposed in the PSW. A normalized efficiency up to 10^5 $W^{-1}cm^{-2}$ is predicted, which is four orders of magnitude higher than those previously reported. Then, by applying two electrodes onto the two sides of PSW, the SHG process can be controlled by the voltage, which is proposed to be a new mechanism for high-speed electro-optic modulation. Another nonlinear effect investigated in PSW is the optical rectification (OR) effect, through which an electrical signal is generated between the two metal slabs when an intensity modulated optical signal is injected into the PSW. This efficient OR process supports flat response for a wide range of wavelength, which can be applied for the realization of high-speed broadband optical detection and demodulation.

The enhanced mid-to-near-infrared SHG in HPW is also explored. The SHG yield is as large as 8.8% for a pumping power of 100 mW and a short length of 120 μm. Then, by utilizing the resonant effect in a microring, the efficiency is further enhanced by two orders of magnitude. This provides a potential route for realizing efficient frequency conversion between mid-infrared and near-infrared wavebands on a chip. Besides, efficient optical parameter amplification (OPA) is also studied in a symmetric HPW. Based on the OPA, phase regeneration of phase-shift keying signals is then theoretically proposed.

The design, fabrication and measurement of PSWs are also described. The fabricated PSW have good performance in terms of loss. By spin-coating the commercial available second order nonlinear polymer, the nonlinear response of the PSW is under testing at the present writing time.

Contents

List of Figures

List of Tables

List of Publications

Journals

1. H. L. Zhou, J. J. Dong, Y. F. Zhou, **J. H. Zhang**, M. Liu, X. L. Zhang, "Designing Appointed and Multiple Focuses With Plasmonic Vortex Lenses, " Photonics Journal, IEEE 7(4) 1-7 (2015).

2. H. L. Zhou, Y. F. Zhou, **J. H. Zhang**, and J. J. Dong, "Double-Slit and Square-Slit Interferences With Surface Plasmon Polaritons Modulated by Orbital Angular Momentum Beams," Photonics Journal, IEEE 7(2), 1-7 (2015).

3. Z. Q. Wang, L. Shi, X. B. Xu, **J. H. Zhang**, J. L. Zhang, and X. L. Zhang, "Optical nonreciprocity with large bandwidth in asymmetric hybrid slot waveguide coupler," Optics Express 23 (3), 3690-3698 (2015).

4. K. S. Chen, J. Hou, Z. Y. Huang, T. Cao, **J. H. Zhang**, Y. Yu, and X. L. Zhang, "All-optical 1st- and 2nd-order differential equation solvers with large tuning ranges using Fabry-Pérot semiconductor optical amplifiers," Optics Express 23(3), 3784-3794 (2015).

5. **J. H. Zhang**, L. Shi, Y. L. Wang, E. Cassan, and X. L. Zhang, "On-chip high-speed optical detection based on an optical rectification scheme in silicon plasmonic platform," Optics Express 22(22), 27504-27514 (2014).

6. **J. H. Zhang**, E. Cassan, and X. L. Zhang, "Enhanced mid-to-near-infrared second harmonic generation in silicon plasmonic microring resonators with low pump power," Photonics Research 2(5), 143-149 (2014).

7. **J. H. Zhang**, E. Cassan, and X. L. Zhang, "Electrically controlled second-harmonic generation in silicon-compatible plasmonic slot waveguides: a new modulation scheme," Optics Letters 39(13), 4001-4004 (2014).

8. **J. H. Zhang**, E. Cassan, and X. L. Zhang, "Wideband and Compact TE-Pass/TM-Stop Polarizer Based on a Hybrid Plasmonic Bragg Grating for Silicon Photonics," Lightwave Technology, Journal of 32(7), 1383-1386 (2014).

9. **J. H. Zhang**, E. Cassan, and X. L. Zhang, "Efficient second harmonic generation from mid-infrared to near-infrared regions in silicon-organic hybrid plasmonic waveguides with small fabrication-error sensitivity and a large bandwidth," Optics Letters 38(12), 2089-2091 (2013).

10. **J. H. Zhang**, P. Zhao, E. Cassan, and X. L. Zhang, "Phase regeneration of phase-shift keying signals in highly nonlinear hybrid plasmonic waveguides," Optics Letters 38(6), 848-850 (2013).

11. **J. H. Zhang**, E. Cassan, D. S. Gao, and X. L. Zhang, "Highly efficient phase-matched second harmonic generation using an asymmetric plasmonic slot waveguide configuration in hybrid polymer-silicon photonics," Optics Express 21(12), 14876-14887 (2013).

12. P. Zhao, **J. H. Zhang**, Y. Yu, J. J. Dong, L. Shi, Y. Liu, and X. L. Zhang, “In-line polarization-dependent microfiber interferometers and their applications in UWB signal generation,” Optics Express 21(7), 8231-8239 (2013).

13. P. Zhao, **J. H. Zhang**, G. H. Wang, M. Jiang, P. P. Shum, X. L. Zhang, “Longitudinal coupling effect in microfiber Bragg gratings,” Optics Communications 285(23), 4655-4659 (2012).

14. P. Zhao, Y. H. Li, **J. H. Zhang**, L. Shi, and X. L. Zhang, “Nanohole induced microfiber Bragg gratings,” Optics Express 20(27), 28625-28630 (2012).

Conferences

1. **J. H. Zhang**, E. Cassan, and X. L. Zhang, “Enhanced mid-to-near-infrared second harmonic generation in silicon-organic hybrid plasmonic microring resonators,”

Conference on Lasers and Electro-Optics (CLEO) 2014, Paper: JTh2A.46.

2. **J. H. Zhang**, X. L. Zhang, and E. Cassan, "High-yield second-harmonic generation from mid-infrared to near-infrared regions in silicon-organic hybrid plasmonic waveguides," in Proc. SPIE 9136, Nonlinear Optics and Its Applications VIII and Quantum Optics III (Brussels, 2014), pp. 91360D-91360D-6.

3. **J. H. Zhang**, E. Cassan, and X. L. Zhang, "Efficient mid-to-near-infrared second harmonic generation based on silicon-organic hybrid plasmonic waveguides," Asia Communications and Photonics Conference and Exhibition (ACP) 2013, Paper: 1752414.

4. **J. H. Zhang**, P. Zhao, E. Cassan, and X. L. Zhang, "Proposal for phase regeneration of phase-shift keying signals in nonlinear hybrid plasmonic waveguides," International Photonics and OptoElectronics Meetings (POEM) N3 2013, Paper: NSu1B.4.

5. P. Zhao, **J. H. Zhang**, Z. Wu, and X. L. Zhang, "Model of Bragg grating written in subwavelength-diameter fiber taper," Asia Communications and Photonics Conference and Exhibition (ACP) 2011, Paper: 830720.

List of Abbreviations

AC	Alternating current
CMOS	Complementary metal-oxide semiconductor
CSHG	Conventional second harmonic generation
CW	Continuous wave
DC	Direct current
EBE	Electron beam evaporation
EBL	Electron beam lithography
ECSHG	Electrically controlled second harmonic generation
EFISHG	Electrical field induced second harmonic generation
EO	Electro-optic
FCA	Free carrier absorption
FCD	Free carrier dispersion
FDTD	Finite different time domain
FF	Fundamental frequency
FWM	Four wave mixing
HPW	Hybrid plasmonic waveguide
ICPRIE	Inductively coupled plasma reactive ion etching
LRSPP	Long-range surface plasmon polariton
MIR	Mid-infrared
MPM	Mode phase matching
MRR	Microring resonator
MSM	Metal-silicon-metal
NCC	Nonlinear coupling coefficient
NCE	Nonlinear coupled-wave equation
NIR	Near-infrared
NP	Nonlinear polymer

OF	Optical frequency
OPA	Optical parameter amplification
OR	Optical rectification
ORPD	Optical rectification based photodetector
PECVD	Plasma enhanced chemical vapor deposition
PMC	Phase matching condition
POH	Plasmonic organic hybrid
PSK	Phase shift keying
PSW	Plasmonic slot waveguide
PW	Pump wavelength
QPM	Quasi phase matching
RF	Radio frequency
RI	Refractive index
SEM	scanning electron microscope
SHF	Second harmonic frequency
SHG	Second harmonic generation
SHPW	Symmetric hybrid plasmonic waveguide
SOH	Silicon organic hybrid
SOHPMR	Silicon-organic hybrid plasmonic microring resonator
SOI	Silicon-on-insulator
SOPHW	Silicon-organic hybrid plasmonic waveguide
SP	Surface plasmon
SPD	Semiconductor photodetector
SPP	Surface plasmon polariton
SSW	Silicon slot waveguide
SW	Signal wavelength
TM	Transverse magnetic
TPA	Two photon absorption

Chapter 1

Introduction

Today, with the rapid development of information technologies, the capacity of global internet is becoming larger and larger. According to the Cisco Visual Networking Index Global Forecast, global IP traffic has increased fivefold over the past five years, and will increase threefold over the next five years. As shown in Fig. 1.1, overall IP traffic is expected to grow to 168 exabytes per month by 2019, up from 59.9 exabytes per month in 2014. This ever-increasing bandwidth requires exponential increases in communication bandwidth at all levels of the system and becomes a big challenge to the conventional electronic circuits due to its intrinsic bandwidth bottleneck and large power consumption at high data rate. At high bit rates of 10 Gbits/s and higher, the circuit's alternating current characteristics begin to dominate the impedance, inductance, and conductance of the electric line, severely distorting the signal. Meanwhile, electric signal attenuation and power dissipation rise dramatically with higher data rate. To deal with the increasing bandwidth requirement of future data communication networks, optical circuits have been widely accepted as a viable alternative owing to their strengths such as low loss and near infinite optical bandwidth.

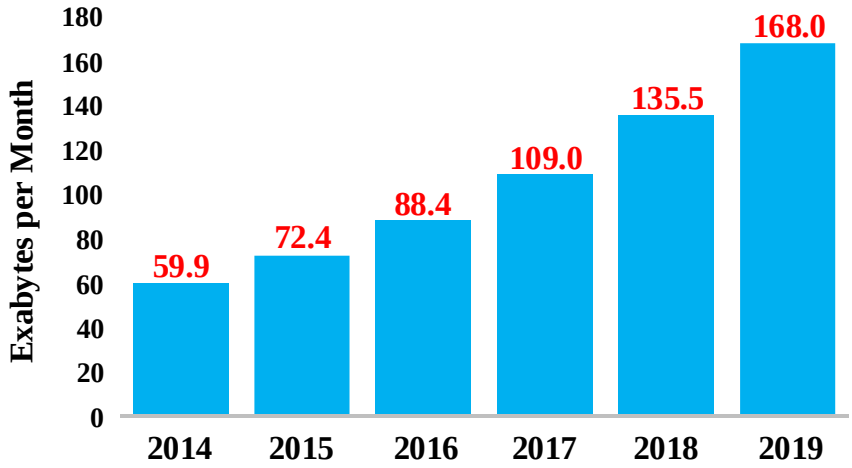

Fig. 1.1 Global IP traffic growth prediction. Figure taken from: Cisco Visual Networking Index Global Traffic Forecast, 2014-2019.

1.1 Silicon photonics: opportunities and challenges

At present, the fiber based long haul transmission of optical signals is very mature. Optical connecting between computers with fibers is also commercial. By employing the wavelength division multiplexing and spatial division multiplexing techniques, the gross transmission throughput of 255 Tbit/s has been demonstrated in a single few-mode multicore fibre [1]. This fact of high bandwidth in a single fiber is not enough, the same has to be done at the chip scale. This relates to another aspect of photonics: the integrated photonics field that deals with on-chip and chip-to-chip optical interconnections and signal processing. In this respect, silicon photonics has drawn a lot of attention in the last decade and has been regarded as the most promising platform in integrated photonics. Motivations to develop silicon photonics include [2-8]:

- The high-quality of silicon-on-insulator (SOI) wafers, which are an ideal platform for creating planar waveguide circuits. The strong optical confinement offered by the high index contrast between silicon (n = 3.45) and SiO_2 (n = 1.45) in the near-infrared region makes it possible to scale photonic devices to the hundreds of nanometers level;

- Silicon is a transparent material for the wide wavelength band from 1100 nm to 7000 nm approximately, which is far from being limited to the near-infrared communication window of around 1550 nm;

- Silicon has excellent material properties that are important in photonic devices. These include high thermal conductivity (~10× higher than GaAs), high optical damage threshold (~10× higher than GaAs), and high third-order optical nonlinearities;

- Today's mature complementary metal-oxide semiconductor (CMOS) techniques could also allow low-cost, large-scale manufacturing for silicon photonic devices.

Based on silicon photonics, lots of exciting reports and breakthroughs especially

on ultrafast nonlinear optical signal processing have been theoretically proposed or experimentally demonstrated [9, 10]. For example, R. Salem et al. reported the signal regeneration by using four-wave mixing on silicon chip [11]. Recently, B. Kuyken et al. demonstrated an octave-spanning frequency comb spanning from the telecom wavelength window ~1500 nm to the mid-infrared wavelength range at 3300 nm in a silicon nanophotonic wire waveguide [12]. As shown in Fig. 1.2, by designing the air-clad photonic wire with a rectangular cross-section of 1600 nm × 390 nm and slightly over etching by 10nm into the buried oxide, the silicon wire has nonlinear parameter of 38 $W^{-1}m^{-1}$ at 2300 nm. The zero-dispersion wavelength is at 2180 nm and the dispersion remains low over a wide spectral band. The spectra at the input from an optical parametric oscillator and output of the waveguide are shown in Fig. 1.2(c) for a pulse energy of 16 pJ. The spectrum of the pulses is significantly broadened in the silicon photonic wire waveguide through self-phase modulation.

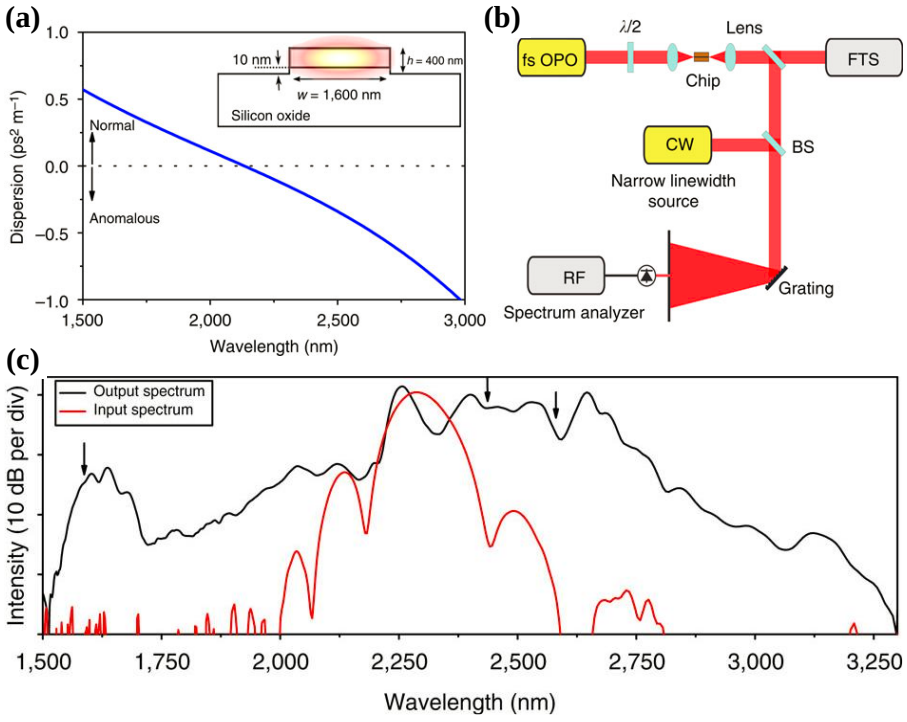

Fig. 1.2 (a) The simulated dispersion of the photonic wire waveguide. The zero-dispersion wavelength of the quasi-TE mode is at 2180 nm, while the dispersion is normal at shorter wavelengths and anomalous at longer wavelengths. The waveguide cross-section is shown

in the inset. (b) Experimental set-up: the optical parametric oscillator pumped by a Ti-Sapphire mode-locked laser is coupled to the silicon chip with a lens. The output of the chip can be sent to a photodetector or a spectrometer. (c) The spectrum at the input (red) and the output (black) of the silicon nanowire. Figure taken from ref. [12].

However, in the way to realize chip-scale integrated optical interconnects with low power consumption, advanced functionality and good convergence with electronics, two stumbling blocks emerge in silicon. Firstly, as we know, one of the key advantages of silicon photonics is that photonic and electronic functions can be integrated and fabricated onto the same chip. Nevertheless, the sizes of photonic devices are limited by the diffraction limit, which means that the dimension cannot be smaller than the half wavelength in the dielectric ($D \geq \lambda/2n$). As a result, there exists a size mismatch between photonic and electronic components in their co-integration. Secondly, the lack of second-order optical nonlinearity and the existence of free carrier effect limit the versatility and operating speed of nonlinear silicon photonics, which plays a key role in combining multiple new optical functionalities with electronics on a single chip [9].

As we know in integrated electronics, there is a clear exponential development in the number of transistors per chip, which has been doubling every two years on average during the last four decades. This phenomenon is known as the Moore's law [13]. Similarly, the development of integrated photonics is also considered to obey a photonic Moore's law. The component count on a single chip becomes larger and larger with time [7, 14]. For example, Fig. 1.3 shows the complexity development of three mainstream integrated photonic platforms measured as the number of components integrated on a single chip [7]. However, the ultimate miniaturization of optical components, which is of key importance for higher speed and lower power operations, is limited by the diffraction limit. This prevents the further improvement of integration density along with the photonic Moore's law and leads to a size mismatch between electronics and photonics.

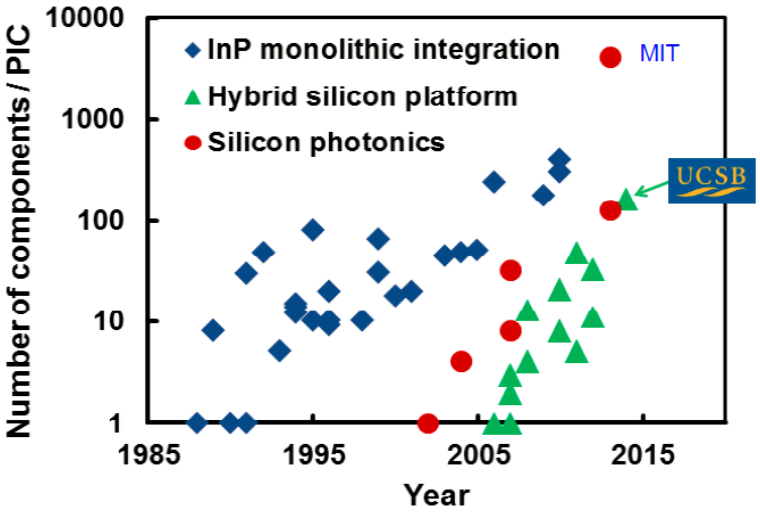

Fig. 1.3 Development of chip complexity measured as the number of components per chip for the three mainstream integrated photonic platforms of InP monolithic integration, hybrid silicon platform and silicon photonics. Figure taken from Ref. [7].

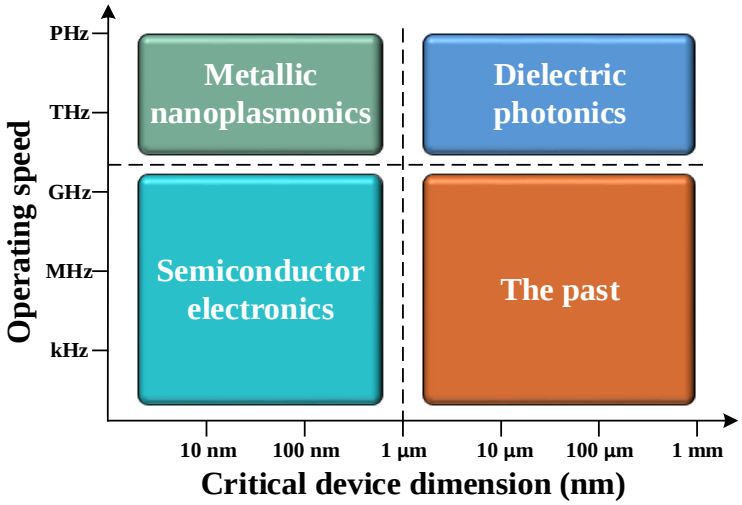

Fig. 1.4 Operating speed and critical device dimension of semiconductor electronics, dielectric photonics and metallic nanoplasmonics. The dashed lines indicate the speed limit of electronics and size limit of dielectric photonics. Figure taken from ref. [15].

In the recent years, plasmonics has been explored as a solution to overcome this obstacle due to its ability to confine the optical field into nanoscale beyond the diffraction limit [15-19]. As shown in Fig. 1.4, the dashed lines indicate physical limitations of different technologies. Semiconductor electronics is limited in speed by heat generation and interconnect delay time issues to about 10 GHz. Dielectric

photonics is limited in size by the fundamental laws of diffraction. Plasmonics offers the opportunity to combine the size of nanoelectronics and the speed of dielectric photonics, enabling devices that might naturally interface with similar-speed photonic devices and with similar-size electronic components, thus enhancing the synergy between these technologies [15]. Meanwhile, the localized strong field enhancement in plasmonic structures enhances interaction of light and matter, which is promising for enhancing the efficiency and thus further reducing the power consumption of nonlinear optical operations [20]. Due to these distinctive properties, plasmonics is perceived to have a great potential for the development of on-chip optical interconnects. In addition, plasmonics has a lot of other exciting applications beyond integrated photonics. A brief introduction to plasmonics will be given in the next section.

As mentioned before, nonlinear optical signal processing plays a key role especially on ultrafast switching, computing and modern optical communications [21-25]. Silicon offers an abundance of nonlinear optical effects that can be used to generate and process optical signals in low-cost ultra-compact chips at speeds beyond those of today's electronic devices. Many excellent papers have been published to investigate and analyze various nonlinear effects in silicon waveguides [9, 26-33]. Nevertheless, the centrosymmetry of the silicon crystal prevents second-order nonlinear effects and thus hinders the development of electro-optic silicon modulators and second-order nonlinearity based optical signal processing. Besides, in silicon it exists two photon absorption (TPA), in which an electron makes a transition from the valance band to the conduction band by the simultaneous absorption of two photons. The generated free carriers in the conduction band will subsequently change the refractive index and absorption coefficient of silicon, which are known as the free carrier dispersion (FCD) and free carrier absorption (FCA), respectively. The long lifetime of the free carriers in the conduction band leads to long-lasting FCD and FCA processes, and ultimately slows down the speed of silicon photonic devices. Meanwhile, the absorption from FCA weakens the optical intensity and in turn decreases the efficiency of nonlinear effects.

To overcome these limitations in silicon nonlinearity, a silicon organic hybrid platform which combines the advantages of silicon with the ultrafast performance of organic materials has attracted a growing attention. It is based on the integration of nonlinear organic polymers with large nonlinear susceptibilities and carrier-effect-free in the silicon photonics platform [34-37]. For example, C. Koos et al. demonstrated a silicon-organic hybrid slot waveguide to carry out all-optical high-speed signal processing of all-optical demultiplexing from 170.8 Gbs^{-1} to 42.7 Gbs^{-1} [38].

Since plasmonics and organic materials are characterized by several strengths to break the stumbling blocks in silicon for photonic integrated circuits, the next reasonable step is to combine both plasmonics and organics onto the silicon photonics to create the so-called plasmonic organic hybrid (POH) platform [39, 40]. The POH optical components are compact, high-speed, low-power-consumption and easily compatible with low-cost CMOS technique, and thus very promising for the future integrated optical signal processing. In this direction, a joint research team from Germany and Switzerland lead by C. Koos and J. Leuthold has reported some pioneer and remarkable works on POH modulators [39-44]. For example, a high-speed plasmonic phase modulator with a length of 29 μm and large radio frequency (> 65 GHz) and optical bandwidths (> 120 nm around 1550 nm) was demonstrated in [42]. As shown in Fig. 1.5(a), a continuous-wave infrared light guided by the upper-left silicon nanowire was coupled through a silicon taper to the plasmonic slot waveguide. The slot is filled with a nonlinear organic material, the refractive index n of which can be changed via the Pockels effect by applying a modulating voltage. A second taper transformed the plasmonic mode back to a photonic mode in the lower-right nanowire. Fig. 1.5(b) is the scanning electron microscope (SEM) image of the fabricated plasmonic modulator. Fig. 1.5 (c) and (d) show the mode profiles of the plasmonic mode and radio frequency (RF) signals, respectively. Both optical and modulating fields are strongly confined to the slot, resulting in a near-perfect overlap between the optical and RF signals. Consequently, the needed voltage for a phase shift of π at a

given device length L is small, leading to a small voltage–length product $U_\pi \times$L. Here, a voltage of 4.7 V can result in a peak-to-peak phase modulation of 0.31 rad for a short length of 29 μm.

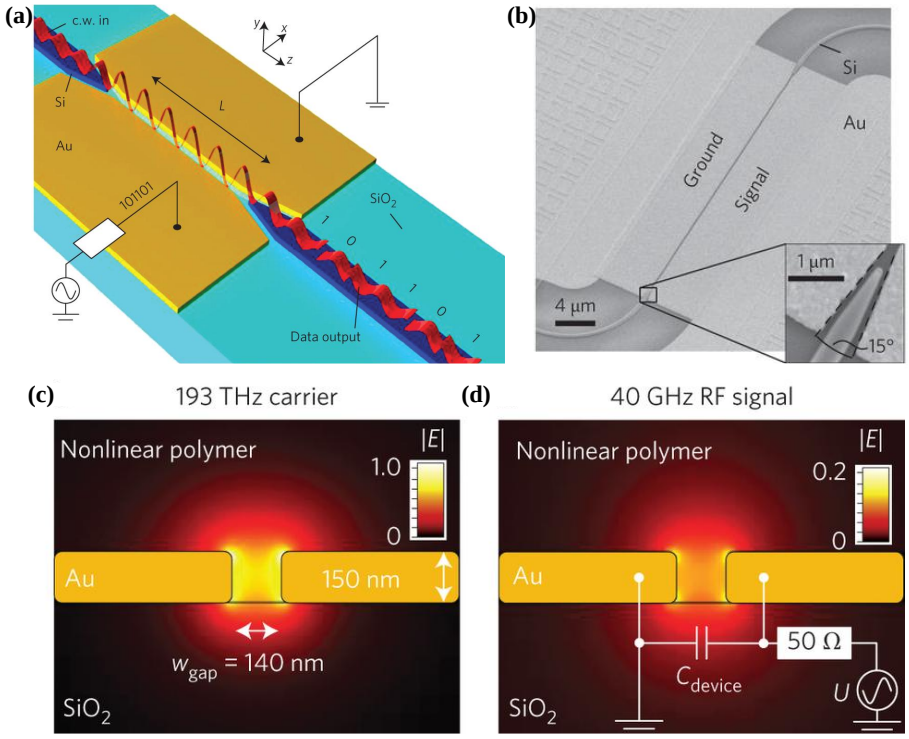

Fig. 1.5 Schematic (a) and SEM image (b) of the high-speed plasmonic phase modulator. The slot in the metal sheets is filled with an electro-optic polymer. The phase of the plasmonic mode, which propagates in the slot, is changed by applying a modulating voltage. Mode profiles of plasmonic wave (c) and RF (d) signals. The strong confinement at both frequencies facilitates the effective EO modulation with low voltage and short length. Figure taken from Ref. [42].

1.2 Plasmonics: fundamental and applications

What is plasmonics? Plasmonics is concerned with the study and application of a surprisingly rich set of optical phenomena that can be elicited from metallic nanostructures. At the origin of these phenomena is the excitation of surface plasmons (SPs), which are collective charge oscillations on a metal surface. SPs can take two forms, ranging from freely propagating electron density waves along metal surfaces to

localized charge oscillations in metal nanoparticles. In this dissertation we will concentrate on the propagation form of SPs. More specifically we will focus on the surface plasmon polaritons (SPPs), which result from the coupling of propagating SPs with light. SPPs are also defined as electromagnetic surface waves propagating at the interface between a metal and a dielectric material.

Fig. 1.6 illustrates the concept of SPPs at a metal-dielectric interface where the z>0 space is filled by a lossless dielectric material having a ε_d permittivity, and the material filling the $z < 0$ space is a metal having a ε_m permittivity. The intensity and surface charge distributions and electromagnetic field components of the SPP propagating in the *x* direction are also shown in Fig. 1.6. It propagates along the interface, and is evanescently confined in the perpendicular direction with amplitude exponentially decaying with increasing distances into each medium from the interface. The SPP mode supported by such an interface is a transverse magnetic (TM) mode, which includes the E_x, E_z and H_y field components. Detailed derivation of SPP modes supported at such a metal-dielectric interface has been reported in many previous review papers and books, for example in [45], and will not be repeated here. Instead we will present a brief summary of the SPP characteristics.

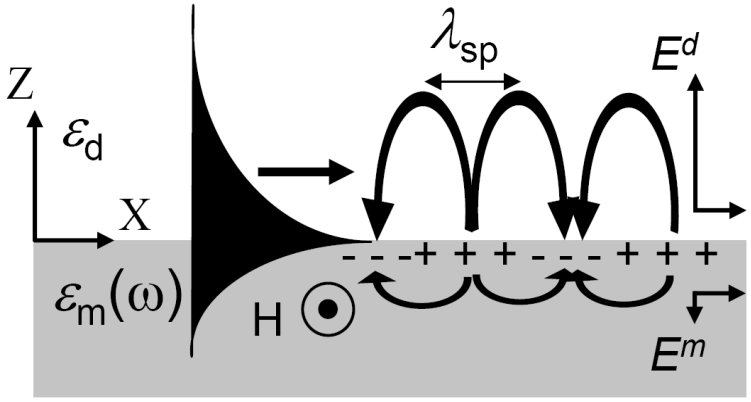

Fig. 1.6 Schematic representation of the intensity distribution and electromagnetic field components of a surface plasmon polariton supported by a metal-dielectric interface.

The dispersion relationship of the SPP mode at a metal-dielectric interface shown

in Fig. 1.6 is [45]:

$$\beta = \mathrm{k}_0 \sqrt{\frac{\varepsilon_\mathrm{d}\varepsilon_\mathrm{m}}{\varepsilon_\mathrm{d}+\varepsilon_\mathrm{m}}} \tag{1.1}$$

Here β is the propagation constant of the SPP mode propagating in the x direction. k_0 is the wave number in vacuum defined by $k_0 = 2\pi/\lambda_0$ with λ_0 being the wavelength in vacuum. In the modeling of SPP, the material dispersion of the dielectric and metal is also to be taken into consideration. Dispersion formulas of the dielectric are often considered in a Sellmeier equation given by:

$$\varepsilon_d(\lambda) = 1 + \sum_i \frac{B_i \lambda^2}{\lambda^2 - C_i} \tag{1.2}$$

Here λ is the wavelength in vacuum, and B_i and C_i are experimentally determined Sellmeier coefficients. These coefficients are usually quoted for λ in micrometres. The Sellmeier coefficients for many common optical materials can be found in handbooks and papers. For example, for the most used materials in silicon photonics, the Sellmeier coefficients of silicon and silica valid for λ = 1550 nm can be found in [46] and [47], respectively. The relative permittivity of metal is often expressed by a Drude model defined as:

$$\varepsilon_\mathrm{m}(\omega) = \varepsilon_\infty - \frac{\omega_\mathrm{p}^2}{\omega^2 - \mathrm{i}\gamma\omega} \tag{1.3}$$

where ω_p is the plasma frequency of the metal and ω is the angular frequency of light. $\gamma = 1/\tau$ where τ is the mean relaxation time of conduction electrons, and ε_∞ is a contribution due to interband transitions. For the most used metals in plasmonics, the Drude parameters of gold and silver can be taken as ε_∞ = 6.9, ω_p = 8.9 eV and γ = 0.07 eV and ε_∞ = 3.7, ω_p = 9.2 eV and γ = 0.02 eV , respectively [48] to match the experimentally measured results in [49]. Substituting Eqs. (1.2) and (1.3) into Eq. (1.1), we can get the dispersion relation of SPP. By ignoring the loss and contribution of

interband transitions, the permittivity of a lossless metal is

$$\varepsilon_{\mathrm{m}}(\omega)=1-\frac{\omega_{\mathrm{p}}^{2}}{\omega^{2}} \tag{1.4}$$

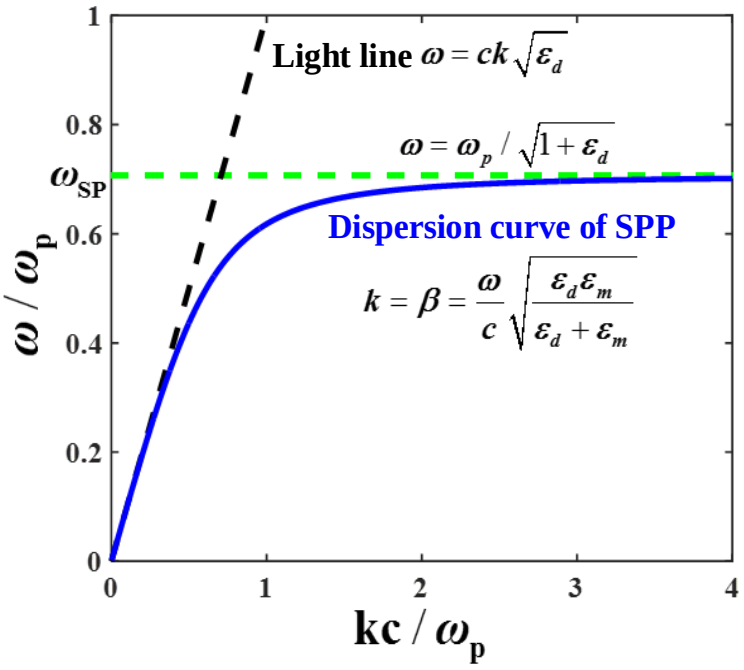

Fig. 1.7 Dispersion relation of surface plasmon polariton at a metal-dielectric interface without considering the loss of metal.

Fig. 1.7 shows the obtained dispersion relation of the SPP mode at a metal-dielectric interface without considering the loss of metal. The black dashed line is the light line in the dielectric. We can see that the propagation constant of the SPP wave is larger than the one of the light line. This leads to two consequences. Firstly, special phase-matching techniques based on grating or prism coupling are required for the excitation of SPP from a free space or fiber optical beam. Secondly and importantly, it results into better confinement of light than in dielectrics. To understand this point, let us have a look to the following equations

$$\begin{aligned} \left|k_{\mathrm{d}}\right|^{2} &= \beta^{2}-k_{0}^{2}\varepsilon_{\mathrm{d}},\ \delta_{\mathrm{d}}=1/\left|k_{\mathrm{d}}\right| \\ \left|k_{\mathrm{m}}\right|^{2} &= \beta^{2}-k_{0}^{2}\varepsilon_{\mathrm{m}},\ \delta_{\mathrm{m}}=1/\left|k_{\mathrm{m}}\right| \end{aligned} \tag{1.5}$$

Here $k_{\mathrm{d,m}}$ are the components of the wave vector perpendicular to the interface in the

two media. $\delta_{d,m}$ are the evanescent decay lengths of the fields perpendicular to the interface, which quantify the confinement of the wave. As ε_m is negative and has a large absolute value, the penetration depth of light into the metal is always small. As shown in Fig. 1.7, for small ω values, β is very close to $k_0\sqrt{\varepsilon_d}$ and the SPP dispersion curve follows the light line very closely. In this case k_d is very small and inversely δ_d is large, thus the SPP wave extends deep into the dielectric. As ω increases, the difference between β and $k_0\sqrt{\varepsilon_d}$ also increases. Correspondingly, k_d becomes larger and δ_d becomes smaller, which means better confinement of light in the dielectric side. Especially, when ω approaches the surface plasmon resonance frequency (ω_{SP}), β approaches infinity. ω_{SP} is expressed by

$$\omega_{SP} = \frac{\omega_p}{\sqrt{1+\varepsilon_d}} \tag{1.6}$$

Near the surface plasmon resonance frequency, the wave greatly slows down and the extent of the field on either side of the interface becomes vanishingly small. While another important characteristic parameter of the SPP mode: the propagation distance L_p, which is defined as the distance over which the power drops to 1/e of its initial magnitude and given by:

$$L_p = \frac{1}{2\,\mathrm{Im}[\beta]} \tag{1.7}$$

becomes shorter.

To provide here a quantitative idea of the involved orders of magnitude regarding especially the evanescent decay length and propagation distance, we plot them as a function of wavelength in Fig. 1.8 for a silver-air interface. As the wavelength decreases, the SPP mode appears to have a better confinement on the dielectric side (let us notice that δ_d is expressed in μm), while the fraction of the field concentrated in the metal slightly increases (yet, notice that δ_m is given in nm). The propagation distance thus

decreases to shorter values due to ohmic absorption in the metal. We can see here the propagation distance of SPP is on the order of millimeters, actually it will become shorter for other metals and dielectrics and roughness of interface in practical demonstrations. The losses have long been the biggest challenge of plasmonics and thus need to be managed carefully. Normally, people tend to use hybrid plasmonic structures with dielectrics, in which the loss penalty is less strong. As a matter of fact, after roughly a decade of research and development, researchers in the field have managed to figure out some potential methods to deal with this biggest challenge [50].

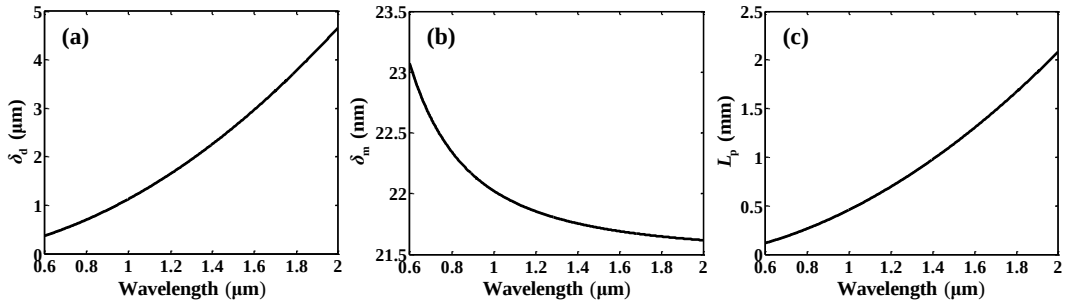

Fig. 1.8 Penetration depth into the (a) dielectric and (b) metal and (c) propagation distance of the SPP wave at the silver-air interface as a function of the wavelength.

Recently, M. L. Brongersma comprehensively summarized five strengths of plasmonics in a review paper as follows [51]: (1) extreme light concentration and light manipulation below the free space diffraction limit; (2) straightforward tunability of the optically-resonant response of metallic nanostructures by engineering their size, shape or dielectric environment; (3) simple building blocks offer a tremendous design flexibility to create a large number of optical functions; (4) efficient light-to-heat conversion with high spatial and temporal control; (5) multifunctionality of nanometallic elements in a single physical space.

These attractive strengths make plasmonics finding applications in many areas of science and technology, including plasmon-assisted catalysis, nanoscale thermal engineering for nanostructure synthesis and phase transformations, heat-assisted magnetic recording and treatment of cancer, optical trapping and sensing, optical

imaging and lithography, engineering emission from quantum emitters, thermal radiation engineering, ultrafast and nonlinear plasmonics, plasmonics for solar energy harvesting, and active chipscale plasmonic devices including most notably nanoscale sources, modulators and detectors [51].

1.3 Nonlinear silicon plasmonics

First of all, let us give a brief introduction to nonlinear optics. In nonlinear optics, the total polarization $\vec{P}(t)$ induced by electric dipoles is not linear in the electric field $\vec{E}(t)$, but satisfies the more general relation [52]:

$$\vec{P}(t) = \varepsilon_0[\chi^{(1)} \cdot \vec{E}(t) + \chi^{(2)} : \vec{E}(t)\vec{E}(t) + \chi^{(3)} \vdots \vec{E}(t)\vec{E}(t)\vec{E}(t) + \cdots] \tag{1.8}$$

where $\chi^{(1)}$ is known as the linear susceptibility. In the case of linear optics, the induced polarization depends linearly on the electric field strength. $\chi^{(2)}$ and $\chi^{(3)}$ are known as the second- and third-order nonlinear optical susceptibilities, respectively. In general, $\chi^{(i)}$ is a tensor of rank i + 1. In the forms shown, we have also assumed an instantaneous response of the polarization to the electric field strength. The second-order optical nonlinearity vanishes in centrosymmetric crystals, while the third-order nonlinear optical interactions can occur for both centrosymmetric and noncentrosymmetric media. Common second-order nonlinear effects include second harmonic generation, sum frequency generation, difference frequency generation, Pockels effect (also known as electro-optic effect) and optical rectification effect. Frequently-used third-order nonlinear effects include third harmonic generation, four-wave mixing, self-phase modulation, and cross-phase modulation. These diverse nonlinear effects provide much more degrees of freedom to control the optical field, which make nonlinear optics playing a great impact in today's daily life, such as in the fields of lasers, material interactions and information technology [53].

Especially, nonlinear optics has been the hotspot of research in integrated

photonics and considerably studied for electro-optic modulation, all-optical signal processing, generation of ultra-short pulses, and ultrafast switching [20, 54]. Realizing efficient optical nonlinear effects at nanoscales and within short distances plays a key role in improving the density and reducing the power consumption. Plasmonics opens up an opportunity to simultaneously increase device nonlinear efficiencies, reduce device power consumptions and footprints, speed up the device response time and improve the device flexibility. In principle, the role of plasmonics in nonlinear optics is threefold. Firstly, the strong optical field and related enhanced nonlinearity in plasmonic nanostructures allows nonlinear effects to be utilized with reduced optical power. Secondly, they scale down the sizes of nonlinear components, which is important for the development of integrated photonic devices and, ultimately, of the fully functional nanophotonic circuitry. Thirdly, the response time of plasmonic excitations is ultrafast, allowing optical signals to be manipulated on femtosecond timescales. The detailed principle and applications for the field of nonlinear plasmonics can be found in a good review paper of Ref. [20]. Here we just want to highlight the mentioned research status and elicit the next development expectations of the field.

With the continuous development of modern nanofabrication technique, precisely experimental implementations of nonlinear plasmonic devices are possible and demonstrated in plenty of reports. However, with few exceptions the majority of experiments on nonlinear plasmonics have involved free-space beams at least for signal or control light. For certain applications, it is necessary to design systems where all beams are maintained within the integrated plasmonic circuitry [20]. In the same time, the compatibility with silicon photonics is also strongly expected. To our best knowledge, few work especially experimental demonstrations have been reported to address these two expectations together. The aforementioned POH modulators belong to one of them. As another example, S. Sederberg et al. recently demonstrated for the first time an efficient third harmonic generation in a silicon-based nanoplasmonic waveguide. As show in Fig. 1.9, the proposed waveguide consisting of a silicon core

and a gold cap is simple to fabricate, compatible with modern electronics and photonics technologies, and occupies an ultracompact footprint of 0.40 μm^2. Femtosecond laser pulses at λ = 1550 nm with input powers in the range of 85 μW – 1.52 mW are used to generate strong THG. The conversion efficiencies is up to 2.3 × 10^{-5} with waveguide length of 5 μm, which is the highest reported to date in any silicon-based device or nanoplasmonic structure [55].

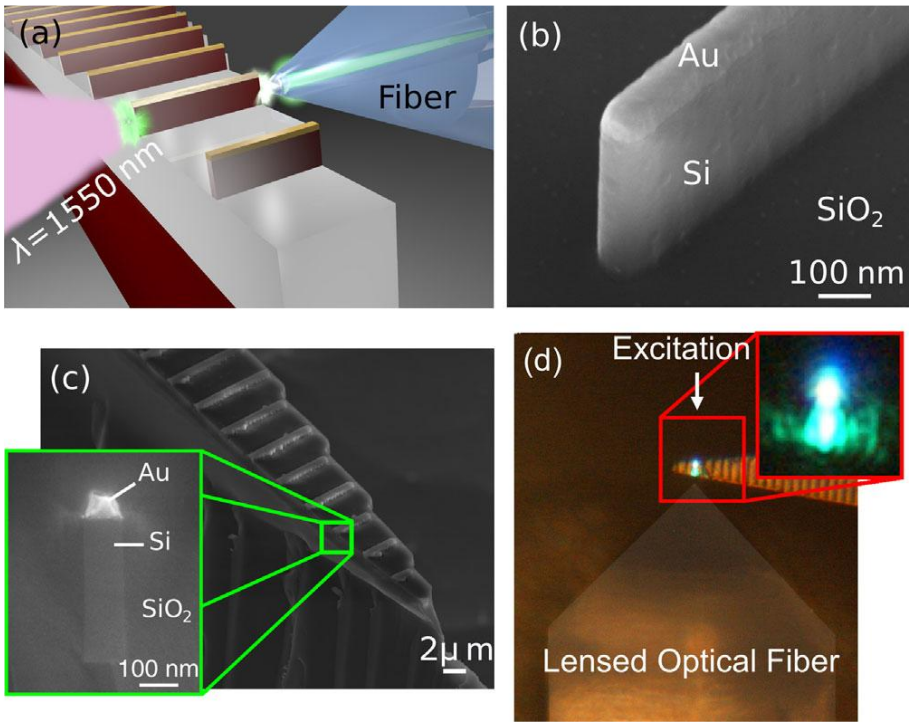

Fig. 1.9 Efficient third harmonic generation in a silicon-based nanoplasmonic waveguide. Figure taken from Ref. [55].

We define the system in which all beams are maintained in the integrated plasmonic circuitry and compatible with silicon photonics as the silicon plasmonic platform. Nonlinear silicon plasmonics is still a young research field, but its basic concepts and great potential have been proposed in a wide variety of ways already. At present, precise experimental fabrication and measurement of the nanoscale silicon plasmonic waveguides is still a big challenge and concepts for more sophisticated waveguide designs and more complex nonlinear effects need to be investigated. Nevertheless, we envisage the field to become increasingly important in the

development of the future integrated nanophotonics, just as traditional nonlinear silicon photonics was in shaping the landscape of modern integrated photonics.

Taking both expectations in mind, in this dissertation we have designed and investigated different kinds of nonlinear silicon plasmonic waveguides and exploited the effective nonlinear effects induced in the nanoscale plasmonic waveguide for optical signal processing.

1.4 Organization

The organization of the dissertation is as follows.

In **chapter 2**, we firstly give a brief review on the plasmonic waveguides. Especially, we primarily focus on two kinds of waveguides: plasmonic slot waveguides (PSW) and hybrid plasmonic waveguides (HPW). Then, we derive the theoretical model of nonlinear coupled-wave equations which have been used to analyze the nonlinear effects in silicon plasmonic waveguides with losses and for the investigation of the mechanisms proper to enhance optical nonlinear effects.

In **chapter 3**, we investigate the possibility of enhancing nonlinear effects based on the PSW and the related applications in optical signal processing. Specifically, three kinds of nonlinear effects are studied, including the enhanced second harmonic generation (SHG), a new high-speed electrooptic modulation mechanism based on the electrically controlled SHG and high-speed optical detection based on the optical rectification effect.

In **chapter 4**, we focus on the HPW-based nonlinear enhancement. Efficient SHG and optical parameter amplification (OPA) are analyzed. The SHG is then further enhanced by using HPW-based ring resonators. The OPA can be applied to regenerate the phase shift keying optical signals.

In **chapter 5**, we present the experimental realization of PSW. The goal is to

demonstrate the optical rectification effect proposed in chapter 3. The chapter includes the design, fabrication and measurement of the structures. By spin-coating an EO polymer onto PSW, the nonlinear property of the coated PSW is investigated.

In **chapter 6**, we conclude our work and have a look to the future possible steps.

Chapter 2

Theoretical analysis of nonlinear processes in silicon plasmonic waveguides

We aim in this dissertation at investigating the potentials of the combination of silicon photonics and plasmonics for the design of photonic integrated circuits and functions. We will focus on a particular aspect of this research field, called silicon plasmonics: the enhancement of nonlinear effects by using plasmonic structures.

In this chapter, we firstly give a brief review of the main plasmonic waveguides proposed in previous works and then focus on two kinds of plasmonic waveguides that can easily be integrated within the silicon photonics platform. In the second part, we derive a set of nonlinear coupled-wave equations (NCEs) which can be exploited to analyze the nonlinear effects induced in the lossy plasmonic waveguides. Note that the NCEs have been widely addressed before in fibers [56] and silicon waveguides [29, 57], in which the losses are negligible. While, in plasmonic waveguides the loss cannot be neglected and thus in the derivation of NCE the normalization condition needs to be considered in term of the unconjugated reciprocity theorem [58, 59]. In Ref. [59], the researchers have done similar derivations to model the optics-to-THz conversion in metallic slot waveguides. Here in this manuscript, we obtain a general form of NCE both in the frequency and time domains that can be used to model any kind of nonlinear optical effects induced in a lossy waveguide. Lastly, four general guidelines for the design of integrated waveguides providing strong nonlinear effects are put forward based on the proposed NCEs.

2.1 Silicon plasmonic waveguides

Due to the excellent ability to confine light without suffering from the diffraction limit,

plasmonic waveguides have attracted a growing interest in the last decade. Many kinds of nanoscale plasmonic waveguides have been proposed theoretically and demonstrated experimentally, such as metal nanowire waveguides [60-62], metal nanoparticle chain array waveguides [63-66], channel plasmon waveguides being constructed by V-grooves in metals [67], plasmonic slot waveguides (or so called metal-dielectric-metal waveguides in two-dimensional case) consisting of a slot sandwitched between two metallic regions [68-72], long range plasmonic waveguides (or so called dielectric-metal-dielectric waveguides in two-dimensional case) comprising a finite-width metal stripe surrounded by dielectric media [73-75], hybrid plasmonic waveguides being made up of a high refractive index (RI) dielectric material separated from the metal part by a subwavelength low RI dielectric gap [76-79], and dielectric loaded plasmonic waveguides made of a dielectric ridge placed on a metal surface [80-82].

All these plasmonic waveguides are able to support tight confinement of optical fields in two directions to the nanoscale that dielectric waveguides unable to do. However, the losses come along with the tight confinement. In plasmonic waveguides, generally there exists a trade-off between confinement and loss. Better confinement is always accompanied by larger losses. This point can be fundamentally understood from Fig. 1.8 for the SPP mode at a metal-dielectric interface: for smaller wavelengths it supports better confinement in the dielectric (Fig. 1.8(a)), while the fraction of the field concentrated in the metal increases (Fig. 1.8(b)). The propagation distance thus decreases to shorter values due to larger ohmic absorption in the metal (Fig. 1.8(c)).

In the early stages, the priority was to realize the best confinement of the optical field, while the loss issue was not considered so much. In the initially proposed plasmonic waveguide structures, such as metal nanowire waveguides, nanoparticle array waveguides and channel plasmon waveguides shown in Fig. 2.1, even though ultra-highly localization of the optical field into nanometer scales was achieved, the related structures had large losses, meaning that only short propagation distances (usually ~μm) were possible. Besides, the fabrication and precise control of these

waveguide were complex due to their nonrectangular shapes. Additionally, as the related devices were hardly compatible with the silicon photonics platform, we have not considered them in the present manuscript for the design of plasmonic-enhanced nonlinear optical functions on silicon.

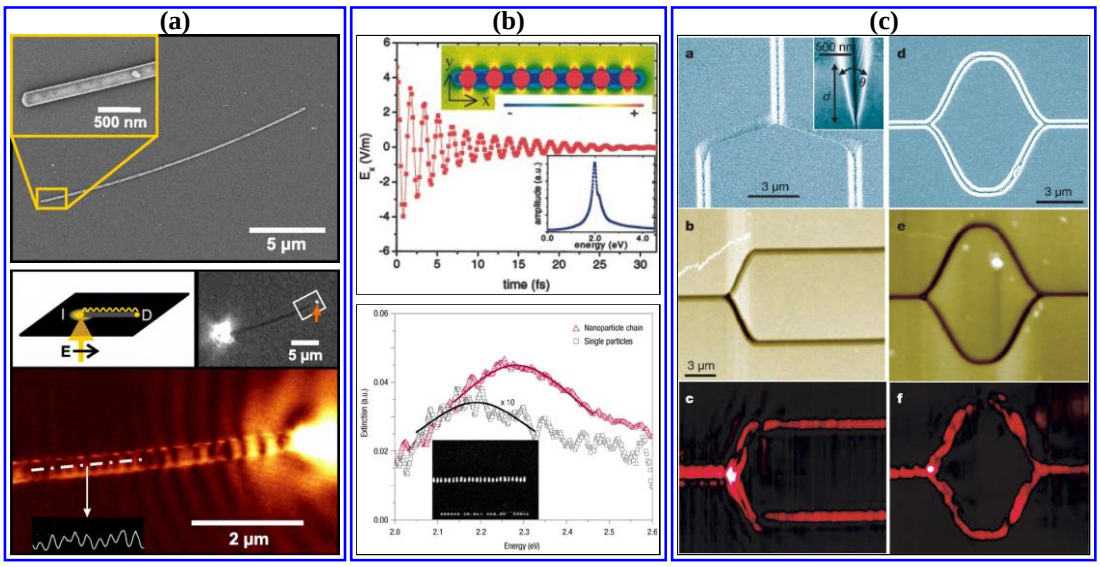

Fig. 2.1 Initially proposed plasmonic waveguides: (a) metal nanowire waveguides [61], (b) metal nanoparticle chain waveguides [65, 66] and (c) channel plasmon waveguides [67]. They can confine the optical field into nanometer scales, while the losses are usually large.

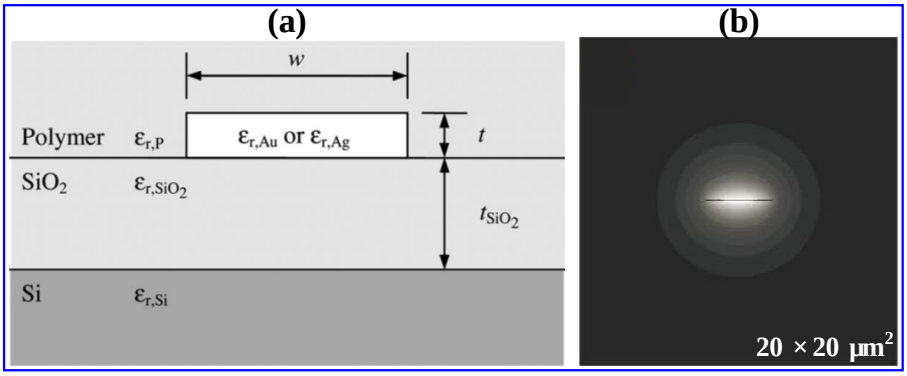

Fig. 2.2 (a) Long range plasmonic waveguide made of a gold stripe with width of 4 μm and thickness of 25 nm. (b) mode intensity contours plotted over a 20 × 20 μm^2 cross-sectional domain. Figure taken from [74].

In an opposite direction, the long range plasmonic waveguides enable long propagation distances, but their confinement properties show in fact no advantage if

compared with conventional dielectric waveguides. Fig. 2.2 shows the schematic and mode profile of a typical long range plasmonic waveguide. By considering an gold stripe with width of 4 μm and thickness of 25 nm, the experimental measured loss is 1.07 dB/mm at λ = 1550 nm, while the mode extends several micrometers away from the metal stripe [74]. Thus, this kind of waveguides has been disregarded in the investigations performed in this manuscript.

Beyond these two extreme cases, the loss/field-confinement compromise of plasmonic waveguides can fortunately be adjusted by a proper choice of the waveguide material and geometry cross-section. Plasmonic slot waveguides, hybrid plasmonic waveguides and dielectric loaded plasmonic waveguides, as shown in Fig. 2.3, have been proposed in this purpose. These waveguides can also be experimentally realized with the standard CMOS technology, belong to the previously mentioned silicon plasmonic waveguides.

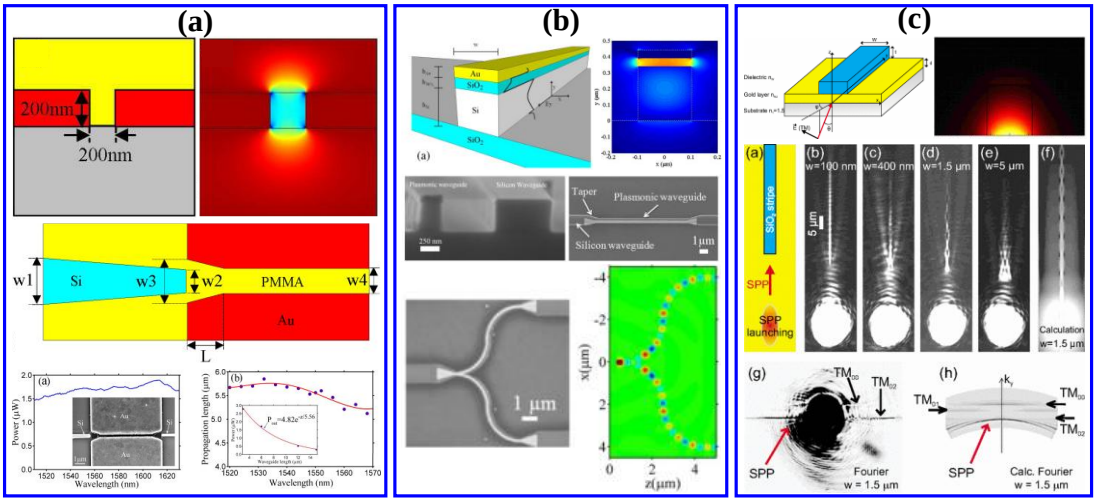

Fig. 2.3 Silicon plasmonic waveguides have better compromise between confinement and loss. (a) plasmonic slot waveguides [72], (b) hybrid plasmonic waveguides [79], and (c) dielectric loaded plasmonic waveguides [81].

The works reported in this manuscript have been mostly based on plasmonic slot waveguides and hybrid plasmonic waveguides. So in the next, we will give a more detailed introduction to these two waveguide families. We will see that due to the

difference of the mode confinement mechanism and loss level, they are suitable for different nonlinear applications.

2.1.1 Plasmonic slot waveguides

In view of the strong localization of optical field on a single metal/dielectric interface on the dielectric side due to the large discontinuity difference of the material permittivities, it is intuitive to closely combine two interfaces to form the so-called metal-dielectric-metal waveguide. In a realistic planar scheme, one gets the so-called plasmonic slot waveguide (PSW).

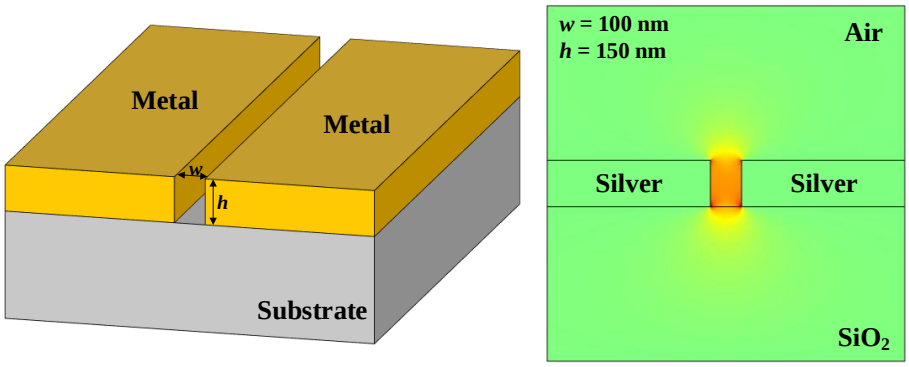

Fig. 2.4 Typical configuration and calculated field distribution for the major component E_x of the fundamental mode of a plasmonic slot waveguide with w = 100 nm and h = 150 nm. One sees that the field is highly localized and greatly enhanced in the nanoscale slot.

Fig. 2.4 shows the typical configuration and mode profile of a PSW. The SPPs on two surfaces that exist in the PSW couple to each other and result in a strong localization of the field in the slot area. The slot width can be chosen down to a few tens of nanometers. Actually, this waveguide geometry is very similar to the silicon slot waveguides, as proposed by Almeida and co-workers [83]. Merely the amplitude of the real part of the metal permittivity is even larger than the one of silicon, which makes PSW have an even larger enhancement of optical fields in the slot region than their dielectric counterparts. To have a more quantitative vision, we plot in Fig. 2.5 the mode effective index n_{eff}, propagation length L_p and mode effective area A_{eff} of the fundamental mode in PSW as a function of slot width w for different slot height h. A_{eff},

whose definition can be found in Section 2.2.2 by Eq. (2.19), is a very key parameter in nonlinear enhancement. Note here that these parameters and all other waveguide mode calculations performed by us have been calculated by a finite element method based commercial software (COMSOL Multiphysics) [84].

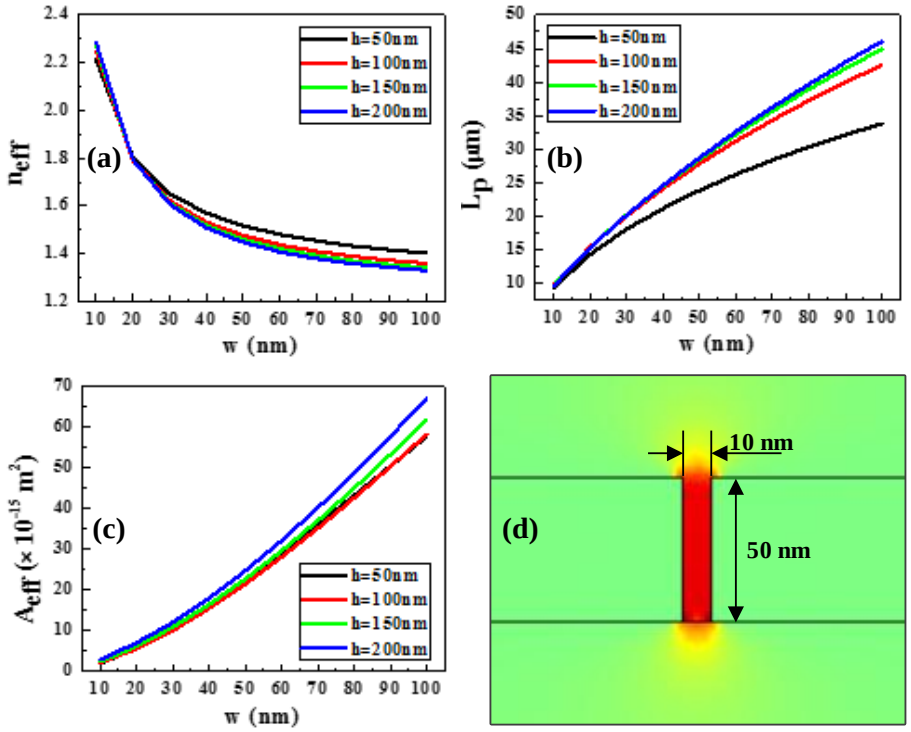

Fig. 2.5 (a) Mode effective index n_{eff}, (b) propagation length L_p and (c) mode effective area A_{eff} of the fundamental mode in PSW as a function of slot width for different slot height. (d) The electric field distribution when w = 10 nm and h = 50 nm. The optical wavelength is fixed at λ = 1550 nm.

The metal, substrate and cladding materials are chosen to be silver, SiO_2 and air, respectively. As the slot width decreases, the impact of the height on the mode property becomes weaker. Meanwhile, n_{eff} increases, while the loss becomes larger. Especially, as shown in Fig. 2.5(d), PSW is capable of guiding a highly confined mode at λ = 1550 nm into a slot as small as 10 nm × 50 nm. The corresponding mode effective area is as small as 2.04 × 10^{-15} m^2, which is down to $\lambda^2/1200$. However, L_p decreases to 9.35 μm. Therefore, there usually exists an optimized dimension in PSW-based optoelectronic devices for realizing best device performances. This will be seen in Chapter 3.

The supporting of tight mode confinement, reasonable propagating lengths and intrinsic broadband nature make PSW a promising candidate for chip-scale nanocircuitry. If compared with metal nanowire waveguides, metal nanoparticle array waveguides and channel plasmon waveguides, planar PSWs are easier to fabricate. This waveguide geometry also leads itself appropriate to compact optoelectronic devices as it is convenient to use the same metallic regions to define the optical guide and as electrical contacts to generate a DC/RF electric field across the slot gap filled with a switching medium. For instance, as mentioned in Chapter 1 by Fig. 1.5, a high-speed phase modulator based on this mechanism was recently demonstrated by filling the slot with an electro-optic polymer [42]. All these features make PSWs very attractive for the realization of ultra-dense integrated optoelectronic components. For example, PSW-based all-optical logic gates [85], subdiffraction directional couplers [86], biosensors [87], high-speed modulators [39-44], filters based on plasmon-induced transparency [88], fundamental elements such as mirrors, bends and splitters [89] , and nonlinear optical devices [90-93], etc, have been proposed.

When filling the slot gap by nonlinear media, effective nonlinear effects can thus be envisaged at low optical power. For example, spin-coating second order nonlinear polymers in to the slot could give rise to the enhanced second harmonic generation and optical rectification in PSWs [94-96]. These works will be detailed in Chapter 3.

2.1.2 Hybrid plasmonic waveguide

As mentioned earlier, the main drawback of plasmonic waveguides is the loss issue, particularly for PSW, which losses scale in 0.1-0.5 dB/μm, as shown in Fig. 2.5. This makes them hardly suitable for some linear and nonlinear applications where the loss is a pivotal factor, such as long distance propagation and nonlinear parametric amplification. In Ref. [90], Rukhlenko et al. investigated nonlinear metal-silicon-metal (MSM) waveguides and came to the conclusion that even though all nonlinear effects are substantially stronger in MSM plasmonic waveguides than in silicon waveguides of

the same thickness, the loss-induced reduced length of MSM waveguides makes the Kerr effect, two-photon absorption, and stimulated Raman scattering too inefficient for device applications. On the contrary, free-carrier effects remain strong enough even in a 10-nm-thick MSM waveguide that is only 500-nm long, and they can dramatically affect the propagation of SPPs. Therefore, it is free-carrier absorption and free-carrier dispersion that should be used to control light in nanosized MSM waveguides [90].

To overcome this disadvantage of PSW, people came up more recently with the concept of hybrid plasmonic waveguide (HPW). It has been shown that HPWs have the potential to achieve a nano-scale light confinement as well as relatively long propagation distance simultaneously. In 2007, Alam et al. initially proposed the form of a HPW including a silicon nanowire adjacent to a metal surface [76]. Later in Ref. [77], the concept of hybrid plasmonic waveguide was proposed formally and a HPW was obtained by putting a dielectric cylinder above a metal surface, for which the mode area was as small as $\lambda^2/400$.

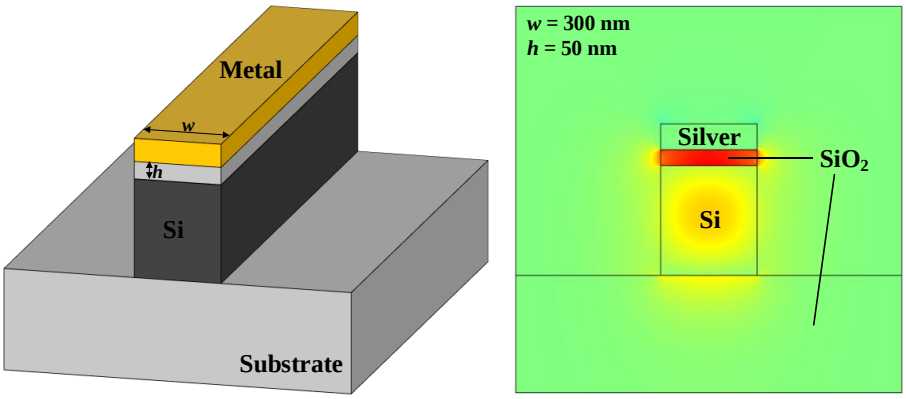

Fig. 2.6 Typical configuration and calculated field distribution for the major component E_y of the fundamental mode of a hybrid plasmonic waveguide with w = 300 nm and h = 50 nm. The field is highly localized and greatly enhanced in the nanoscale low RI spacer.

Fig. 2.6 shows the typical configuration and mode profile of a HPW. It consists of a high refractive index (RI) region, a metal cap and a low RI spacer between them. This kind of waveguide is also compatible with the silicon on insulator technology. The

working principle of the HPW can be considered as the coupling between the SPPs mode supported by the metal surface and the dielectric mode guided by the high RI dielectric stripe. This results in a guided mode which has most of its power concentrated between the dielectric-stripe and the metal surface, i.e. in the low RI spacer. This feature is clearly characterized in Fig. 2.6, where the optical field is mainly confined and significantly enhanced in the nanoscale low RI spacer layer.

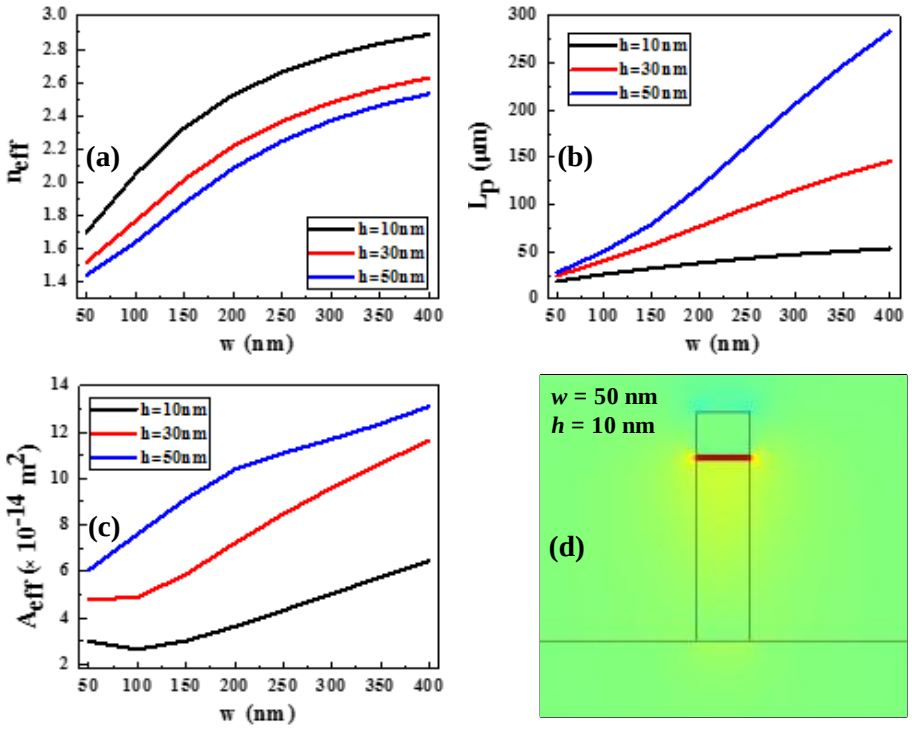

Fig. 2.7 (a) Mode effective index n_{eff}, (b) propagation length L_p and (c) mode effective area A_{eff} of the fundamental mode at λ = 1550 nm in HPW as a function of spacer width for different spacer height. (d) The electric field distribution when w = 50 nm and h = 10 nm.

Fig. 2.7 shows the mode effective index n_{eff}, propagation length L_p and mode effective area A_{eff} of the fundamental mode in HPW as a function of spacer width w for different spacer height h. The thickness of the silicon stripe and the optical wavelength are fixed at 340 nm and λ = 1550 nm, respectively. Similar to the mode property of PSW, smaller spacer layer leads to larger n_{eff}, shorter L_p, and smaller A_{eff}. **Thus, we can adjust the compromise between confinement and losses by tuning the dimensional sizes of HPW.** In another picture, HPW can also be considered as a kind of slot

waveguide [83], merely it is a vertical slot between a metallic region and a high RI dielectric material (which, in most cases, is silicon). As a result, HPWs compromise the mode properties of both PSWs and silicon slot waveguides. **It shows better confinement properties than silicon slot waveguides and lower optical losses if compared with PSWs.** The propagation length is on the order of hundreds of micrometers, while in PSW is a few tens of micrometers. To have a visual comparison with PSW, let us take a look to the related parameters with same size of spacer layer (i.e. 10 nm $\times$50 nm) for two kinds of waveguides. They are L_p = 18.67 μm, A_{eff} = 2.98 $\times 10^{-14}$ m^2 for HPW, and L_p = 9.35 μm, A_{eff} = 2.04 $\times 10^{-15}$ m^2 for PSW, respectively. Clearly, HPW have lower losses and larger mode size over one order of magnitude, this is because some part of the field is confined into the silicon part, as shown in Fig. 2.7(d).

Another interesting property of HPWs that disappears in PSWs is that the optical fields of the TM and TE modes in such a HPW are concentrated in different areas. The TM mode is concentrated in the low RI layer, whereas the conventional TE mode is concentrated in the high RI region. This makes HPW very interesting in realizing polarization components. Because of these attractive features HPWs have attracted a growing interest in recent years. Many different applications have been suggested such as subwavelength plasmon lasers [97], modulators [98, 99], directional couplers [100-102], ring resonators [103-105], polarization devices [106-108], and nonlinear applications [109-112] etc.

When substituting the low RI dielectric with nonlinear materials, nonlinear effects can be effectively enhanced. In this manuscript, we analyze the enhanced second harmonic generation and phase sensitive amplification based on this kind of waveguides without and with the help of micro-ring resonators [113-115], as shown hereafter in Chapter 4.

2.2 Nonlinear coupled-wave equations

In order to model the nonlinear processes in plasmonic waveguides, such as estimating the efficiency of a nonlinear wavelength conversion process or finding out the phase change of a phase modulation process, the nonlinear coupled mode theory is used in this dissertation. In the following, we will give a detailed derivation for the nonlinear coupled-wave equation (NCE) and then give the key factors to enhance the nonlinear effects in integrated waveguides based on the NCE.

2.2.1 Derivation

For a specific frequency ω in a nonlinear planar waveguide, we consider the nonlinear polarization $\vec{P}^{NL}$ as a source and the corresponding excited electromagnetic field $\{\vec{E}, \vec{H}\}$ which propagates along the +z direction fulfills the Maxwell's equations in the frequency domain:

$$\begin{aligned} \nabla \times \vec{E} &= i\omega\mu\vec{H} \\ \nabla \times \vec{H} &= -i\omega\varepsilon\vec{E} - i\omega\vec{P}^{NL} \end{aligned} \tag{2.1}$$

and can be expanded in terms of all modes at the same frequency:

$$\begin{aligned} \vec{E} &= \sum_{v} \tilde{A}_v(z)\vec{E}_v = \sum_{v} \tilde{A}_v(z)\vec{E}_v(x,y)\exp(ik_v z) \\ \vec{H} &= \sum_{v} \tilde{A}_v(z)\vec{H}_v = \sum_{v} \tilde{A}_v(z)\vec{H}_v(x,y)\exp(ik_v z) \end{aligned} \tag{2.2}$$

where k_v is the propagation constant of v-th mode. $\tilde{A}_v(z)$ is the slowly varied complex mode amplitude. $\{\vec{E}_v(x,y) = \vec{E}_{v,t}(x,y) + \vec{E}_{v,z}(x,y),\ \vec{H}_v(x,y) = \vec{H}_{v,t}(x,y) + \vec{H}_{v,z}(x,y)\}$ are the mode profiles of the v-th guided mode with the subscripts t and z representing the transverse and longitudinal components, respectively. In principle, the expansion of Eq. (2.2) should consider all guided and radiation modes and is continuous over the radiation modes [116]. From a theoretical point of view, the rigorous completeness of the used set of modes is still a question under debate. Involvement of mathematical

mode solutions diverging at infinity (thus non normalizable) is in principle necessary [117]. However, in many practical cases, a limited set of interacting waveguide modes is to be considered. In the present manuscript, only the main guided modes have been considered at the different involved frequencies and power exchanges through nonlinear optical mechanisms has been considered between them. This approximation is very common in the study of nonlinear optical waveguides [59]. The related guided mode profiles have been normalized as:

$$\frac{1}{2}\iint \vec{e}_z \cdot \{\vec{E}_i(x,y)\times\vec{H}_j(x,y)\}dxdy = \delta_{ij} \tag{2.3}$$

Note that this normalization condition is considered here in term of the unconjugated reciprocity theorem, which is applicable to lossy media [58]. As a result, the derived NCE is valid for plasmonic waveguides, which are intrinsically lossy due to the absorption loss from the metal.

For a specific guided mode of $\{\vec{E}_u, \vec{H}_u\}$, the Maxwell's equations without the nonlinear part are satisfied:

$$\begin{aligned} \nabla\times\vec{E}_u &= -\mu\frac{\partial\vec{H}_u}{\partial t} = i\omega\mu\vec{H}_u \\ \nabla\times\vec{H}_u &= \varepsilon\frac{\partial\vec{E}_u}{\partial t} = -i\omega\varepsilon\vec{E}_u \end{aligned} \tag{2.4}$$

By reversing the sign of *z* in Maxwell's equations, we can construct a new solution to Eq. (2.4) with the form [59, 116]:

$$\begin{aligned} \vec{E}_u{}' &= \left[\vec{E}_{u,t}(x,y) - \vec{E}_{u,z}(x,y)\right]\exp(-ik_u z) = \vec{E}_u{}'(x,y)\exp(-ik_u z) \\ \vec{H}_u{}' &= \left[-\vec{H}_{u,t}(x,y) + \vec{H}_{u,z}(x,y)\right]\exp(-ik_u z) = \vec{H}_u{}'(x,y)\exp(-ik_u z) \end{aligned} \tag{2.5}$$

Then, by using the vector identity $\nabla\cdot(\vec{a}\times\vec{b}) = \vec{b}\cdot(\nabla\times\vec{a}) - \vec{a}\cdot(\nabla\times\vec{b})$ and based on Eq. (2.1) and Eq. (2.4), we obtain:

$$\nabla\cdot(\vec{E}\times\vec{H}_u{}')=\vec{H}_u{}'\cdot(\nabla\times\vec{E})-\vec{E}\cdot(\nabla\times\vec{H}_u{}')=i\omega\mu\vec{H}\cdot\vec{H}_u{}'+i\omega\varepsilon\vec{E}\cdot\vec{E}_u{}'$$
$$\nabla\cdot(\vec{E}_u{}'\times\vec{H})=\vec{H}\cdot(\nabla\times\vec{E}_u{}')-\vec{E}_u{}'\cdot(\nabla\times\vec{H})=i\omega\mu\vec{H}\cdot\vec{H}_u{}'+i\omega\varepsilon\vec{E}\cdot\vec{E}_u{}'+i\omega\vec{P}^{NL}\cdot\vec{E}_u{}' \tag{2.6}$$

Thus

$$\nabla\cdot(\vec{E}\times\vec{H}_u{}'-\vec{E}_u{}'\times\vec{H})=-i\omega\vec{P}^{NL}\cdot\vec{E}_u{}' \tag{2.7}$$

The next step is substituting Eq. (2.2) into Eq. (2.7) and integrating both sides of Eq. (2.7) over the cross-section of the waveguide. Applying the orthogonal normalization condition of Eq. (2.3) yields the integral of left side to be:

$$\begin{aligned}
&\iint\nabla\cdot(\vec{E}\times\vec{H}_u{}'-\vec{E}_u{}'\times\vec{H})dxdy=\iint\left\{-i\omega\vec{P}^{NL}\cdot\vec{E}_u{}'\right\}dxdy\\
&=\iint\left\{\frac{\partial\left[\vec{e}_x\cdot(\vec{E}\times\vec{H}_u{}'-\vec{E}_u{}'\times\vec{H})\right]}{\partial x}+\frac{\partial\left[\vec{e}_y\cdot(\vec{E}\times\vec{H}_u{}'-\vec{E}_u{}'\times\vec{H})\right]}{\partial y}+\frac{\partial\left[\vec{e}_z\cdot(\vec{E}\times\vec{H}_u{}'-\vec{E}_u{}'\times\vec{H})\right]}{\partial z}\right\}dxdy\\
&=\frac{\partial}{\partial z}\iint\vec{e}_z\cdot(\vec{E}\times\vec{H}_u{}'-\vec{E}_u{}'\times\vec{H})dxdy\\
&=\frac{\partial}{\partial z}\iint\vec{e}_z\cdot\left[\sum_v\tilde{A}_v(z)\vec{E}_v(x,y)\exp(ik_vz)\times\vec{H}_u{}'\right]dxdy-\\
&\quad\frac{\partial}{\partial z}\iint\vec{e}_z\cdot\left[\vec{E}_u{}'\times\sum_v\tilde{A}_v(z)\vec{H}_v(x,y)\exp(ik_vz)\right]dxdy\\
&=\frac{\partial}{\partial z}\iint\vec{e}_z\cdot\left[\sum_v\tilde{A}_v(z)\exp(ik_vz-ik_uz)\vec{E}_v(x,y)\times\vec{H}_u{}'(\mathrm{x},\mathrm{y})\right]dxdy-\\
&\quad\frac{\partial}{\partial z}\iint\vec{e}_z\cdot\left[\sum_v\tilde{A}_v(z)\exp(ik_vz-ik_uz)\vec{E}_u{}'(x,y)\times\vec{H}_v(x,y)\right]dxdy\\
&=-\frac{\partial}{\partial z}\iint\vec{e}_z\cdot\left[\sum_v\tilde{A}_v(z)\exp(ik_vz-ik_uz)\vec{E}_v(x,y)\times\vec{H}_u(\mathrm{x},\mathrm{y})\right]dxdy-\\
&\quad\frac{\partial}{\partial z}\iint\vec{e}_z\cdot\left[\sum_v\tilde{A}_v(z)\exp(ik_vz-ik_uz)\vec{E}_u(x,y)\times\vec{H}_v(x,y)\right]dxdy\\
&=-\frac{\partial}{\partial z}\tilde{A}_u(z)\iint\vec{e}_z\cdot\left[\vec{E}_u(x,y)\times\vec{H}_u(\mathrm{x},\mathrm{y})\right]dxdy-\frac{\partial}{\partial z}\tilde{A}_u(z)\iint\vec{e}_z\cdot\left[\vec{E}_u(x,y)\times\vec{H}_u(x,y)\right]dxdy\\
&=-4\frac{\partial\tilde{A}_u(z)}{\partial z}
\end{aligned} \tag{2.8}$$

In the derivation of Eq. (2.8), we have used the following relations:

$$\iint \vec{e}_z \cdot \left[\vec{E}_v(x,y) \times \vec{H}_u{}'(\mathrm{x},\mathrm{y}) \right] dxdy = -\iint \vec{e}_z \cdot \left[\vec{E}_v(x,y) \times \vec{H}_u(\mathrm{x},\mathrm{y}) \right] dxdy = -2\delta_{uv}$$
$$\iint \vec{e}_z \cdot \left[\vec{E}_u{}'(x,y) \times \vec{H}_v(\mathrm{x},\mathrm{y}) \right] dxdy = \iint \vec{e}_z \cdot \left[\vec{E}_u(x,y) \times \vec{H}_v(\mathrm{x},\mathrm{y}) \right] dxdy = 2\delta_{uv} \quad (2.9)$$

Thus, we can finally obtain the NCE for guided waves to be:

$$\frac{\partial \tilde{A}_u}{\partial z} = \frac{i\omega}{4} \iint \left\{ \vec{P}^{NL} \cdot \vec{E}_u{}' \right\} dxdy \quad (2.10)$$

For a lossy waveguide case, the propagation constant can be written into its real and imaginary parts as: $k_u = \beta_u + i\alpha_u/2$. Here β_u and α_u represent the phase propagation constant and attenuation coefficient, respectively. If we set $A_u(z) = \tilde{A}_u(z)\exp(-0.5\alpha_u z)$ and substitute it into Eq. (2.10), we obtain the following NCE for lossy waveguides:

$$\frac{\partial A_u}{\partial z} = -\frac{\alpha_u}{2} A_u + \frac{i\omega}{4} \exp(-i\beta_u z) \iint \left\{ \vec{P}^{NL} \cdot \vec{E}_u{}'(x,y) \right\} dxdy \quad (2.11)$$

in which the relation of $\vec{E}_u{}' = \vec{E}_u{}'(x,y)\exp(-ik_u z) = \vec{E}_u{}'(x,y)\exp(-i\beta_u z + 0.5\alpha_u z)$ is used for the derivation. Now, the power of the lossy *u*-th mode along the propagation can be expressed as $P_u(z) = |A_u(z)|^2$.

In $\vec{P}^{NL}$, the part which is irrelevant with the transverse ordinates of (*x*, *y*) can be extracted from the integral term. This means that if we set $\vec{P}^{NL} = \vec{P}^{NL}(x,y)P^{NL}(\mathrm{z})\exp(i\beta^{NL} z)$, we can obtain:

$$\boxed{\frac{\partial A_u}{\partial z} = -\frac{\alpha_u}{2} A_u + \frac{i\omega}{4} P^{NL}(\mathrm{z}) \exp(i\Delta\beta z) \iint \left[\vec{P}^{NL}(x,y) \cdot \vec{E}_u{}'(x,y) \right] dxdy} \quad (2.12)$$

Here $\Delta\beta = \beta^{\mathrm{NL}} - \beta_u$ is the phase mismatch. The integral term can be defined as the nonlinear coupling coefficient:

$$\kappa = \iint \left[\vec{P}^{NL}(x,y) \cdot \vec{E}_u{}'(x,y) \right] dxdy \quad (2.13)$$

which only depends on the mode confinement and overlap integral between interacted modes in the nonlinear areas within the waveguide cross-section. **Eq. (2.12) is the NCE**

in the frequency domain. If we want to obtain the time-domain NCE, we need to take the dispersion (i.e. the dependence of k_u on ω) into account.

Next, we set $A_{u\omega}(z) = \tilde{A}_u(z)\exp(ik_u z) = \tilde{A}_u(z)\exp(i\beta_u z - 0.5\alpha_u z)$ and substitute it into Eq. (2.10). The resulted new equation is:

$$\begin{aligned} &\frac{\partial A_{u\omega}}{\partial z}\exp(-ik_u z) - ik_u A_{u\omega}\exp(-ik_u z) = \frac{i\omega}{4}\iint\left\{\vec{P}^{NL}\cdot\vec{E}_u{}'(x,y)\exp(-ik_u z)\right\}dxdy \\ &\Rightarrow\ \frac{\partial A_{u\omega}}{\partial z} - (i\beta_u - 0.5\alpha_u)A_{u\omega} = \frac{i\omega}{4}\iint\left\{\vec{P}^{NL}\cdot\vec{E}_u{}'(x,y)\right\}dxdy \end{aligned} \tag{2.14}$$

in which we have used the relations of $k_u = \beta_u + i\alpha_u/2$ and $\vec{E}_u{}' = \vec{E}_u{}'(x,y)\exp(-ik_u z)$. Then, by considering the dispersion as $\beta_u(\omega) = \sum_{m=0}^{\infty}\frac{1}{m!}\frac{\partial^m\beta_u}{\partial\omega^m}\Big|_{\omega_0}(\omega-\omega_0)^m = \sum_{m=0}^{\infty}\frac{\beta_{um}}{m!}(\omega-\omega_0)^m$ and $\alpha_u(\omega) = \sum_{m=0}^{\infty}\frac{1}{m!}\frac{\partial^m\alpha_u}{\partial\omega^m}\Big|_{\omega_0}(\omega-\omega_0)^m = \sum_{m=0}^{\infty}\frac{\alpha_{um}}{m!}(\omega-\omega_0)^m$ (where $\beta_{um} = \frac{\partial^m\beta_u}{\partial\omega^m}\Big|_{\omega_0}$ and $\alpha_{um} = \frac{\partial^m\alpha_u}{\partial\omega^m}\Big|_{\omega_0}$ are the m-th dispersion coefficient and loss dispersion coefficient of the u-th mode at the center frequency of ω_0, respectively), we can obtain:

$$\frac{\partial A_{u\omega}}{\partial z} - \sum_{m=0}^{\infty}\frac{i\beta_{um} - 0.5\alpha_{um}}{m!}(\omega-\omega_0)^m A_{u\omega} = \frac{i\omega}{4}\iint\left\{\vec{P}^{NL}\cdot\vec{E}_u{}'(x,y)\right\}dxdy \tag{2.15}$$

Now by implementing an inverse Fourier transformation on both sides of Eq. (2.15), we can get the **NCE in the time domain as**:

$$\boxed{\frac{\partial A_{ut}}{\partial z} - \sum_{m=0}^{\infty}\frac{i^m(i\beta_{um} - 0.5\alpha_{um})}{m!}\frac{\partial^m A_{ut}\exp(i\omega_0 t)}{\partial t^m}\exp(-i\omega_0 t) = -\frac{1}{4}\frac{\partial}{\partial t}\left\{\iint\left[\vec{P}_t^{NL}\cdot\vec{E}_u{}'(x,y)\right]dxdy\right\}} \tag{2.16}$$

where $A_{ut} = \mathcal{F}^{-1}(A_{u\omega})$ and $P_t^{NL} = \mathcal{F}^{-1}(P^{NL})$ are the inverse Fourier transforms of $A_{u\omega}$ and P^{NL}, respectively.

Based on the NCE expressed in Eqs. (2.12) and (2.16), we can analyze different kinds of nonlinear processes. The frequency domain form of Eq. (2.12) is applicable for the continuous wave case, while the time domain form given by Eq. (2.16) can be applied in the pulse wave analysis. The only difference between various nonlinear effects lies in the expression of the nonlinear polarization $\vec{P}^{NL}$ term dependence over the electrical field. For example, when considering a common degenerate four-wave mixing process, where a single pump wave ω_p provides amplification for a neighbored signal wave ω_s and generates an idler wave on the other side of the pump through a third-order optical nonlinearity ($\omega_i = 2\omega_p - \omega_s$), the $\vec{P}^{NL}$ at different frequencies are:

$$\begin{aligned}
\vec{P}_s^{NL} &= \frac{3}{4}\varepsilon_0 A_p A_p A_i^* \exp[i(2\beta_p - \beta_i)z]\chi^{(3)} \vdots \vec{E}_p(x,y)\vec{E}_p(x,y)\vec{E}_i^*(x,y) \\
\vec{P}_i^{NL} &= \frac{3}{4}\varepsilon_0 A_p A_p A_s^* \exp[i(2\beta_p - \beta_s)z]\chi^{(3)} \vdots \vec{E}_p(x,y)\vec{E}_p(x,y)\vec{E}_s^*(x,y) \\
\vec{P}_p^{NL} &= \frac{3}{2}\varepsilon_0 A_s A_i A_p^* \exp[i(\beta_s + \beta_i - \beta_p)z]\chi^{(3)} \vdots \vec{E}_p(x,y)\vec{E}_p(x,y)\vec{E}_i^*(x,y)
\end{aligned} \tag{2.17}$$

where $\chi^{(3)}$ is the third-order nonlinear susceptibility. The asterisk represents the conjugate term.

2.2.2 Principles to enhance nonlinear effects

In general, nonlinear effects are very weak especially for high-order nonlinear processes due to the small magnitude of nonlinear susceptibilities. As a result, in order to excite efficient nonlinear processes, high pump powers and long propagation lengths are typically needed. For example in the most common used nonlinear silicon nanowire waveguides with dimensions of 220 nm × 450 nm, the nonlinear length is as long as 8 mm for an optical pulse with power of 0.2 W [57]. How to enhance the nonlinear effects is pretty essential for the purpose of reducing the power consumption and footprint of optical devices.

In the next, we will discuss the key factors to enhance the nonlinear efficiency in term of the former derived NCE. Firstly, let us list all the key factors as follows:

- Nonlinear materials with large nonlinear susceptibilities are needed.
- Long distances of interaction between light and matter are expected.
- Phase matching conditions are required in parametric processes.
- Strong optical mode confinement and large overlap integrals between interacted modes are welcome.

Firstly, the most intuitional way is to select nonlinear materials with the highest possible nonlinear susceptibilities. As can be seen in Eq. (2.17), nonlinear polarizations at every frequency are linearly proportional to the nonlinear susceptibility. In this direction, many kinds of efficient nonlinear materials have been proposed for the exploitation of second or third orders nonlinear optical processes [118, 119]. As to our concern, we mainly focused on nonlinear materials compatible with the silicon photonics platform. The most used nonlinear materials include silicon itself [120-123], silicon dioxide (in fiber nonlinearity), and newly reported silicon nitride and Hydex [124]. Recently, organic polymers have also attracted a growing attention for nonlinear applications in silicon photonics due to their excellent properties of low linear loss, large nonlinear coefficients and removal of carrier effects, especially for electro-optical (EO) modulation and carrier-free ultrafast optical applications [34-37, 125-127]. More recently, the two dimensional graphene material has been also proposed as a new competitive nonlinear material owing to its large nonlinear coefficient in a broad band and electrical tunability [128-131].

Table 2.1 lists the EO coefficients of various second order nonlinear materials. EO coefficient r and second-order susceptibility $\chi^{(2)}$ are interrelated by $r = -2\chi^{(2)}/n^4$ [35]. The first material is the most commonly used EO material lithium niobate ($LiNbO_3$), while the other materials are EO polymers. It is clear that the EO coefficients of polymers are one order of magnitude larger than that in $LiNbO_3$. Table 2.2 gives the nonlinear index coefficients of different kinds of third order nonlinear materials which are compatible with the CMOS platform. Nonlinear index coefficient n_2 and third-order

susceptibility $\chi^{(3)}$ are interrelated by $n_2 = 3\mathrm{Re}[\chi^{(3)}]/4\varepsilon_0 c n^2$ [35]. Similarly, polymers show the best performance with respect to the reachable nonlinear coefficients.

Materials	**λ (nm)**	***n***	**r_{33} (pm/V)**	**Ref.**
$LiNbO_3$	1550	2.2	30	[46]
Doped, crosslinked organic polymer	1550	1.643	170	[132]
AJ404L	1550	1.6	150	[133]
M3	1550	1.68	70	[42]
YLD124/PSLD41 (25:75 wt.%)	1540	1.73	230	[134]

Table 2.1 Electrooptic coefficients for various second order nonlinear materials.

Materials	**λ (nm)**	***n***	**n_2 (m^2/W)**	**Carrier limited**	**Ref.**
Silicon	1550	3.48	4.5×10^{-18}	Yes	[32]
Silicon dioxide	1550	1.45	2.5×10^{-20}	No	[56]
Silicon nitride	1550	1.989	2.5×10^{-19}	No	[124]
Hydex	1550	1.5-1.9	1.15×10^{-19}	No	[124]
DDMEBT	1500	1.8	1.7×10^{-17}	No	[135]

Table 2.2 Nonlinear coefficients for various third order nonlinear materials.

As a matter of fact, there also exists drawbacks for organic polymers. Their integration onto silicon is usually realized by using spin-coating technique. In this technique, most of the material is spun off the wafer during this technological step, which is not suitable for low-cost large-scale manufacturing. While the deposition of SiO_2 and Si_3N_4 is usually realized by plasma enhanced chemical vapor deposition (PECVD) technique. Another drawback of organic polymers is that their short- and long-term stability especially with regard to temperature should be improved. Their performance deteriorates at high temperature. Fortunately, efforts have made to address this problem [136]. In spite of these weaknesses, their excellent nonlinear properties are interesting enough to investigate possible optical functions with low power, which is precisely what we have done within this manuscript.

In a word, the research on better nonlinear materials is always the most

fundamental and effective way to realize high-performance nonlinear devices and progress in this domain is still on-going.

The second key factor is to increase the interaction distance between light and matter. Mathematically speaking, the contribution of the first term on the right side (i.e. loss term) of Eqs. (2.12) and Eq. (2.16) lies in adding an exponential decay into the amplitude solution of the NCE. As nonlinear effects depend on energy density, this means that the strength of nonlinear interaction scales down with the loss level. In nonlinear optics, the effective length is typically expressed as $L_{\text{eff}} = (1 - e^{-\alpha L})/\alpha$ with L and α being the practical length and attenuation coefficient of the nonlinear waveguide, respectively. This means that no matter how long the practical waveguide is, the effective length is always less than a maximum of the propagation length $1/\alpha$, i.e. inversely proportional to the loss. Therefore, in order to have a long light-matter interaction distance, the loss level of the waveguide should be as small as possible.

The loss of a waveguide comes from two aspects: material absorption and scattering loss due to bending and roughness of the sidewalls. Thus the issue can be considered both from the material and fabrication points of view. Firstly, we need to use nonlinear materials with low loss. For example, as already mentioned in Chapter 1, polymers are considered to be better than silicon due to the existence of two photon absorption and concomitant free carrier absorption in silicon for high optical powers in the near-infrared wavelength range. For plasmonic materials, people tend to use noble metals such as silver and gold with relatively low losses [48]. In addition, the loss of the plasmonic mode propagating along a metal-dielectric interface decreases for dielectric with smaller refractive index, which further reinforces the advantage of low-index polymer in plasmonic structures. Secondly, the fabrication procedure should be optimized in order to realize smooth waveguide etched sidewalls. In the same time, as presented in the mode analysis of plasmonic slot and hybrid plasmonic waveguides in Section 2.1, in plasmonic waveguides the loss is also strongly relevant to the geometrical dimension of the waveguide. Besides, an important feature of waveguide

size is that it affects the phase matching, as shown hereafter. For these two reasons, the geometrical parameters of plasmonic waveguides need a careful appropriate design.

The third aspect that needs to be considered is the phase matching. In order to satisfy the phase matching condition (PMC), the most popular methods include birefringence, quasi-phase-matching (QPM) and mode phase-matching (MPM) techniques [137]. Birefringence is the dependence of the refractive index on the direction of polarization of the optical radiation. By making use of this, it is possible to achieve the PMC between the interacting frequencies with different polarizations [52]. QPM is one of the most effective techniques for the attainment of phase matching in a material that lacks birefringence and is achieved through periodic modulation of the nonlinear coefficient [138]. However, in silicon plasmonic waveguides, it is not easy to use these two approaches. On the one hand, plasmonic waveguides usually can support only one kind of polarization mode, and most of the silicon-compatible nonlinear materials show little birefringence. On the other hand, periodical poling in a compact plasmonic waveguide is difficult and will increase the cost and complexity of the device. The MPM method for achieving PMC is to make use of the distinction of modal dispersion properties between different frequencies. In general, waveguides can support several modes, and the mode effective refractive indices of higher-order modes are lower. Therefore it is possible to achieve the PMC if the higher frequency propagates at a higher-order mode while the low one propagates at a lower-order mode. This approach is simple because it does not require any additional technological step after the waveguide fabrication. The MPM is usually realized by tuning the geometrical parameters of the waveguide cross section and has been widely demonstrated as an effective method to achieve PMC in plasmonic waveguides between optical and plasmonic modes [139, 140] or plasmonic modes with different orders [141] or symmetries [142, 143].

The last key factor to realize considerable nonlinear effects is the tight optical confinement, or in other words, enlarging the overlap integral item between interacting

modes in Eqs. (2.12) and (2.16). This is obvious since nonlinear effects are dependent on optical intensity. Actually, after removing the complex mode amplitude items from the nonlinear polarization, the integral item in Eqs. (2.12) and (2.16) is exactly the effective nonlinear coefficient of a nonlinear waveguide that people have commonly used in nonlinear analysis, such as the interaction factor Γ or the effective index susceptibility γ for the EO effects [36, 144], nonlinear coefficients for nonlinear silicon waveguides [29] or Kerr nonlinear coefficients in subwavelength waveguides [145].

The first step to address this issue is to excite nonlinear effects in miniature waveguides with a cross-sectional area on the micrometre scale and below. This approach has already led to major breakthroughs, for instance signal regeneration using low-power four-wave mixing in a silicon nanowaveguide [11]. The optical confinement can be further increased in silicon slot and photonic crystal waveguides [9, 83]. Except from such slot waveguide effects motivated in the cross section of a waveguide, the other way to increase the optical field confinement lies in introducing resonant structures or slow light effects in the propagation direction. As we know it, the optical field is enhanced around the resonant wavelength in a resonant structure such as in microring resonators, gratings or microcavities [146]. The enhancement factor is proportional to the quality factor of the resonator. Thus, resonant structures with high quality factor are often used to enhance nonlinear effects. Slow light is considered to provide another opportunity for further enhancement. When an optical pulse travels in a slow-light waveguide, it is compressed and its energy density is thereby increased [147]. The second and third order optical nonlinearity enhancement is proportional to the group index squared n_g^2 [148]. Understanding slow light from another aspect, it can extend the interaction time between light and matter within the same waveguide length due to the slower light group velocity, thus can enhance the nonlinear interactions. As mentioned before, for all-dielectric waveguides, the optical field confinement is limited to the diffraction limit. In contrast, plasmonic waveguides can provide a true nano-scale waveguiding and confinement of light, which makes plasmonic waveguides enabling

the tightest confinement of light.

In order to have a more visual understanding, we next give a comparison of the third order Kerr nonlinearity between a silicon slot waveguide (SSW) and a plasmonic slot waveguide (PSW) with same slot cross-sectional sizes. For the Kerr nonlinearity in a waveguide, a Kerr nonlinear coefficient γ is often used to evaluate the nonlinear magnitude. According to the full vectorial nonlinear model, γ in a subwavelength waveguide is defined as [145]:

$$\gamma = \frac{2\pi}{\lambda}\frac{\bar{n}_2}{A_{\text{eff}}} \tag{2.18}$$

Here λ is the optical wavelength in free space, $\bar{n}_2$ is the nonlinear refractive index averaged over an inhomogeneous cross section weighted with respect to field distribution, and A_{eff} is the effective mode area. They are expressed as [145]:

$$\begin{aligned} \bar{n}_2 &= \frac{\varepsilon_0}{\mu_0}\frac{\int n^2(x,y)n_2(x,y)[2|\vec{E}|^4+|\vec{E}^2|^2]dxdy}{3|\int S_z dxdy|^2} \\ A_{\text{eff}} &= |\iint S_z dxdy|^2 / \iint |S_z|^2 \cdot dxdy \end{aligned} \tag{2.19}$$

where $S_z = (\vec{E}\times\vec{H})\cdot e_z$ (e_z is the unit vector in z direction). $n(x, y)$ and $n_2(x, y)$ are the linear and nonlinear refractive index distribution within the cross-section, respectively.

The comparative results are given in Table 2.3. The cross-sectional size of two slots is 157 nm wide and 220 nm high. The width of two silicon wires in the SSW is 216 nm, which comes from the reported highly nonlinear SSW in [38]. One sees that the PSW has a smaller effective mode area and a larger nonlinear coefficient over one order of magnitude, which means tighter confinement and thus facilitates stronger nonlinearity. Meanwhile, the loss of PSW is much larger than that in SSW due to the existence of metal. In the next, we will yet see that the large nonlinear coefficient and loss in silicon plasmonic waveguides make them applicable for short-distance strong nonlinear effects, while hinders them in long distance nonlinear applications.

Waveguide structure	Silicon slot[a]	Plasmonic slot[b]
Mode profile	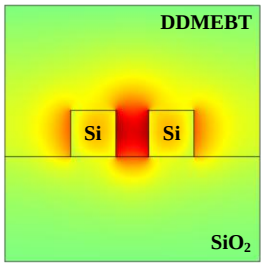	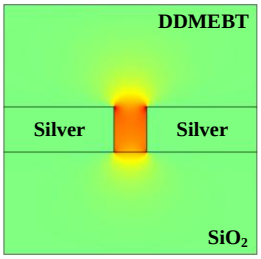
A_{eff} (m^2)	3.64×10^{-13}	8.37×10^{-14}
γ ($m^{-1}W^{-1}$)	104*	1326
α (dB/mm)	1.6*	132.2
L_p (μm)	2714*	32.85

Table 2.3 Kerr nonlinearity in silicon slot waveguide and plasmonic slot waveguide.

[a]Slot is 157 nm wide and formed by two 216 nm × 220 nm silicon wires [38].

[b]Slot has same size with the one in silicon slot i.e. 157 nm × 220 nm.

*Parameters obtained from [38]. Other parameters are calculated using Eqs. (2.18) and (2.19) by a finite element simulation.

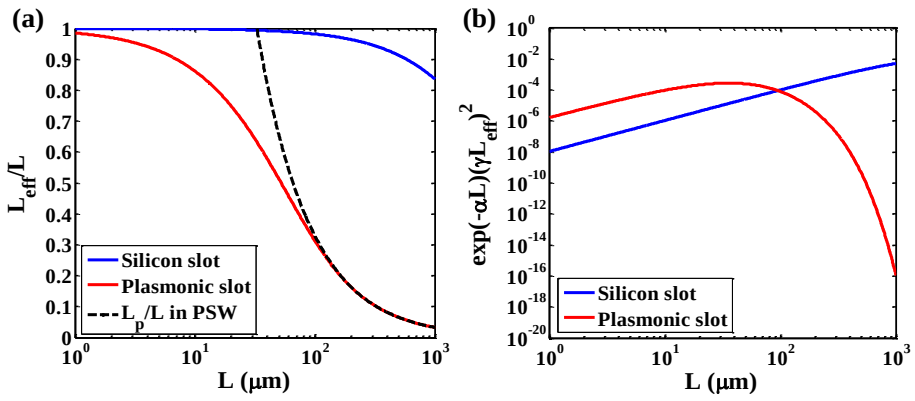

Fig. 2.8 (a) Effective length and (b) efficiency factor of third order nonlinear process in silicon slot waveguide and plasmonic slot waveguide from Table 2.3.

We take here the case of the degenerate four-wave mixing (FWM) process as an example, whose efficiency in a waveguide is proportional to the factor of $\eta \propto \exp(-\alpha L)(\gamma L_{eff})^2$ [38]. L is the practical length of the waveguide and L_{eff} is the effective length being defined as $L_{eff} = [1-\exp(-\alpha L)]/\alpha$. Fig. 2.8 plots the effective length and FWM efficiency factor as a function of the waveguide length. The parameters of the SSW and

PSW are taken from Table 2.3. The black dashed line in Fig. 2.8(a) is the propagation length of PSW divided by the length, which is always larger than the effective length. After a propagation length of around 100 μm, the effective length nearly reaches its maximum, i.e. the propagation length. But the effective length becomes smaller and smaller compared with the waveguide length for larger waveguide lengths, while for a short waveguide, the effective length is only slightly reduced when compared with the waveguide length (L_{eff}/L = 0.8 when L = 15 μm). In Fig. 2.8(b) the FWM efficiency factor in PSW is larger than that in low-loss SSW when the waveguide is shorter than 96 μm. This can be explained as follows. In the beginning, the loss has little influence on the FWM efficiency due to the short length. Thus the PSW with larger nonlinear coefficient supports larger FWM efficiency, and the efficiency increases as length increases. After a length of around the propagation length, the loss begins to counteract the conversion from the nonlinear process, thus the FWM efficiency decreases. Here the peak efficiency happens at L = 36 μm ~ L_p = 32.85 μm. For this length, the loss of SSW has no influence on the efficiency. These features highlight the potential interest of PSW as compact devices, as the effectiveness of long PSW is limited by linear propagation losses, at least with current technology.

In conclusion, even with larger losses, plasmonic waveguides show superiority over dielectric ones for nonlinear applications when lengths are kept compact, specifically no more than several propagation lengths. The ability to realize efficient nonlinear effects within short distance makes plasmonic waveguides a promising platform for ultra-compact on-chip optical signal processing and communications.

In this dissertation, we have taken the four key factors giving rise to strong nonlinear effects into consideration. Regarding the materials' choices, nonlinear polymers with large nonlinear susceptibilities and low loss will be considered as the active nonlinear materials in the investigations described in next chapters, with silver and gold to realize the metallic layers. With respect to their cross-section geometry, silicon plasmonic waveguides with tight field confinement and nice compatibility with

the silicon photonic platform will be considered. Regarding the phase matching conditions, mode phase matching method will be utilized. Based on whole framework, we will proposed enhanced nonlinear effects in plasmonic slot and hybrid plasmonic waveguides, and investigate some of their possible applications for on-chip nonlinear optical signal processing, such as phase regeneration, modulation and detection.

Chapter 3

Enhancement of nonlinear effects using plasmonic slot waveguides

As seen in Chapter 2, plasmonic slot waveguides (PSW) have the ability to squeeze light far below the diffraction limit. The field enhancement at subwavelength scale is really helpful to realize effective nonlinear effects, and based on the supported nanoscale nonlinear effects, compact optical functionalities can thus be envisaged. Meanwhile, the metallic slabs that define the PSW can also serve as electrodes for the generation of a high electric field with low applied voltages. This feature makes PSW suitable for realizing optoelectronic components with low power consumption. Lastly, PSW has the simplest configuration among all the proposed plasmonic waveguides. It is reasonably easy to fabricate them experimentally with standard nano-fabrication techniques.

This chapter will detail numerical investigation of three nonlinear applications exploiting PSW, including enhanced second harmonic generation (SHG), high-speed electro-optic (EO) modulation mechanism based on the electrically controlled SHG, and on-chip high-speed optical detection based on the optical rectification effect.

The rest of the chapter is organized as follows.

In section 3.1, we investigate the most fundamental nonlinear effect, i.e. SHG in PSW. By optimizing the waveguide geometry and exploiting the mode phase matching method, a normalized SHG efficiency more than 1×10^5 $W^{-1}cm^{-2}$ is predicted within a PSW length shorter than 20 μm.

In section 3.2, we go a step further and take both the second order and third order nonlinearities of the considered polymer into consideration at the same time. By applying an electrical signal between the two metallic slabs, electrically controlled SHG

in an integrated waveguide is proposed. The corresponding intensity and phase modulation magnitudes are predicted to be 8 μW/V and 0.12 π/V, respectively. We then consider this process as a possible mechanism of ultra-high speed EO modulation.

In section 3.3, we finally investigate the inverse process of the EO effect, i.e. the optical rectification effect, and apply it for a broadband high-speed optical detection. The proposed detector characterizes a relatively flat response for a wide optical band from 1.25 μm to 1.7 μm and supports a RF cut-off frequency up to 800 GHz.

3.1 Enhanced second harmonic generation in plasmonic slot waveguides

3.1.1 Introduction

Among all the nonlinear processes, second harmonic generation (SHG) is frequently studied for its simple theoretical principle, reasonable easiness for demonstration in experiments, and various interesting applications [52]. In silicon photonics, however, SHG cannot be excited directly in silicon because the second-order susceptibility vanishes in this material owing to crystal centro-symmetry. Exploitation of silicon nitride (Si_3N_4) has been proposed to circumvent this drawback and induce second-order nonlinear processes in silicon compatible structures [149-152]. For now, three mechanisms have been proposed in this purpose. Firstly, $\chi^{(2)}$ can be induced in silicon waveguides by using a stressing Si_3N_4 overlayer. Based on such a waveguide geometry, SHG efficiency of about 5×10^{-8} under a ns pump peak power of around 0.7 W was realized for a length of two millimeters [149]. Secondly, SHG was proposed in a Si_3N_4 ring resonator due to the break of centrosymmetry at the interface between the waveguide and the silica cladding. J. S. Levy et al. observed in a 116 μm ring radius resonator a conversion efficiency of 2.86×10^{-4} with a 100 μW of second harmonic frequency (SHF) signal generated for a fundamental frequency (FF) pump power of 315 mW [150]. More recently, R. E. P. de Oliveira et al. reported SHG in a 20 μm

radius Si_3N_4 ring resonator by using the electric-field induced SHG process and calculated a conversion efficiency of around 3.68×10^{-3} with a pumping power of 75 mW [151].

From Chapter 1, we know that plasmonic based nonlinear devices are among the most promising candidates to further increase the efficiency of SHG and reduce the sizes of devices due to the ability to allow strong local-enhanced confinement of light beyond the limits imposed by the laws of diffraction in dielectric media [20, 153, 154]. Another advantage of plasmonic structures is that they can respond on the timescale of a few femtoseconds. Many kinds of nonlinear plasmonic structures have been proposed for realizing efficient SHG, such as in plasmonic slot waveguides (PSW) [141, 143, 155], long-range plasmonic waveguides [156], hybrid plasmonic waveguides (HPW) [109], metal surfaces with nanoscale roughness [157], individual metallic nanoaperture [158], plasmonic particle chains [159], and plasmonic core-shell nanowires [160]. To date, the most used nonlinear material in these structures to realize SHG is lithium niobate ($LiNbO_3$) [109, 141, 143, 156]. However, in spite of the generally used continuous wave (CW) pump power of the FF to around 1 W, the peak powers of the generated SHF are usually limited to 10^{-5} W [141, 143, 156]. Even if it can go up to 10^{-2} W in HPW, the corresponding waveguide length to realize this efficiency is one millimeter [109], which is probably too long and not suitable for applications into future integrated nanophotonic circuits. The rather small reported efficiencies are due to the relatively small nonlinear susceptibility in $LiNbO_3$, the moderately large nonlinear coupling coefficients (NCC) between different frequencies, and the absorption loss of the plasmonic modes. Furthermore, $LiNbO_3$ is not easily compatible with silicon photonics, which represents the best solution for high yield and mass production with low cost [161]. In the same time, the aforementioned nonlinear polymers (NP) which have nonlinear susceptibilities exceeding those of $LiNbO_3$ and can be integrated into silicon photonic structures have drawn more and more attention for nonlinear optics and all-optical high-speed signal processing [34, 35, 38]. For example, Wenshan Cai et

al. demonstrated experimentally an electrically controlled SHG in plasmonic slot with NP in the slot [155]. More recently, L. Alloatti et al. reported an impressive second-order normalized conversion efficiency up to 2900% $W^{-1}cm^{-2}$ based on a silicon-organic hybrid (SOH) waveguide [162].

Hence, structures combining the plasmonics and NP have a great potential for nonlinear nano-optics. Here, we propose a second-order nonlinear PSW configuration in hybrid polymer-silicon photonics. To theoretically investigate the potentials of this approach, we consider a NP with high $\chi^{(2)}$ as its core nonlinear material. This waveguide is able to tightly confine fields in the subwavelength nonlinear slot both at FF and SHF [71], which is crucial to efficiently maximize the nonlinear interaction. In addition, the theoretically considered structures can potentially be fabricated with state-of-the-art silicon compatible fabrication techniques [155]. With a careful choice of the opto-geometrical parameters, the phase-matched SHG at the FF wavelength corresponding to λ_{FF} = 1550 nm induced in the proposed waveguide is analyzed by numerical simulations. Then, the SHG performance of the structure is modified by enhancing the asymmetry of the PSW. In the new proposed geometry, the nonlinear coupling coefficients are significantly enhanced, leading to prediction of highly efficient SHG with low pump power (≤ 10 mW) and short waveguide length (≤ 20 μm).

3.1.2 Waveguide structure and nonlinear modeling approach

Figure 3.1 shows the cross-section of the proposed waveguide geometry, which is similar to the one reported in [141] for a $LiNbO_3$-based structure, and with a $\chi^{(2)}$ polymer infiltrated into a metallic slot. The width and height of the NP region are *w* and *h*, respectively. The considered polymer is the doped, crosslinked organic polymer with a refractive index of n = 1.643 and an EO coefficient of r_{33} = 170 pm/V at the wavelength of 1550 nm [35, 132]. Based on the conversion equation $\left|\chi^{(2)}_{lmn}\right| = \delta_{1l}\delta_{1m}\delta_{1n}n^4\left|r_{lmn}\right|/2$ [163], the corresponding NP second-order nonlinear

susceptibility $\left|\chi_{111}^{(2)}\right|$ = 619.4 pm/V can be obtained. Metal is defined here as silver due to its relatively low loss in the calculated wavelength range and with a Drude permittivity dispersion given by $\varepsilon_{Ag} = \varepsilon_\infty - \omega_p / \left[\omega\left(\omega + i\gamma\right)\right]$, with ε_∞ = 3.7, ω_p = 9.2 eV and γ = 0.02 eV [49].

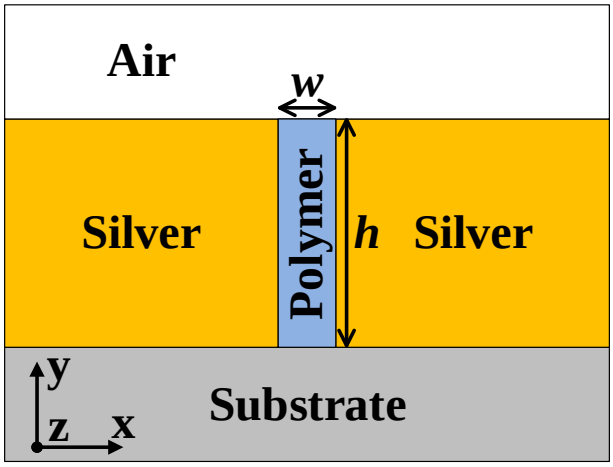

Fig. 3.1 Schematic cross-section of the proposed plasmonic slot waveguide with $\chi^{(2)}$ nonlinear polymer infiltrating into the slot and substrate compatible with SOI platform.

In order to couple light into such a PSW from a standard silicon waveguide, Z. Han et al. proposed experimentally a Si-plasmonic taper coupler, where a 30% coupling efficiency was reported [72]. More recently, R. Thomas et al. presented theoretically a specially designed coupler with a short taper length to couple light into a PSW, where a maximum coupling efficiency of 72% into a 20 nm slot was predicted [164].

Based on the former proposed nonlinear coupled-wave equations (NCE) in chapter 2, we can analyze different kinds of nonlinear processes. In the present case under consideration about the SHG process, the FF ω_{FF} is converted into the SHF $\omega_{SH} = 2\omega_{FF}$, and the nonlinear polarization terms at FF and SHF are $\vec{P}_{FF}^{NL} = \varepsilon_0 \chi^{(2)} : \vec{E}_{SH} \vec{E}_{FF}^{*}$ and $\vec{P}_{SH}^{NL} = 0.5\varepsilon_0 \chi^{(2)} : \vec{E}_{FF} \vec{E}_{FF}$, respectively. If we consider a single given guided mode both at FF and SHF, the NCEs describing the SHG process in the nonlinear waveguide are:

$$\frac{\partial A_{FF}}{\partial z} = -\frac{\alpha_{FF}}{2} A_{FF} + i\frac{\omega_{FF}}{4}\kappa_{FF} A_{FF}^{*} A_{SH} \exp(i\Delta\beta z)$$
$$\frac{\partial A_{SH}}{\partial z} = -\frac{\alpha_{SH}}{2} A_{SH} + i\frac{\omega_{FF}}{4}\kappa_{SH} A_{FF} A_{FF} \exp(-i\Delta\beta z) \quad (3.1)$$

where $\Delta\beta = \beta_{SH} - 2\beta_{FF}$ is the phase mismatch and $\kappa_{FF,SH}$ are the nonlinear coupling coefficients (NCC), which are defined by [139]:

$$\kappa_{FF} = \varepsilon_0 \iint \left\{ \chi^{(2)} : \vec{E}_{SH}(x,y)\vec{E}_{FF}^{*}(x,y) \cdot \vec{E}_{FF}{}'(x,y) \right\} dxdy$$
$$\kappa_{SH} = \varepsilon_0 \iint \left\{ \chi^{(2)} : \vec{E}_{FF}(x,y)\vec{E}_{FF}(x,y) \cdot \vec{E}_{SH}{}'(x,y) \right\} dxdy \quad (3.2)$$

Note that the $\chi^{(2)}$ in two NCC are different in terms of principle. The complete forms are $\chi^{(2)}(-\omega; 2\omega, -\omega)$ at FF and $\chi^{(2)}(-2\omega; \omega, \omega)$ at SHF, respectively. However, if all the involved optical frequencies are much smaller than the lowest resonance frequency of the nonlinear material system, which is apparently satisfied here, the nonlinear susceptibility would be dispersionless. Thus, we have taken the same value of $\chi^{(2)}$ at two frequencies. Besides, the longitudinal components of the modes are neglected in the NCC calculations because the transverse components of both the hybrid modes and the nonlinear susceptibility dominate all over other components.

Then, we give the definition of the normalized conversion efficiency as a factor of merit with which we propose here to quantify the efficiency of SHG conversion process:

$$\eta = \frac{P_{SH}(L_p)}{\left[P_{FF}(0)\right]^2 \left[L_p(cm)\right]^2} \quad (3.3)$$

where $P_{FF}(0)$ is the pump power of the FF, L_p is the length when SHF reaches its maximum (defined as peak position) and $P_{SH}(L_p)$ is the corresponding maximum output power, respectively. This allows better assessment of the conversion process since it takes the conversion efficiency $\eta_p = P_{SH}(L_p)/P_{FF}(0)$ (to be maximized), the pump power of the FF wave (to be minimized), and the needed device length (to be minimized) simultaneously into account. It should be noted that this definition is slightly different

from the standard one in a lossless waveguide, where the waveguide length is fixed. As the optimized device length L_p varies here with the pump power, different losses for the FF and SHF are indeed obtained, meaning a variable normalized conversion efficiency under variations of the pump power.

The key factors to increase the SHG efficiency both in terms of higher $\omega_{FF} \rightarrow \omega_{SH}$ conversion yield and smaller device footprint are the reduction of propagation attenuation, the good filling of the phase matching condition (PMC) (i.e. $\Delta\beta = 0$), and the achievement of large coupling coefficients $\kappa_{FF,SH}$ [59]. In the PSW under study here, these three factors can be fulfilled and/or optimized by adjusting the waveguide opto-geometrical parameters.

In order to reduce the propagation attenuation, let us first remind that the metal was chosen as Ag due to its relatively low losses and that to further minimize the PSW propagation losses, a polymer with a relatively low index of 1.643 is considered. The choice of the slot width w, however, results from a trade-off between the accepted loss level increasing and the obtained field-induced nonlinear effect enhancement by lowering w. Besides, an important feature of w is that it affects the PMC, as shown hereafter. For these two reasons, this parameter needs a careful appropriate design.

With respect to the PMC, we adopt the mode phase matching method in the present paper, first in the simplest possible configuration before extending it to improve the SHG efficiency as shown hereafter in section 3.1.4. Figure 3.2(a) shows the effective indices of the two guided modes as functions of the slot height h for a free space FF wavelength of 1550 nm and a slot width w = 50 nm. The red and blue lines represent the obtained effective indices for modes at the FF (λ_{FF} = 1550 nm) and the SHF (λ_{SH} = 775 nm), respectively. We can see that the fundamental mode (labeled 0-th mode) at the FF has a crossing with the second-order mode (labeled 1-st mode) at the SHF indicating a point of PMC. For the considered case of a SiO_2 substrate, which has indices of 1.444 and 1.454 for FF and SHF [47], respectively, the PMC occurs for the

slot height h = 489 nm. At this point, the effective indices for the FF and the SHF are 2.2068 + 0.0068i and 2.2069 + 0.0063i, respectively. The corresponding E_x distributions of the different modes are plotted in Fig. 3.2(b), (c) and (d). All the mode profiles shown here have been calculated by using the finite-element-based commercial COMSOL software.

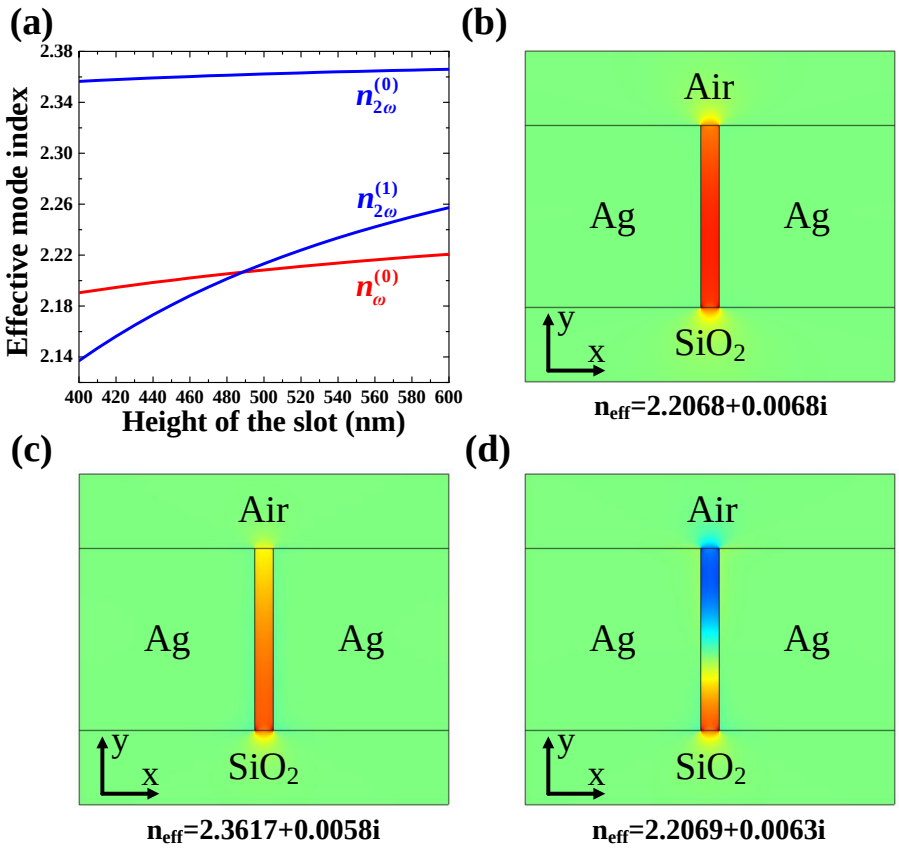

Fig. 3.2 Design of the waveguide geometry for satisfying the PMC. (a) Effective indices of the obtained guided optical modes versus the slot height h for the plasmonic waveguide geometry depicted in (b), (c), (d) in which the slot width is w = 50 nm. Notation "(0)" and "(1)" stand for the fundamental and second-order waveguide modes, respectively, and the signs "ω" and "2ω" correspond to the FF and SHF, respectively. The 1-st mode of the SHF has a crossing with the red line at h = 489 nm indicating a point of phase-matching. E_x distribution of 0-th plasmonic mode at FF (b); 0-th plasmonic mode at SHF (c); and 1-st plasmonic mode at SHF (d) when w = 50 nm, h = 489 nm.

3.1.3 Enhanced SHG in the proposed plasmonic slot waveguide

Now we calculate the SHG for the case of Fig. 3.2 where the 0-th mode at the FF is converted into the 1-st mode at the SHF. The corresponding NCC is calculated to be by doing a post-processing of "surface integration" after mode calculations in COMSOL: $\kappa_{FF} = \kappa_{SH}^{*} = 71\ \mathrm{psm^{-1}W^{-1/2}}$. Figure 3.3 is a plot of the powers of the FF and SHF waves as a function of the propagation distance for an input power of FF source of 1 W. All results presented here and hereafter have been obtained by a numerical simulation of NCE with a self-made Matlab code (please see the detail in the Appendix).

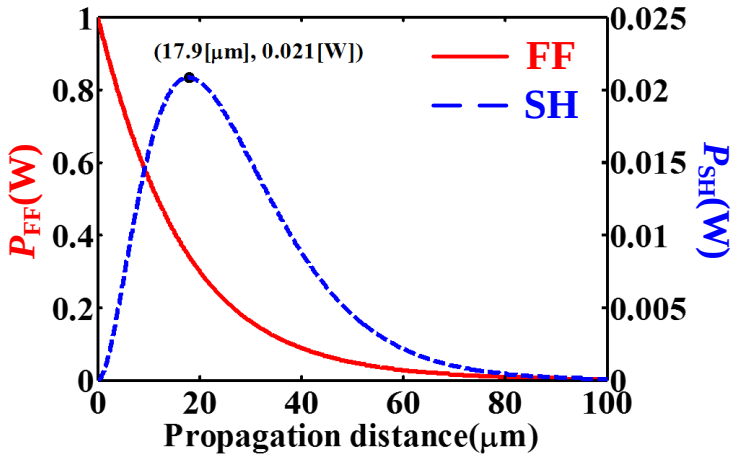

Fig. 3.3. Optical powers of the FF and SHF waves versus the propagation distance for a pump power of 1 W in the structure depicted in Fig. 3.2.

It is shown that a peak power of the generated SHF wave up to 0.021 W is revealed at a propagation length of only 17.9 μm. The corresponding normalized conversion efficiency is $6.55 \times 10^{3}\ \mathrm{W^{-1}cm^{-2}}$. This result is larger than the one obtained in $LiNbO_3$-based PSW devices by about three orders of magnitude with same pump power at the FF [141]. The improvement of the SHG performance mainly results from two aspects. On one hand, the considered polymer has a smaller index compared to $LiNbO_3$. This leads to a larger optical power confined into the nonlinear slot region and to a lower waveguide loss level [71]. On the other hand, the larger $\chi^{(2)}$ in the considered polymer enlarges the coupling coefficients $\kappa_{FF,SH}$.

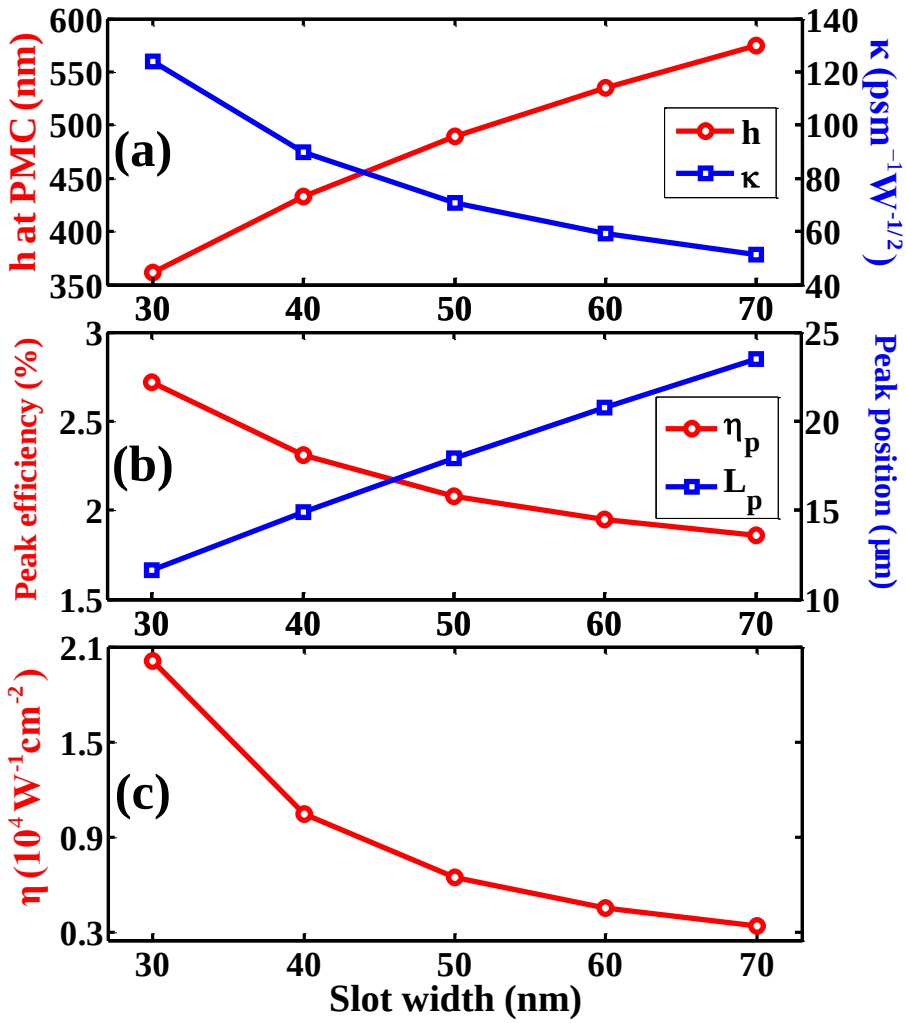

Fig. 3.4. (a) Slot height h to satisfy the PMC needed for the SHG process and associated coupling coefficient κ between the two coupled modes, (b) peak efficiency η_p and peak position L_p of the SHF field, (c) normalized conversion efficiency of the SHG process as functions of the plasmonic slot width under a pump power of 1 W.

Starting from this first result, further improvement is investigated hereafter by adjusting the compromise between the in-slot field confinement and the optical propagation losses. To do so, we analyze the influence of the slot width on the SHG process performance. In Fig. 3.4, the slot height to satisfy the PMC, the nonlinear coupling coefficient (κ), the peak efficiency (η_p) and peak position (L_p) of the SHG process, and the corresponding normalized conversion efficiency (η) are plotted versus the slot width for a FF pumping power of 1 W. As can be seen, when the slot width decreases, the height required to ensure the PMC decreases and the coupling coefficient

increases correspondingly due to the stronger confinement of the field in a smaller area. As a result, the maximum power of SHF increases and the propagation length to realize this efficiency becomes shorter, as is shown in Fig. 3.4(b). The normalized efficiency increases as well. It can be concluded that the PSW has better SHG property with smaller width. However, it is necessary to stress also that the fabrication feasibility should be taken into consideration, so that too narrow slots cannot be considered.

3.1.4 Further improvement of SHG efficiency by tailoring the waveguide asymmetry

What limits the interest of the mode phase-matching method to satisfy the PMC is that the spatial overlap integral between modes with different orders or different symmetries is always less than that between modes with same orders or same symmetries. This in turn results to small nonlinear coupling coefficients (NCC), as defined in Eq. (3.2). For example, we can see in Fig. 3.2(b), that the 0-th mode field distribution at the FF is nearly symmetrical in the nonlinear area. However, in the same time, it is shown in Fig. 3.2(d) that the 1-st mode field distribution at the SHF is nearly anti-symmetrical in the domain of integration. This will inevitably lead to relatively small NCC.

In order to overcome this drawback and enlarge the NCC between the two considered modes, we increase the asymmetry of the PSW by using a Si_3N_4 substrate with larger indices at the FF (n_{Si3N4} = 1.99) and SHF (n_{Si3N4} = 2.1). The new structure is still compatible with silicon photonics. The PMC is satisfied for w = 50 nm and h = 490 nm from Fig. 3.5(a) and the corresponding mode profiles are shown in Fig. 3.5(b), (c) and (d), respectively. At the PMC point, the geometrical size of the waveguide is almost the same as in Fig. 3.2. But the mode profiles become quite asymmetrical especially for the 1-st mode at the SHF. In this case, the calculated NCC is up to 292 $psm^{-1}W^{-1/2}$.

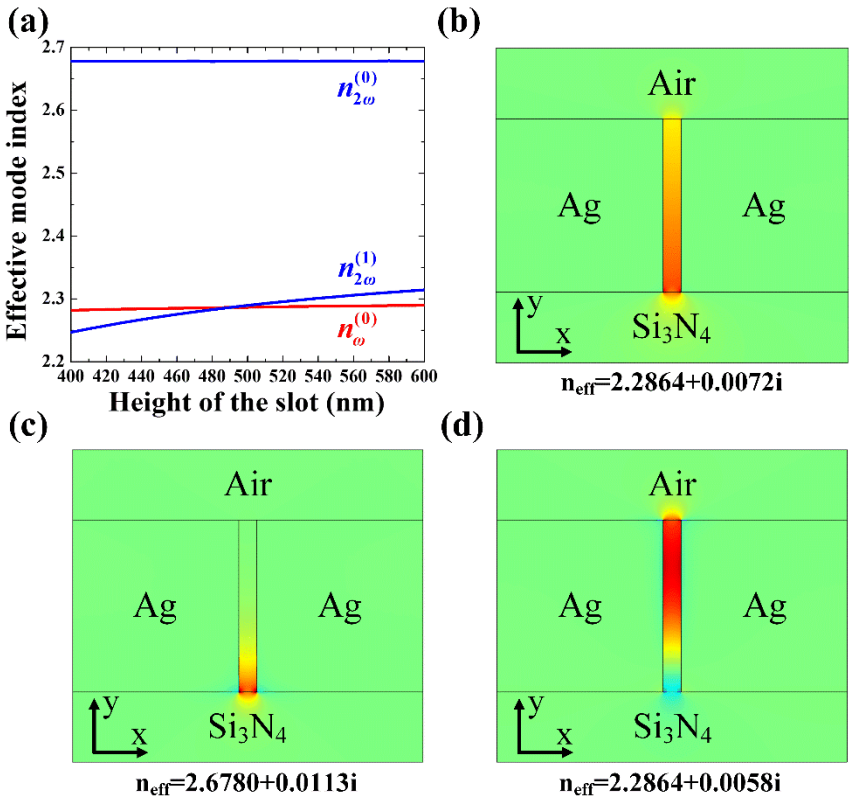

Fig. 3.5. Design of the waveguide with Si_3N_4 substrate for satisfying the PMC. (a) Effective indices of the obtained guided optical modes versus the slot height h for the plasmonic waveguide geometry depicted in (b), (c), (d) in which the slot width is w = 50 nm. E_x distribution of 0-th plasmonic mode at FF (b); 0-th plasmonic mode at SHF (c); and 1-st plasmonic mode at SHF (d) at the phase-matching point (w = 50 nm, h = 490 nm).

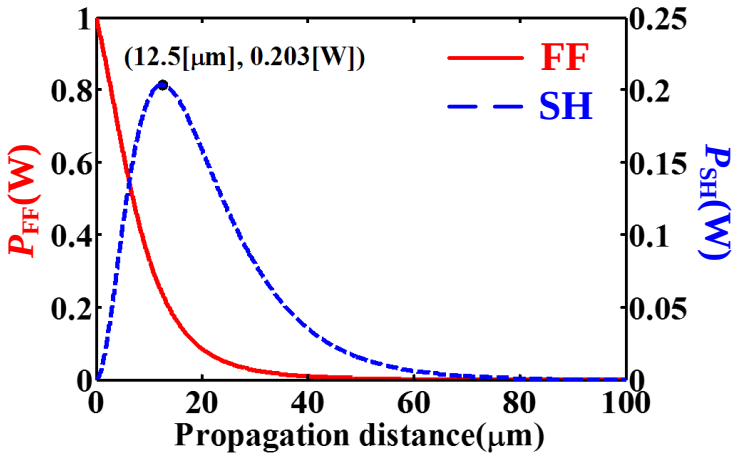

Fig. 3.6. Optical powers of the FF and SHF waves versus the propagation distance for a pump power of 1 W in the structure depicted in Fig. 3.5.

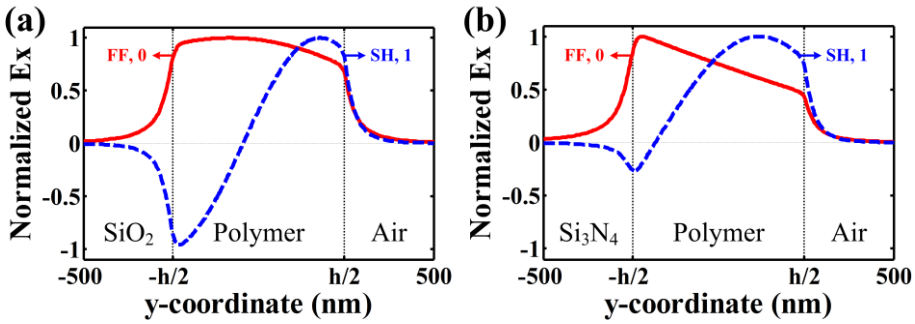

Fig. 3.7. Normalized E_x distribution at x = 0 for the case of SiO_2 substrate (a); Si_3N_4 substrate (b).The red solid line and blue dotted line correspond to 0-th mode at the FF and 1-st mode at the SHF, respectively. The domain between the two vertical lines is the nonlinear area to integrate.

Fig. 3.6 shows the variations of the optical power of the FF and SHF along propagation in this modified waveguide geometry with the same initial condition as in Fig. 3.3. One can see that the maximum efficiency is increased up to 20% and that the propagation length (around 12.5 μm) to realize this efficiency is shorter as well. The normalized conversion efficiency is calculated to $\eta = 1.3 \times 10^5$ $W^{-1}cm^{-2}$, which is over one order of magnitude of further improvement if compared with our starting structure. The principle of this improvement can be seen more clearly in Fig. 3.7, where plots of the normalized E_x distributions along the cutline of x = 0 are shown. For the case of a SiO_2 substrate shown in Fig. 3.7(a), the positive and negative parts of the 1-st mode (blue dotted line) at the SHF have comparable amplitudes, hence making the nonlinear overlap integration with the 0-th mode field small. With respect to the case of Si_3N_4 substrate shown in Fig. 3.7(b), however, the negative part of the 1-st mode becomes negligible in the integration domain. This indicates that the counteraction effect is lower and in turn contributes to the enhancement of the 0-th/1-st NCC. In addition, it should be noted that as the distribution of the generated SHF becomes less symmetric in the modified structure, the in-and-out light coupling efficiency will be easier from/into standard strip silicon waveguides.

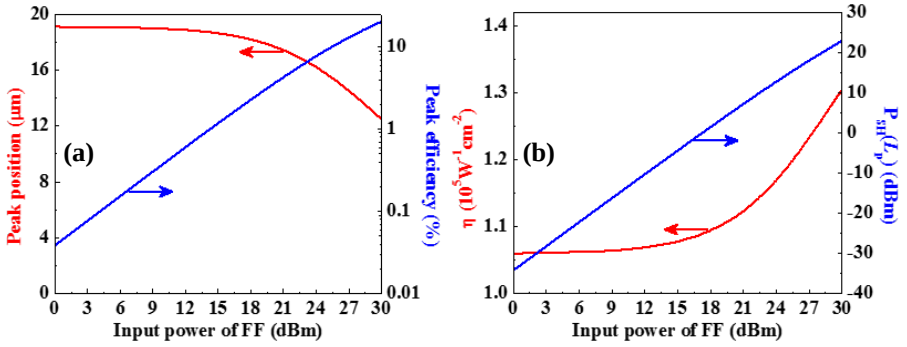

Fig. 3.8. Peak position L_p, peak efficiency η_p, normalized conversion efficiency η and maximum output power $P_{SH}(L_p)$ of SHF versus the input pump power of FF.

In the previous sections, a CW pump power of 1 W was considered to facilitate the direct comparison with the results reported in previous works that considered this pumping condition [109, 141, 156]. However, it should be noted that lowering the pump power is highly desirable and could enable low-power nonlinear all-optical operations amenable to various practical applications in future generations of integrated photonic circuits. Besides, the input power should be chosen carefully so that the intensity in the sub-wavelength slot remains lower than the damage threshold of the material. Since the modified waveguide has so large NCC, we show that the second harmonic can be efficiently generated under low pump power. Figure 3.8(a) shows the peak position and efficiency as a function of the pump power with all other parameters and conditions being the same as in Fig. 3.6. As expected, it is shown that the conversion efficiency is greatly affected by the pump power, while the peak position only moderately varies, and the change of the calculated normalized conversion efficiency is small as well, as it is shown in the left Y-axis of Fig. 3.8(b). We can see that the plasmonic waveguide length remains shorter than 20 μm in all cases, while the normalized conversion efficiency can exceed 1×10^5 $W^{-1}cm^{-2}$. Moreover, it should be emphasized that within this nonlinear PSW, the SHG efficiency still remains around 0.4% even if the input power of the FF is as low as to 10 dBm, which represents a continuous wave optical power easily available. This efficiency is over the one in a Si_3N_4 ring resonator where a pump power of 75 mW was used [151]. Moreover, the optical power of the generated

SHF is then still around 40 μW, as shown in the right Y-axis of Fig. 3.8(b), i.e. is comparable to values reported in previous work that considered a 1 W pumping power [141]. This dramatic improvement makes the proposed plasmonic waveguide geometry very promising and competitive for low-power all-optical signal processing.

3.1.5 Conclusion

In conclusion, we have proposed a silicon compatible nonlinear PSW with a nonlinear polymer infiltrated the metallic slot. For the SHG induced in this PSW, the phase matching condition between the FF and SHF can be satisfied with appropriate designs of the opto-geometrical parameters. Efficient SHG, about three orders of magnitude above the one reported in previous works obtained for $LiNbO_3$-based structures, was demonstrated and the influence of the slot width on SHG efficiency was numerically analyzed. Then, the SHG performance was further improved by one order of magnitude by increasing the spatial asymmetry of the proposed waveguide. In the modified proposed geometry, a normalized SHG conversion efficiency above 1×10^5 $W^{-1}cm^{-2}$ is predicted for a propagation distance shorter than 20 μm. The output power of the SHF generated in the optimized structure for a low pumping power of 10 mW is comparable to the one obtained in previous works for a 1W pumping power. This obtained dramatic improvement of the nonlinear efficiency allows envisaging practical applications using low-power nonlinear SHG-based all-optical signal processing.

3.2 High-speed electro-optical modulator based on electrically controlled second harmonic generation

3.2.1 Introduction

The versatility of plasmonic slot waveguides (PSW) and their strong ability to confine optical fields at nanoscale voids make them suitable for the enhancement of other nonlinear optical mechanisms apart from the simple SHG. With respect to section 3.1, we now investigate an electrical field induced second harmonic generation (EFISHG)

mechanism by making use of an applied electric field.

EFISHG effect, which was first observed in centro-symmetric crystals by applying to them a DC electric field [165], is a frequency-doubling process via four-wave mixing with one of the mixing fields being a DC field or an AC field with a negligible frequency if compared to the optical one. Unlike the conventional second harmonic generation (CSHG) being attributed to the second-order nonlinear susceptibility $\chi^{(2)}(2\omega; \omega, \omega)$, EFISHG arises from its third-order counterpart $\chi^{(3)}(2\omega; \omega, \omega, 0)$, which permits the generation of frequency-doubling radiation in either centro-symmetric or noncentro-symmetric materials. EFISHG has been proposed in several materials or structures without $\chi^{(2)}$, such as in glass [38, 166], semiconductors [167], optical fibers [168], silica waveguides [169] and silicon nitride ring resonators [170]. Applications of EFISHG have also been investigated widely, including the precise measurement of $\chi^{(3)}$ tensors [171], the detection of ultrafast electrical signals [172], the characterization of dielectric surface properties [173], and the probing of carrier dynamics in semiconductors [174].

However, the SH signal generated from EFISHG is usually orders of magnitude smaller than the CSHG contribution. It often requires large voltages (> 100 V) to generate a noticeable EFISHG. Besides, in order to fulfill the phase matching condition (PMC), complex periodic design of electrodes is required [168]. These deficiencies can be modified or simplified by using plasmonic structures. On one hand, the significantly enhanced electromagnetic concentration makes plasmonic structures an ideal platform to support efficient and low-power nonlinear processes [20]. On the other hand, it is possible to satisfy the PMC through the modal phase-matching technique [94, 113]. Lastly, the metallic layers that define the plasmonic structure can also serve as electrodes for the generation of a high DC-like electric field with low applied voltages. In this direction, Cai et al. experimentally reported an electrically controlled second harmonic generation (ECSHG) in a plasmonic nanocavity filled by a nonlinear polymer (NP) [155], where the authors used electric signals to efficiently and linearly control

the SHG in a free-space optics configuration.

In this manuscript, we investigate a planar waveguide integrated counterpart of this approach, which brings several advantages: i) The possible realization of an exact PMC, ii) A good compatibility with the silicon photonics technology. Starting from the work in section 3.1, here we apply an extra control voltage between the two metallic slabs to actively control this efficient SHG. Let us notice that very recently, a high-speed plasmonic phase modulator was experimentally reported based on similar electrically driven PSW [42].

To investigate the performances of this planar PSW approach of EISHG and clearly identify the contributions coming from CSHG and EISHG, we firstly consider a centro-symmetric NP with only $\chi^{(3)}$, where a quadratic control of the power of SH by the voltage is predicted. Then by taking both $\chi^{(2)}$ and $\chi^{(3)}$ into account, the generated SH is almost linearly modulated by the control voltage. At last, we show that this mechanism is able to support small size, efficient intensity and phase modulation for a wide range of voltages with prospectively ultrahigh cut-off electrical frequency.

3.2.2 Waveguide structure and nonlinear modeling approach

Figure 3.9 shows the cross-section of the proposed silicon compatible PSW, which consists of a NP with width *w* and height *h* infiltrated into a metallic slot. Additionally, an extra control voltage (defined as V_c) is applied between the two silver electrodes. In a first step, the NP is chosen as DDMEBT (n = 1.8 and $\chi^{(3)} = 2.3\times10^{-19}$ m^2/V^2), which has been demonstrated as an interesting NP to support high third-order nonlinearity [35]. In a second step, the ECSHG is analyzed for a NP having both $\chi^{(2)}$ and $\chi^{(3)}$ following a similar approach as in [155]. We adopt a typical value of $\chi^{(2)}$ = 230 pm/V for the NP [162] and maintain the original $\chi^{(3)}$ value. The material dispersions of Si_3N_4 and Ag are considered in the simulation. For example, the refractive index of Si_3N_4 is considered to be 1.99 at 1550 nm and 2.1 at 775 nm, while for Ag the Drude model is employed like in [94].

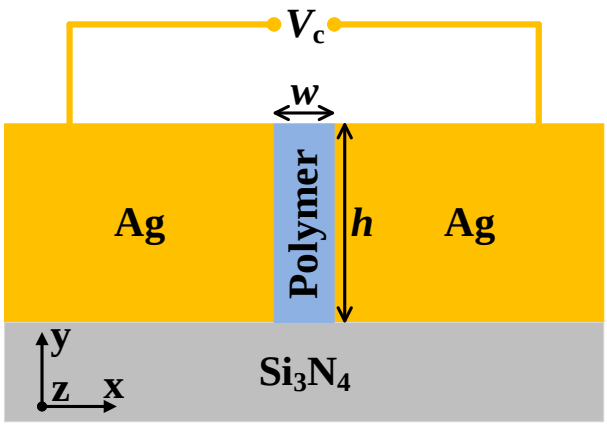

Fig. 3.9 Schematic cross-section of the proposed active plasmonic slot waveguide.

In this PSW, the PMC can be fulfilled between the fundamental (0-th) waveguide mode at fundamental frequency (FF) and the second-order (1-st) waveguide mode at the second harmonic frequency (SHF). The nonlinear coupling coefficient (NCC), which depends on the overlap integral between the interacted two modes in the NP area, is increased by increasing the waveguide asymmetry [94]. Here, the PMC is fulfilled for w = 50 nm, h = 370 nm, where the effective refractive indices of the interacted two modes are n_{FF} = 2.4645+0.0080i and n_{SH} = 2.4642+0.0073i, respectively.

Then, we estimate the tolerable pump power in this PSW by taking into account the damage threshold for the NP layer. In Ref. [155], the experimental average input power in the considered plasmonic slot nanocavity filled with NP was 34 mW, indicating a peak intensity around 2.4×10^8 W/cm^2. Setting this intensity as an acceptable value, the tolerable incident power for our PSW is around 44.4 mW for a 50 nm × 370 nm waveguide cross-section size. We thus considered a maximum pump power of 40 mW.

The ECSHG process is analyzed by using the nonlinear coupled equations. When ω_{FF}, the FF, is converted into the SHF $\omega_{SH} = 2\omega_{FF}$ and an extra electric field of $\vec{E}_c = V_c / we_x$ (V_c is the applied voltage, e_x is the unit vector in x direction) is applied, the nonlinear polarizations are:

$$\vec{P}_{FF}^{NL} = \varepsilon_0 \chi^{(2)} : \left[\vec{E}_{SH} \vec{E}_{FF}^{*} + 2\vec{E}_{FF} \vec{E}_c \right] + 3\varepsilon_0 \chi^{(3)} \vdots \vec{E}_{SH} \vec{E}_{FF}^{*} \vec{E}_c$$
$$\vec{P}_{SH}^{NL} = \varepsilon_0 \chi^{(2)} : \left[\frac{1}{2} \vec{E}_{FF} \vec{E}_{FF} + 2\vec{E}_{SH} \vec{E}_c \right] + \frac{3}{2} \varepsilon_0 \chi^{(3)} \vdots \vec{E}_{FF} \vec{E}_{FF} \vec{E}_c \quad (3.4)$$

Here, $\vec{E}_{FF}$ and $\vec{E}_{SH}$ are the electric field for 0-th mode at FF and 1-st mode at SHF, respectively, and can be expressed by $\vec{E}_{FF,SH} = A_{FF,SH} \vec{E}_{FF,SH}(x, y) \exp(i\beta_{FF,SH} z)$, where $A_{\mathrm{FF,SH}}$ are the slowly varied complex mode amplitudes, $\vec{E}_{FF,SH}(\mathrm{x, y})$ are the normalized mode profiles and $\beta_{\mathrm{FF,SH}}$ are the phase propagation constants. The first to third terms on the right side of Eq. (3.4) stand for the CSHG, $\chi^{(2)}$-induced EO modulation and EFISHG effects, respectively. Note that we have neglected the third-order nonlinear processes of self-phase modulation and cross-phase modulation due to their weak impacts in this study. The nonlinear coupled equations for the considered ECSHG are:

$$\frac{\partial A_{FF}}{\partial z} = -\frac{\alpha_{FF}}{2} A_{FF} + i \frac{\omega_{FF}}{4} \left[\kappa_{11} A_{FF}^{*} A_{SH} + 2\kappa_{12} A_{FF} \right] \exp(i\Delta\beta z)$$
$$\frac{\partial A_{SH}}{\partial z} = -\frac{\alpha_{SH}}{2} A_{SH} + i \frac{\omega_{FF}}{4} \left[\kappa_{21} A_{FF} A_{FF} + 4\kappa_{22} A_{SH} \right] \exp(-i\Delta\beta z) \quad (3.5)$$

$\alpha_{\mathrm{FF,SH}}$ are the attenuation coefficients, $\Delta\beta = \beta_{\mathrm{SH}} - 2\beta_{\mathrm{FF}}$ is the phase mismatch, κ_{ii} are the NCC defined by [59, 94]:

$$\kappa_{11} = \varepsilon_0 \iint \left\{ \begin{array}{l} \chi^{(2)} : \vec{E}_{SH}(x, y) \vec{E}_{FF}^{*}(x, y) \cdot \vec{E}_{FF}'(x, y) + \\ 3\chi^{(3)} \vdots \vec{E}_{SH}(x, y) \vec{E}_{FF}^{*}(x, y) \vec{E}_c \cdot \vec{E}_{FF}'(x, y) \end{array} \right\} dxdy$$
$$\kappa_{21} = \varepsilon_0 \iint \left\{ \begin{array}{l} \chi^{(2)} : \vec{E}_{FF}(x, y) \vec{E}_{FF}(x, y) \cdot \vec{E}_{SH}'(x, y) + \\ 3\chi^{(3)} \vdots \vec{E}_{FF}(x, y) \vec{E}_{FF}(x, y) \vec{E}_c \cdot \vec{E}_{SH}'(x, y) \end{array} \right\} dxdy \quad (3.6)$$
$$\kappa_{12} = \varepsilon_0 \iint \left\{ \chi^{(2)} : \vec{E}_{FF}(x, y) \vec{E}_c \bullet \vec{E}_{FF}'(x, y) \right\} dxdy$$
$$\kappa_{22} = \varepsilon_0 \iint \left\{ \chi^{(2)} : \vec{E}_{SH}(x, y) \vec{E}_c \bullet \vec{E}_{SH}'(x, y) \right\} dxdy$$

If we just take the *x*-component of the modes and the nonlinear susceptibility into account, which is reasonable in this PSW, the generated power of SHF is [155]:

$$P_{SH} = \left| A_{SH} \right|^2 \propto [\chi_{111}^{(2)} + 3\chi_{1111}^{(3)} E_c]^2 = [\chi_{111}^{(2)}]^2 + 6\chi_{111}^{(2)} \chi_{1111}^{(3)} E_c + 9[\chi_{1111}^{(3)}]^2 E_c^2 \quad (3.7)$$

The first term does not include E_c, which is the CSHG part. The last two terms represent the EFISHG contribution. If the NP is centro-symmetric, only the third term then exists.

3.2.3 Effectively controlled SHG by voltage

For the centro-symmetric polymer case, only the EFISHG effect is induced, and the NCC have been calculated to be: $\kappa_{11}^{*} = \kappa_{21} = 6.22 \times V_c$ psm^{-1}W$^{-1/2}$. Fig. 3.10(a) shows the power variations along the propagation for a FF of 1550 nm with a control voltage of 10 V and a pump power of 40 mW. For the pump of FF, the power decreases monotonously due to the conversion and intrinsic loss. With respect to the SH, the power increases until a peak position where the nonlinear conversion has equivalent contribution with the loss. After this peak position, the power starts to decrease. Here, the power of SH reaches its peak of 20 μW at a propagation length of 16 μm. Fig. 3.10(b) shows the electrically controlled performance of this ECSHG mechanism. The length of the waveguide is set to 16 μm. As expected, the output power of SH is modulated by the control voltage in a quadratic form. For V_c = 20 V, the generated SH is 80 μW. This result shows a promising approach to excite equivalent second-order nonlinearity in materials without $\chi^{(2)}$.

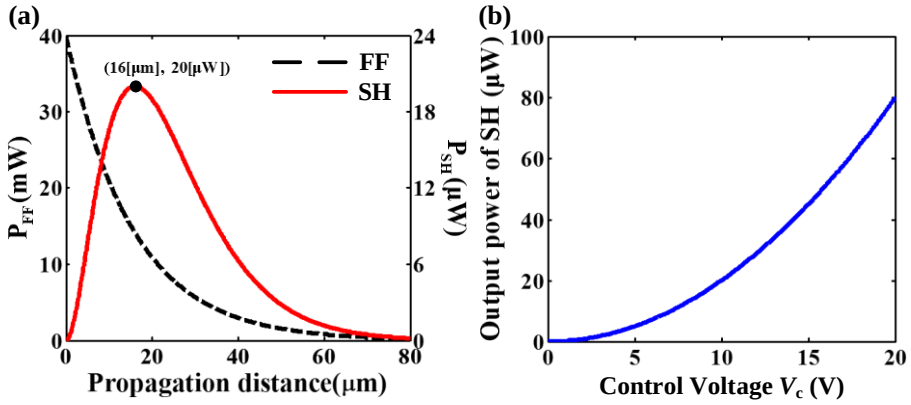

Fig. 3.10 (a) Power variations of FF and SH along propagation for V_c=10 V when the polymer is centro-symmetric. (b) the generated power of SH as a function of the control voltage by setting the length of the waveguide to 16 μm.

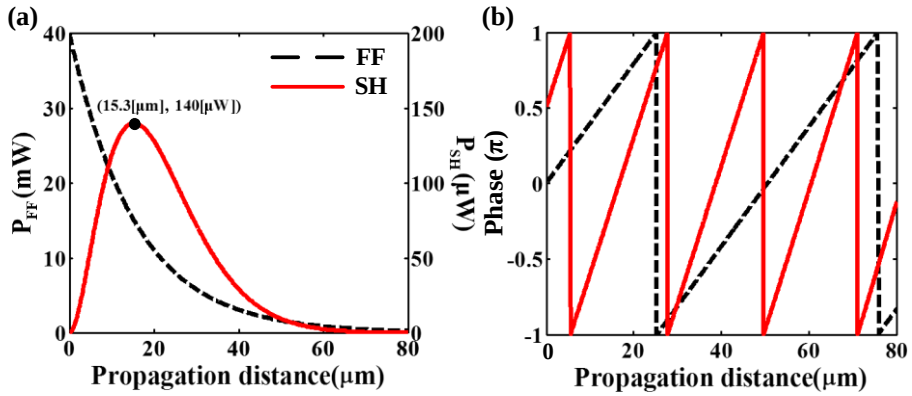

Fig. 3.11 (a) Power and (b) phase variations of FF and SH along propagation for V_c=10 V when we take both $\chi^{(2)}$ and $\chi^{(3)}$ into account.

Apart from the $\chi^{(3)}$, some NP also have $\chi^{(2)}$ properties [155]. In order to give a theoretical insight of this, next we analyze the ECSHG in the PSW with both $\chi^{(3)}$ and $\chi^{(2)}$. The value of $\chi^{(2)}$ is chosen to a typical value of $\chi^{(2)}$ = 230 pm/V in a NP. In this case, the obtained NCC are: $\kappa_{11}^{*} = \kappa_{21} = 104 + 6.2 \times V_c$ psm^{-1}W$^{-1/2}$, κ_{12} = 20.46 $\times V_c$ psm^{-1}W$^{-1/2}$ and κ_{22} =25.78 $\times V_c$ psm^{-1}W$^{-1/2}$. Now the nonlinear process includes all the three terms in Eq. (3.7). Similarly, we plot the obtained SHG result for V_c= 10 V in Fig. 3.11. The peak distance is similar to the previous one, i.e. around 15.3 μm. However, the generated peak power of SH is enlarged to 140 μW. The added part comes from the first two terms in Eq. (3.7). In Fig. 3.11(b), the phases of two signals vary linearly along the propagation due to the $\chi^{(2)}$-induced electro-optical effect.

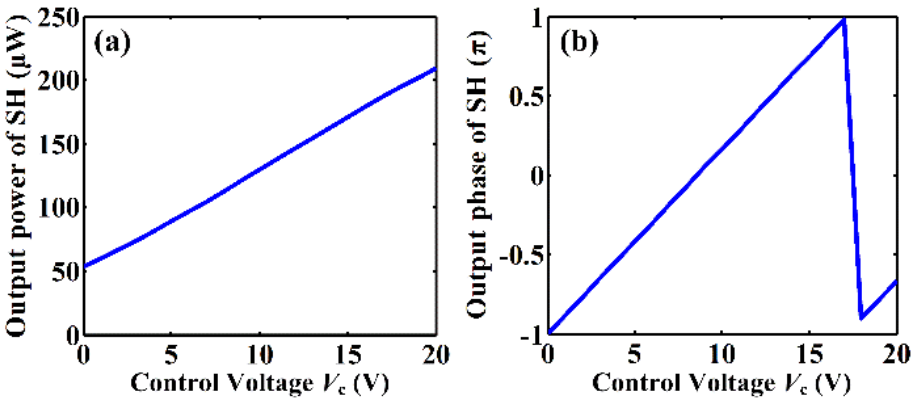

Fig. 3.12 (a) The generated power and (b) output phase of SH for noncentro-symmetric case as a function of the control voltage by setting the length of the waveguide to 13 μm.

As shown in Fig. 3.12(a), the output power of SH is not any more quadratically dependent on the control voltage. As the third term is negligible when compared to the second one in Eq. (3.7), the output power of SH is now almost linearly modulated by the control voltage. Another interesting part of this result is that the output phase of the SH can also be linearly modulated by the voltage in the range of $0 < V_c < 17$ V, as shown in Fig. 3.12(b). Note that the initial phase of FF is set to $\pi/4$ in order to locate the output phase of SH at $-\pi$ for $V_c = 0$. This means that both the intensity and phase of the generated SH can be almost linearly modulated by the voltage. This novel property makes this mechanism promising for electric-controlled nonlinear applications. For example, if we apply an AC voltage (still with a negligible frequency if compared to the optical one) instead of a DC one to control the nonlinear SHG process, we may provide a new mechanism for an electro-optical modulator to realize the generation of some optical signals with advanced modulation formats, i.e. both the intensity and phase of the carrier wave carry the information. In addition, it is worth noting that this is a direct intensity modulation instead of translating the phase modulation into an intensity one by using a conventional Mach-Zehnder scheme, which further simplifies the design and complexity of the modulator.

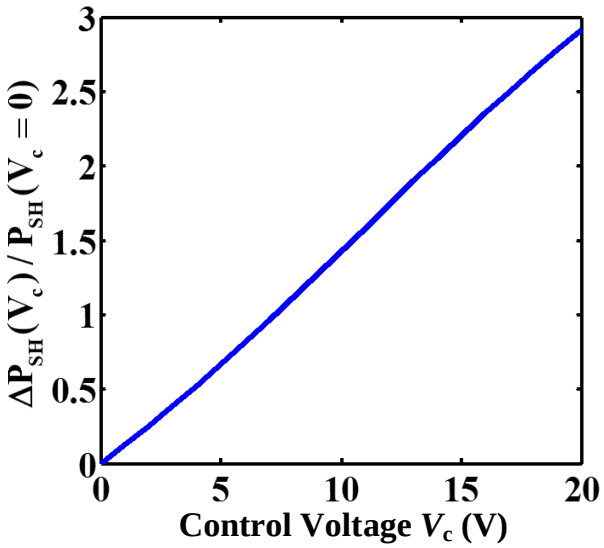

Fig. 3.13 The normalized change of the output power of SH as a function of the externally applied control voltage V_c.

The generated SH at $V_c = 0$ is the CSHG contribution. Setting this power as a reference level, we plot in Fig. 3.13 the normalized change of the SH power as a function of the control voltage. One can see that a nonlinear modulation magnitude of 292% at a bias voltage of 20 V is predicted, while in [155] the corresponding value was about 140%. The resulted efficient SHG and high modulation magnitude are due to the large field enhancement and DC-like field in the slot, large NCC owing to the waveguide vertical asymmetry and the high nonlinear susceptibility of the NP. We also note that further improvement of the SHG performance is possible in terms of the used NP. Here, we have used a very commonly used NP as the active material and taken typical values for the nonlinear susceptibilities. In terms of $\chi^{(2)}$ and $\chi^{(3)}$ properties, other better options can be envisaged. For example, the doped, crosslinked organic polymer mentioned in [35] has a $\chi^{(2)} = 619$ pm/V, and the Poly(3-Hexy1Thiophene) used in [175] has a $\chi^{(3)} = 2.6\times10^{-19}$ m^2/V^2.

3.2.4 Discussion and conclusion

In the envisaged modulation scheme, the proposed configuration has to be investigated in terms of electrical bandwidth, driving voltage, and optical extinction ratio. As the nonlinear processes are instantaneous and none of the speed limiting factors in silicon modulators plays a role in this PSW [42], ultrahigh speed is expected. The capacitance of the device can be estimated by $C = \varepsilon_0\varepsilon_r hL/w = 2.76$ fF, where $\varepsilon_r = 3.24$ is the relative permittivity of the slot NP. w, h and $L = 13$ μm are the width, thickness and length of the waveguide, respectively. If we consider a classical load resistance of $R = 50$ Ω, the maximum cut-off modulation frequency is $f_0 = 1/2\pi RC = 1.15$ THz. Considering other capacitances coming from substrate and cladding, the realistic bandwidth would be smaller. In spite of this, a large bandwidth is still prospective due to the compact footprint and the ultrafast response of the plasmonic structure. Inversely, this mechanism can be applied to detect ultrafast electric signals. For the driving voltage, it is shown in Fig. 3.12 that the proposed approach supports linear intensity modulation

property over a voltage range from 0 V to 20 V, and it is possible to realize a nonlinear phase shift of 2π by altering the voltage from 0 V to 17 V. With respect to the extinction ratio, the average intensity and phase modulation magnitudes are predicted to be 8 μW/V and 0.12 π/V in Fig. 3.12, respectively.

In conclusion, we propose a theoretical insight to the electrically controlled SHG in a silicon compatible hybrid plasmonic slot waveguide with nonlinear polymers infiltrating the slot and a control voltage applied for RF modulation. By considering the NP to be centro-symmetric or noncentro-symmetric, we carry out the dependence of the SHG process on the applied voltage. As a result, efficient SHG and electrically-induced modulation are proposed. Quantitatively, for the noncentro-symmetric NP case, the average intensity and phase modulation magnitudes are predicted to be 8 μW/V and 0.12 π/V, respectively, within a wide range of voltages. The proposed configuration allows inducing low-power equivalent second-order nonlinear processes in centro-symmetric materials, probing ultrafast electrical signals, and realizing electro-optical modulators with dramatically ultrahigh speed.

3.3 Broadband high-speed optical detection based on the optical rectification effect

3.3.1 Introduction

Optical rectification (OR) is a nonlinear process in which a second-order optical nonlinearity converts an optical field into a direct current (DC) or a radio frequency (RF) voltage. It can be seen as the reverse process of the electro-optic (EO) effect [52, 176]. Reported applications of OR include the generation of terahertz radiations or high-frequency electrical pulses [177-182] and high-speed detection of optical radiations [183-186]. The capability of enabling applications with such a high-speed property is attributed to the nearly instantaneous response of second order nonlinearity. For example, high-frequency electrical pulses up to terahertz scale generated by the OR

effect in poled polymers [178], $LiTaO_3$ crystals [179] and bulk GaAs [180] have been reported before. Moreover, OR-based photodetectors (ORPD) have advantages over the traditional semiconductor photodetectors (SPD). Firstly, ORPD can support broadband flat response in the optical domain and can operate at ultra-high speed (>> 100 GHz) in the electrical domain [187], while the frequency response of SPD is limited by electron and hole transit times. Actually, the OR efficiency grows as the speed increases. Secondly, no external DC bias is needed in the detection, though the application of a DC bias tends to increase the responsivity, as shown hereafter. Thirdly, as the OR process only converts a fraction of the optical power into an electrical detected signal, the optical output can be reused for other applications. Mikheev et al. experimentally demonstrated an ORPD in nanographite films with a voltage sensitivity of 5×10^{-7} V/W at hundreds MHz speed [185]. Later, Zhang et al. reported the detection of microwave signals by OR in an integrated AlGaAs waveguide with operation speed to 20 GHz [186]. These schemes were either realized in a free-space configuration or in long distance scales, and most of all were not compatible with silicon photonics which is believed to be the most convenient platform for future integrated optical chips [2].

Based on a silicon photonics approach, T. Baehr-Jones et al. experimentally demonstrated an ORPD in a slot-waveguide-based ring resonator with EO polymers filling the slot, where a current sensitivity of 88 nA/W was observed for a speed of 1 MHz [184]. Unfortunately, this device could not be measured at higher speeds due to substantial output impedance. Recently, the same authors theoretically studied the OR in a silicon slot waveguide instead of considering a ring configuration, in which a much faster response up to 400 GHz was predicted. By using an equivalent circuit model in the analysis, a voltage responsivity of 0.45 V/W was envisaged [187]. However, the device length was of 1 mm, i.e. too long for a possible compact on-chip integration. To overcome this obstacle, plasmonic structures seem to be competitive candidates [154], especially for nonlinear applications [20]. For example, Ward et al. measured the OR in a sub-wavelength plasmonic nanogap but in a free-space configuration [188]. With

respect to using integrated silicon plasmonic waveguides, efficient second order nonlinear processes such as EO modulations [42, 98] and frequency conversions [94, 113, 114, 156] within short length have been also widely proposed theoretically or demonstrated experimentally due to the large field enhancement and overlap between the interacting frequencies.

In this context, a PSW counterpart of the ORPD proposed in Ref. [187] is investigated in the present manuscript, bringing several advantages:

i) the reduction of the device size and thus the ease of group velocity matching between optical frequency (OF) and RF signals due to the short length;

ii) the simplification of the electrode design because of the fact that in a PSW the metallic slabs which constitute the waveguide also serve as the electrodes directly;

iii) the improvement of the OR efficiency within short lengths (< 23 μm) owing to an increased confinement and overlap between OF and RF modes.

In addition, instead of using an equivalent circuit model where the assumption of uniform OF and RF mode profiles in the slot area was employed, a more general model directly derived from the Maxwell's equations is presented here to calculate the OR voltage. Meanwhile, our model is still able to give similar results as those in Ref. [187] under the same assumption. Specifically, by making use of the optimized PSW structure with a compact footprint of 50nm×90nm×22.4μm, an OR voltage responsivity above 1 V/W and an OR current responsivity about 0.42 mA/W are predicted at the RF of 400 GHz. The corresponding normalized OR efficiency is up to 2.25×10^{-4} W^{-1}. Then the responsivity of the ORPD can be further improved by introducing the electrically induced OR contribution. Moreover, the proposed ORPD supports such an efficient performance over a wide range of light wavelength from 1.25 μm to 1.7 μm, containing all the classical communication bands. The electrical bandwidth of the ORPD is estimated to more than 800 GHz.

3.3.2 Waveguide structure and nonlinear modeling approach

The proposed PSW is shown in Fig. 3.14. It consists of two metallic slabs on a silicon oxide substrate and separated by a narrow gap filled with an EO polymer. The two metallic slabs also serve as the electrodes in the OR process. Through the OR process, an electrical signal is generated between the two electrodes when an intensity modulated optical signal is injected into the PSW. The length of the PSW is *l*. The bottom inset shows the cross-section of the PSW, in which the width and height of the slot are defined as *w* and *h*, respectively. The EO polymer is considered to be the doped,

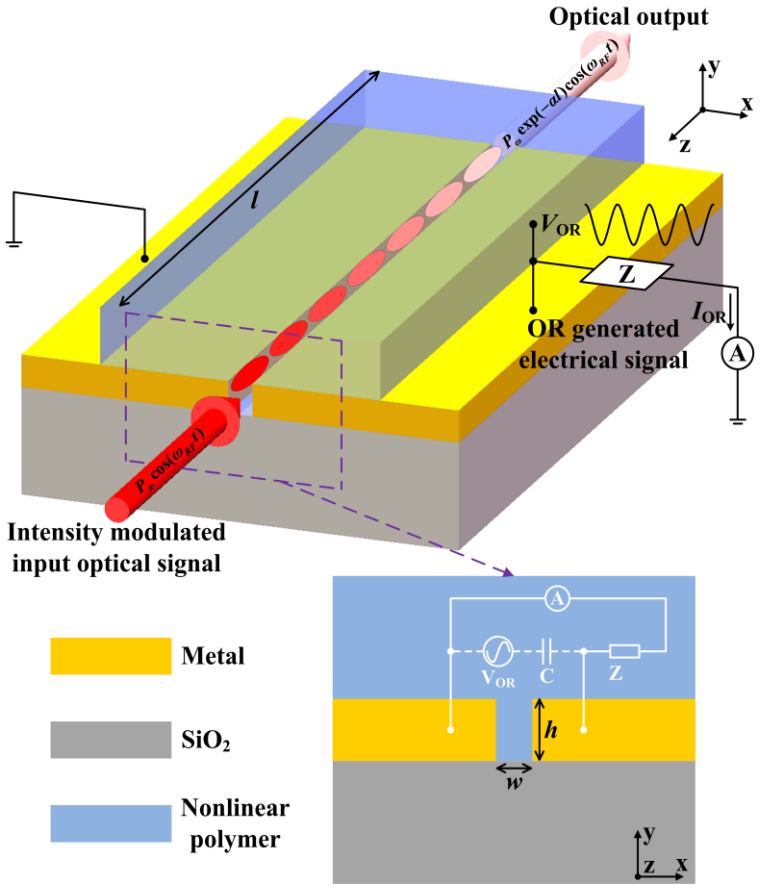

Fig. 3.14 Schematic of the PSW for investigating the OR effect. The bottom inset shows the cross-section of the PSW and the equivalent electrical circuit at RF. As given in the results section, this PSW with size of w = 50 nm, h = 90 nm and l = 22.4 μm supports an OR voltage responsivity above 1 V/W and an OR current responsivity about 0.42 mA/W at the RF of 400 GHz. The corresponding normalized OR efficiency is 2.25×10^{-4} W^{-1}.

crosslinked organic polymer with a refractive index of n_p = 1.643 and an EO coefficient of $\chi^{(2)}_{111}$ = 619.4 pm/V (r_{33} = 170 pm/V) at the wavelength of 1550nm [132]. The metal is considered to be silver in forthcoming calculations. In the meantime, results obtained for gold are also given for comparison. It will be shown hereafter that the two metals, which have been chosen due to their better plasmonic properties in the optical domain and higher conductivity in the electrical domain with respect to other ones, present similar voltage responsivities while silver supports larger OR currents and correspondingly larger OR efficiencies. The bottom inset also shows the equivalent circuit at RF for the calculation of the OR current. With respect to the OR mechanism, the PSW is equivalent to a voltage (OR-induced) source V_{OR} and a C capacitance. Z is the external load resistance. The resistance between the electrodes and the slot has been neglected here due to the high conductivity of the considered metal.

To begin, let us set the electric field at the optical frequency (OF) to be $\tilde{\boldsymbol{E}}(t) = \boldsymbol{E}_\omega e^{-i\omega t} + c.c.$ with ω being the angular frequency of the OF. Then, by assuming that the OF signal is an intensity modulated signal with a modulation frequency of ω_{RF}, the nonlinear polarization resulting from the OR effect for the RF signal is:

$$\boldsymbol{P}_{RF}^{NL} = 2\varepsilon_0 \chi^{(2)} : \boldsymbol{E}_\omega \boldsymbol{E}_\omega^* \cos(\omega_{RF} t) \tag{3.8}$$

Now the RF fields $\{\boldsymbol{E}_{RF}, \boldsymbol{H}_{RF}\}$ fulfill the Maxwell equations with nonlinear polarization:

$$\begin{aligned} \nabla \times \boldsymbol{E}_{RF} &= -\mu \frac{\partial \boldsymbol{H}_{RF}}{\partial t} \\ \nabla \times \boldsymbol{H}_{RF} &= \varepsilon_0 \varepsilon_r \frac{\partial \boldsymbol{E}_{RF}}{\partial t} + \frac{\partial \boldsymbol{P}_{RF}^{NL}}{\partial t} \end{aligned} \tag{3.9}$$

where ε_r is the relative permittivity at RF. We can then obtain:

$$\nabla \times \nabla \times \boldsymbol{E}_{RF} = \mu \varepsilon_0 \varepsilon_r \omega_{RF}^2 \boldsymbol{E}_{RF} + \mu \omega_{RF}^2 \boldsymbol{P}_{RF}^{NL} \tag{3.10}$$

When the size of the waveguide is much smaller than the wavelength of the RF

signal, i.e. (w, h, l) << λ_{RF}, which is satisfied in the proposed PSW, the left part of Eq. (3.10) is approximately equal to 0. This well-satisfied approximation then leads to:

$$\boldsymbol{E}_{RF} = -\frac{\boldsymbol{P}_{RF}^{NL}}{\varepsilon_0 \varepsilon_r} = -\frac{2\chi^{(2)} : \boldsymbol{E}_{\omega}\boldsymbol{E}_{\omega}^{*}}{\varepsilon_r}\cos(\omega_{RF}t) \tag{3.11}$$

This electric field distribution induced from the nonlinear polarization can be expanded over the guided modes, radiation modes, and the evanescent modes at the RF of ω_{RF} [116]. The most interesting part is the conversion efficiency to the fundamental guided mode due to the largest overlap integral between this mode and the nonlinear RF fields, i.e. $\boldsymbol{E}_{RF}$. Defining the fundamental guided mode distribution at ω_{RF} as $\{\boldsymbol{E}_0, \boldsymbol{H}_0\}$ corresponding to 1 V voltage between two electrodes, the generated RF voltage value from the nonlinear OR effect is:

$$V_0 = \frac{\iint_{gap} e_z \cdot \{\boldsymbol{E}_{RF} \times \boldsymbol{H}_0\} dxdy}{\iint e_z \cdot \{\boldsymbol{E}_0 \times \boldsymbol{H}_0\} dxdy} = -\frac{2\cos(\omega_{RF}t)}{\varepsilon_r} \frac{\iint_{gap} e_z \cdot \{\chi^{(2)} : \boldsymbol{E}_{\omega}\boldsymbol{E}_{\omega}^{*} \times \boldsymbol{H}_0\} dxdy}{\iint e_z \cdot \{\boldsymbol{E}_0 \times \boldsymbol{H}_0\} dxdy} \tag{3.12}$$

For simplicity, we will just consider the x components of the field and nonlinear susceptibility, which is a reasonable assumption in PSW [94]. Further, if we consider the RF field to be uniform in the cross-section of the gap, i.e. $\boldsymbol{E}_0 = E_{0,x} \cdot e_x = 1[\mathrm{V}]/w$ and $\boldsymbol{H}_0 = H_{0,y} \cdot e_y$, the obtained voltage goes to:

$$V = -\frac{2\chi_{xxx}^{(2)}\cos(\omega_{RF}t)}{\varepsilon_r h} \iint_{gap} |E_{\omega,x}|^2 \, dxdy \tag{3.13}$$

Interestingly, if the optical mode is considered to be uniform in the slot as well, then the generated voltage turns into the same value as the Eq. (12) of Ref. [187], where a lumped-element equivalent circuit model was employed. In addition, it should be noted that even though the length of the PSW is negligible when compared with the RF wavelength λ_{RF}, it is usually larger than the optical wavelength λ_{ω}. As a result, it is needed to take the loss of the optical mode into account. The intensity of the optical

mode is attenuated along the propagation in the form of $I_\omega(z) \propto \left|E_{\omega,x}\right|^2 \exp(-\alpha z)$, where α is the attenuation constant of the optical mode. Here, we apply the average value of the intensity along the propagation to calculate the OR-obtained voltage:

$$V_{OR} = V\frac{\int_0^l \exp(-\alpha z)dz}{l} = -\frac{2\chi_{xxx}^{(2)}[1-\exp(-\alpha l)]\cos(\omega_{RF}t)}{\varepsilon_r \alpha hl}\iint_{gap}|E_{\omega,x}|^2\,dxdy \qquad (3.14)$$

The generated current is then:

$$I_{OR} = \left[\frac{1}{i\omega_{RF}C} + Z\right]^{-1} V_{OR} = -\frac{2\chi_{xxx}^{(2)}\omega_{RF}\varepsilon_0[1-\exp(-\alpha l)]\cos(\omega_{RF}t)}{\omega_{RF}\varepsilon_0\varepsilon_r\alpha hlZ - i\alpha w}\iint_{gap}|E_{\omega,x}|^2\,dxdy \qquad (3.15)$$

where $C = \varepsilon_0\varepsilon_r hl/w$ is the capacitance and Z is the external load resistance. As a result, the voltage responsivity V_R, current responsivity I_R and the normalized efficiency of the OR process η in the PSW are:

$$\begin{aligned}
V_R &= \frac{|V_{OR}|}{P_\omega} = \frac{2\chi_{xxx}^{(2)}[1-\exp(-\alpha l)]}{\varepsilon_r\alpha hl}\frac{\iint_{gap}|E_{\omega,x}|^2\,dxdy}{\iint 2e_z\cdot\{\boldsymbol{E}_\omega\times\boldsymbol{H}_\omega\}\,dxdy} \\
I_R &= \frac{|I_{OR}|}{P_\omega} = \frac{2\chi_{xxx}^{(2)}\omega_{RF}\varepsilon_0[1-\exp(-\alpha l)]}{\sqrt{(\omega_{RF}\varepsilon_0\varepsilon_r\alpha hlZ)^2+\alpha^2w^2}}\frac{\iint_{gap}|E_{\omega,x}|^2\,dxdy}{\iint 2e_z\cdot\{\boldsymbol{E}_\omega\times\boldsymbol{H}_\omega\}\,dxdy} \\
\eta &= \frac{|V_{OR}|\cdot|I_{OR}|/2}{P_\omega^2} = \frac{2\omega_{RF}\varepsilon_0\left\{\chi_{xxx}^{(2)}[1-\exp(-\alpha l)]\right\}^2}{\varepsilon_r\alpha hl\sqrt{(\omega_{RF}\varepsilon_0\varepsilon_r\alpha hlZ)^2+\alpha^2w^2}}\left[\frac{\iint_{gap}|E_{\omega,x}|^2\,dxdy}{\iint 2e_z\cdot\{\boldsymbol{E}_\omega\times\boldsymbol{H}_\omega\}\,dxdy}\right]^2
\end{aligned} \qquad (3.16)$$

Here $P_\omega = \iint 2e_z\cdot\{\boldsymbol{E}_\omega\times\boldsymbol{H}_\omega\}dxdy$ is the input power of the optical mode. Noting that the parameter of $\int_{gap}\left|E_{\omega,x}\right|^2 dxdy \Big/ \iint_{gap}\iint 2e_z\cdot\{\boldsymbol{E}_\omega\times\boldsymbol{H}_\omega\}\,dxdy$ is very similar to the interaction factor Γ or the effective index susceptibility γ for the EO effect [36, 144], which makes sense since the OR is considered to be the reversed effect of the EO modulation.

3.3.3 Effective optical rectification in plasmonic slot waveguides

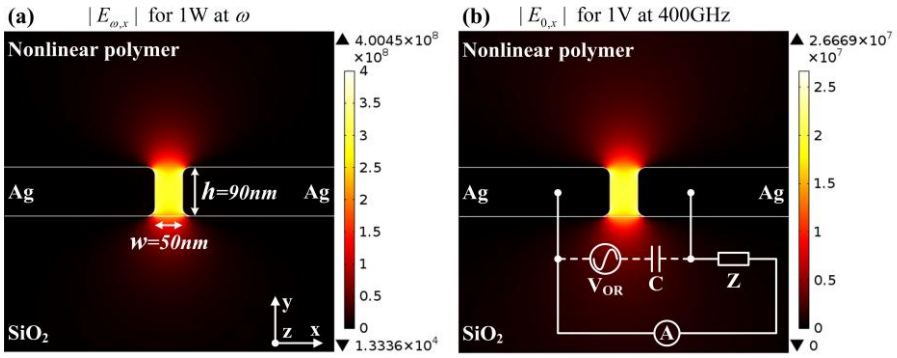

Fig. 3.15 *x*-components of the electric field at (a) optical frequency and (b) RF of 400GHz with *w*=50nm, *h*=90nm. The optical power and the electrical voltage have been normalized to 1W and 1V, respectively.

As a starting point, we carry out the mode distributions of the PSW at the OF and RF in the considered structure of Fig. 3.14. The related field profiles obtained with the finite element based commercial software Comsol Multiphysics are shown in Fig. 3.15(a) and (b), respectively. In Fig. 3.15(a) the optical power has been normalized to 1 W, and in Fig. 3.15(b) the given mode distribution corresponds to 1 V of potential difference between the two electrodes for a RF of 400 GHz. The dimensions of w = 50 nm and h = 90 nm, respectively, have been chosen for the purpose of large OR efficiency after an optimization procedure, as shown soon afterwards. As can be seen, both the OF and RF fields are tightly confined in the slot area. Specifically, the electric field at the OF is up to the magnitude of ~10^8 V/m for 1 W, and electric field at the RF arrives to magnitude of ~10^7 V/m for 1 V of drop voltage between the two electrodes. This matter of fact is likely to facilitate the high efficiency of nonlinear processes involving the filling of the slot.

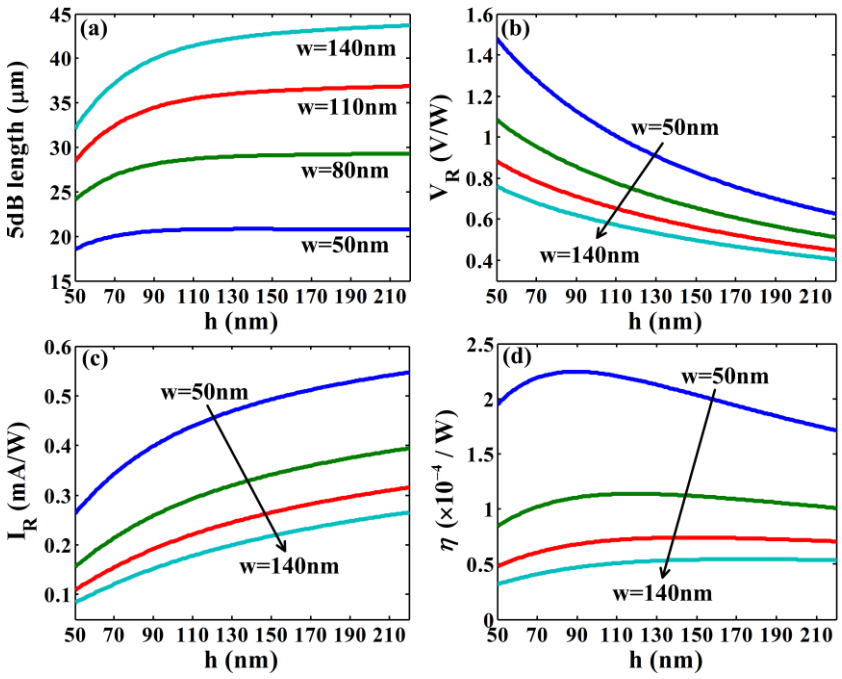

Fig. 3.16 (a) 5dB length (where the transmission of the optical mode is -5 dB) of the PSW for different cross-sectional sizes. (b), (c) and (d) are the voltage responsivity, current responsivity and the normalized efficiency of the OR process in the PSW with 5dB length as a function of the height for different values of the width, respectively.

Now, based on the calculated modes and Eq. (3.16), the voltage responsivity V_R, the current responsivity I_R, and the normalized OR efficiency η can be obtained. Fig. 3.16 shows the related results as a function of the slot height for different slot widths. In Fig. 3.16(a) the '5dB length' is defined as the length where the transmittance of the optical mode is -5 dB due to the absorption loss of the metal. The OR results in Fig. 3.16(b)-(d) are obtained in a PSW with this 5dB length. It is shown that the PSW has larger losses for smaller widths, while the OR shows better performance. This trend can be attributed to the better field confinement at both frequencies for decreasing widths. With respect to the dependence on the waveguide height, the OR voltage decreases and the current increases when the height increases. This phenomenon can be explained as follows. As shown in Eq. (3.14), the h parameter is in the denominator. Even though the integral term increases for larger heights, the correlation coefficient is smaller than one. In the same time, the impedance of the capacitor goes down as the height goes up,

which leads to larger currents. As an interesting result, from Fig. 3.16(d), we can see that there exists an optimal height for a certain width for the OR efficiency. The obtained optimal heights for different widths are given in Table 3.1.

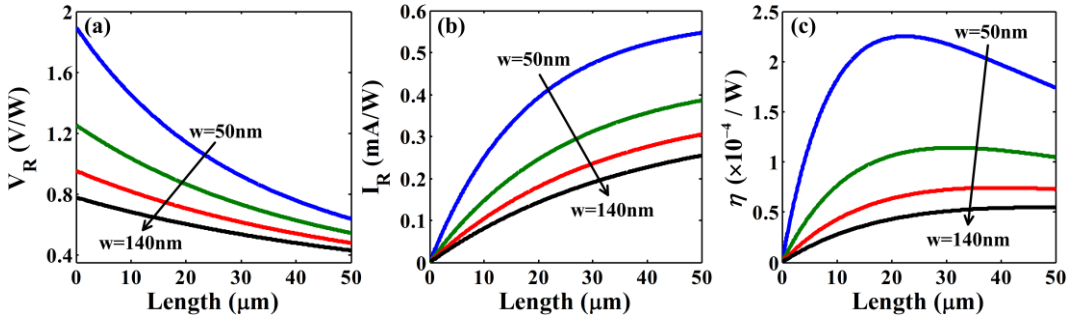

Fig. 3.17 The voltage responsivity (a), current responsivity (b) and the normalized efficiency (c) of the OR process in the PSW as a function of the PSW waveguide length. Here, the height has been chosen to the optimal value for a certain width coming from the approach giving rise to the results of Fig. 3.16.

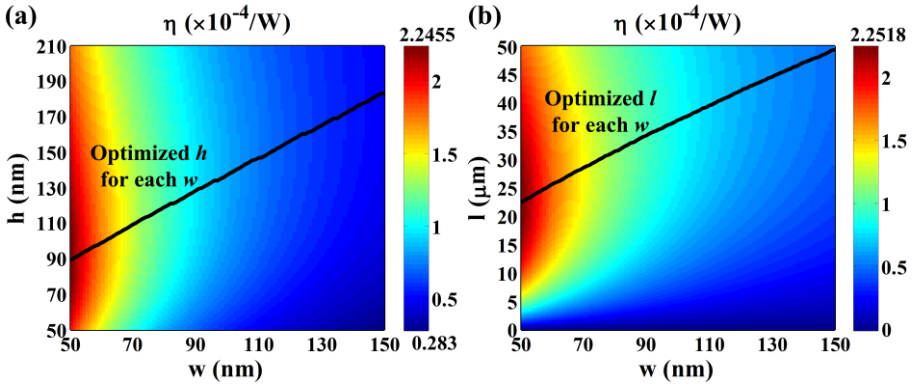

Fig. 3.18 (a) Normalized OR efficiency as functions of *w* and *h* with 5dB length. The black line marks out the optimized *h* for each *w*. (b) Normalized OR efficiency as functions of *w* and *l*. The height has been chosen to be the optimized value in (a). The black line marks out the optimized *l* for each *w*.

Next, we set the height to the optimized value and sweep the length of the PSW. The results are shown in Fig. 3.17. When the length increases, the loss of the optical mode increases, thus reducing the average power along the propagation distance and thus the OR voltage. However, similarly as before, the OR current increases due to the reduction of the capacitor impedance for increasing lengths. As shown in Fig. 3.17(c),

there exists an optimal length as well. As a conclusion, there is an optimized structural dimension for the OR efficiency in the PSW to a certain width. In Fig. 3.18, the black lines mark out the optimized *h* and *l* values. In Fig. 3.18(a) the length has been chosen to be the previously introduced 5dB length, while in Fig. 3.18(b) the height has been chosen to be the optimized value for each *w* obtained in Fig. 3.18(a).

***w* (nm)**	***h* (nm)**	***l* (μm)**	**V_R (V/W)**	**I_R (mA/W)**	**η (10^{-4}/W)**
50	90	22.4	1.0810	0.4166	2.2517
80	119	31.5	0.7140	0.3198	1.1417
110	147	39.6	0.5423	0.2743	0.7438
140	174	47.1	0.4421	0.2473	0.5467
50	90	5.4	1.0984	0.1021	0.5607

Table 3.1. The optimized height and length for different widths and the corresponding voltage responsivity, current responsivity and the optimized normalized efficiency of the OR process. The last row represents the result for the metal of Au.

Table 3.1 lists the optimized sizes and results for a couple of specific widths. As a whole, the OR shows better performance for smaller widths. However, it should be noted that the fabrication of the PSW is difficult and the coupling efficiency between silicon waveguides and PSW becomes low when the width is too narrow. Another issue needs to be accounted is that the poling efficiency of the EO polymer may deteriorate in the ultra-narrow slot. Therefore, we choose a smallest width of 50 nm, as the efficient coupling between the silicon waveguide and PSW with such a gap was demonstrated in a previous paper in an orthogonal junction configuration [189]. The last row in Table 3.1 represents the result for the case of gold. Compared with the silver case, the optimized height is similar and so does the generated voltage, while the optimized length is much shorter due to the larger metallic loss. As a result, the OR current and the efficiency are smaller than that by using silver, which is the reason why we mainly choose silver in this analysis. At last, we note that there still exists rooms for further improvement of the OR efficiency in terms of the used EO polymer. For example, in

Ref. [187] an EO polymer with r_{33} = 300 pm/V was considered.

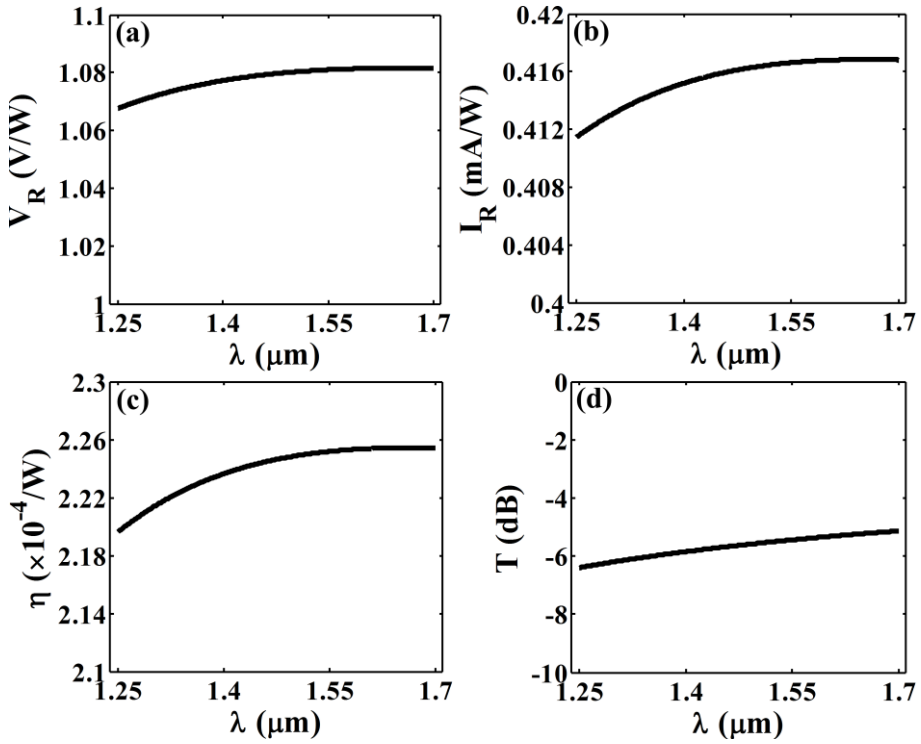

Fig. 3.19 The OR property of the PSW as a function of the optical wavelength for w = 50 nm, h = 90 nm and l = 22.4 μm. (d) is the transmittance of the PSW.

Next, we study the frequency response of this OR mechanism at OF and RF regions. Fig. 3.19 shows the OR property as a function of the optical carrier wavelength for w = 50 nm, h = 90 nm and l = 22.4 μm. As can be seen, the OR in the PSW enables a relatively flat response for a wide wavelength range from 1.25 μm to 1.7 μm, which contains all the classical communication bands. Fig. 3.19(d) is a plot of the optical mode power transmittance through the 22.4 μm long structure, which is around -6 dB in the calculated waveband. Fig. 3.20 shows the OR property as a function of the RF. The OR voltage is not given since it is not relevant to the RF according to Eq. (3.16). We can see that the responsivity of the proposed ORPD is heavily frequency dependent, i.e. it shows a linear dependence on the RF. What should be emphasized here is that a speed limitation still exists in this device. Firstly, the condition of $\lambda_{RF} >> l$ must be satisfied for the validity of Eq. (3.11). If we set this condition to $\lambda_{RF} \geq 10l$ in the PSW, the limiting factor would be $f_1 = c/10ln_{eff}$ = 815 GHz, where n_{eff} is the effective refractive index of

the RF mode. Here we set $n_{eff} = n_p$ by considering the metal as an ideal conductor at RF. Beyond this RF range, a travelling-wave model is needed, such as the nonlinear coupled-wave model in [59]. The second factor lies in the transition time of single optical wave-packet in order to avoid the crosstalk between two adjacent wave-packets. This limitation is $f_3 = c/ln_g = 5.72$ THz, $n_g = 2.34$ being the group index of the OF mode at $\lambda_\omega = 1550$ nm. Note that there is no RC constant resulted bandwidth limitation in this ORPD. On the contrary, as shown in Fig. 3.20, the ORPD shows better performance at higher RF.

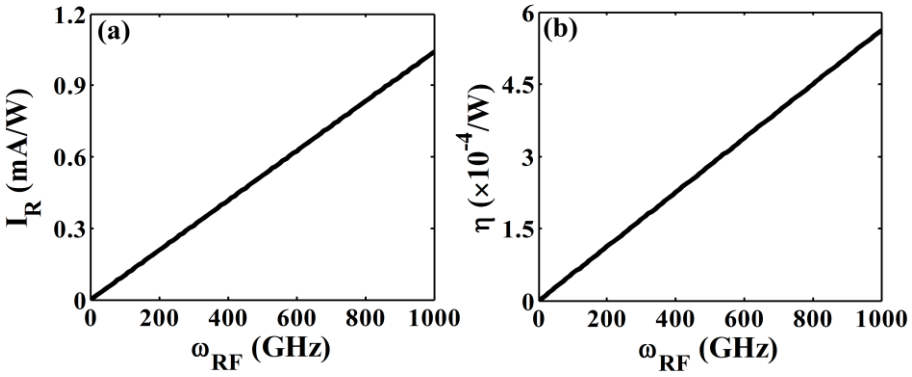

Fig. 3.20 The OR property of the PSW as a function of the radio frequency for $w = 50$ nm, $h = 90$ nm and $l = 22.4$ μm.

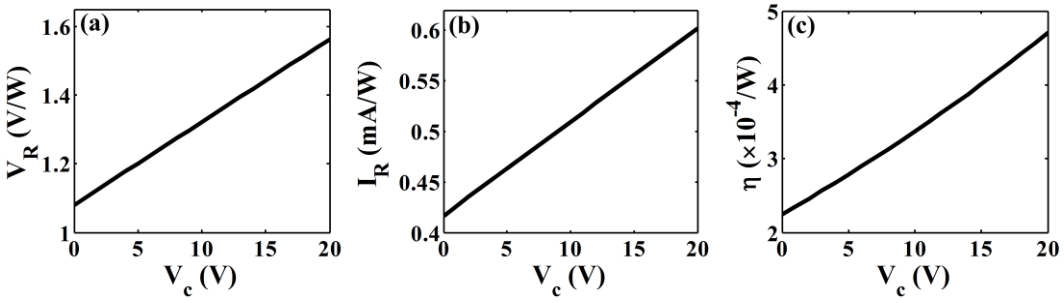

Fig. 3.21 The OR property in the PSW as a function of the control DC voltage for $w = 50$ nm, $h = 90$ nm and $l = 22.4$ μm.

In conclusion, the cut-off frequency is estimated to be around 800 GHz in the present configuration. This high speed is believed to be larger than that in the conventional semiconductor photodetectors by one order of magnitude. This capability of generating ultrahigh speed electrical signals may also derive another potential

application of the proposed structure, which is the generation of THz radiation.

In the same time, the current responsivity of proposed ORPD is small when compared with the one in the semiconductor detectors, which have typical responsivities of 0.5 to 1A/W. Apart from the way to employ EO polymer with larger nonlinear coefficients, we propose here another method to increase the responsivity of the ORPD by analyzing the electrical induced OR when introducing a DC electrical bias between the two metallic electrodes. For this case, an effective second order nonlinear coefficient of $\chi_{111}^{(2)} + 3\chi_{1111}^{(3)} E_c$ is considered when only the *x* components are taken into account [190]. Here $E_c = V_c/w$ with V_c being the external applied DC voltage. When a typical value of $\chi_{1111}^{(3)}$ =2.3×10^{-19} m^2/V^2 is considered [135], the OR property in the PSW is shown in Fig. 3.21. It can be seen that the OR process can be linearly controlled and improved by the external applied voltage. The normalized OR efficiency has been further improved more than two times when V_c = 20 V. Note that the total voltage is $V_c + V_R P_\omega \cos(\omega_{RF} t)$ now. Besides, as a common property of nonlinear effect, a high pump power can lead to high OR efficiency. However, it is worth noting that there is a power limitation which comes from two aspects. Firstly, there is an optical damage threshold for the polymer, beyond this value the polymer will get damaged. Secondly, the loss from the metal will elevate the temperature of device. The temperature cannot exceed the glass transition temperature of the used polymer, or the chromophores of the polymer will reorientate and degrade the second-order nonlinear property of the used polymer. Therefore, the input optical power should be carefully chosen in practical experiments.

3.3.4 Conclusion

Based on an originally proposed and general model, in a PSW with a compact footprint of 50nm×90nm×22.4μm, an effective OR process with a normalized efficiency of 2.2517×10^{-4} W^{-1} is predicted for an intensity-modulated optical signal with speed of

400 GHz. The corresponding voltage and current responsibilities are 1.081 V/W and 0.4166 mA/W, respectively. Then, an original approach is additionally proposed for increasing the responsivity of the ORPD by bringing in the electrical induced OR. Apart from the classical semiconductor photodetectors that are based on the carrier-induced photoconductive or photovoltaic effects, the proposed ORPD scheme takes advantage of the transient nonlinear optical effect. This makes ORPD supports ultra-high speed (> 800 GHz) around one order of magnitude larger than the one in semiconductor PD. Other advantages include compact footprint and no need for external bias. As to our best knowledge, this work is the first investigation of the nonlinear optical rectification effect in an integrated silicon plasmonic waveguide based on standard silicon-on-insulator technologies. Based on this OR scheme, low-power high-speed broadband optical detection and demodulation can be envisaged in silicon chips.

3.4 Chapter summary

In this Chapter, we have investigated three kinds of nonlinear processes in the plasmonic slot waveguides (PSW) with compact dimensions.

(1) We theoretically investigated the possible increase of the SHG efficiency in PSW. The needed phase matching condition is satisfied between the fundamental waveguide mode at the fundamental frequency (FF) and second-order waveguide mode at the second harmonic frequency (SHF) by an appropriate design of the waveguide opto-geometrical parameters. The SHG signal generated in our starting waveguide is three orders of magnitude higher than those previously reported. Then, the SHG performance was further improved by increasing the asymmetry of the structure where nonlinear coupling coefficients as large as 292 $psm^{-1}W^{-1/2}$ are predicted. The device length is shorter than 20 μm and the normalized SHG conversion efficiency comes up to more than 1×10^5 $W^{-1}cm^{-2}$.

(2) We theoretically investigated the possible realization of an active electro-optical

control of the nonlinear SHG mechanism in a PSW. Both the conventional SHG and the electrically induced SHG were taken into account with a moderate pump power of 40 mW at the FF of 1550 nm. The generated SHF power can be modulated by the applied voltage in a quadratic and almost linear form for centro-symmetric and noncentro-symmetric nonlinear polymers integrated in the slot, respectively. Converted power up to 140 μW within a short distance of 16 μm is predicted for a voltage of 10 V. This mechanism may open a new route to realize high-speed advanced modulations or inversely to detect ultrafast electrical signals.

(3) We theoretically investigated the nonlinear optical rectification (OR) process in a PSW. An electrical signal is generated between the two metal slabs when an intensity-modulated optical signal is injected into the PSW. Optimization of the geometrical parameters is performed to obtain the highest OR efficiency. Specifically, a voltage responsivity over 1 V/W and a normalized OR efficiency of 2.25×10^{-4} W^{-1} are predicted in a compact PSW with active size of 50nm×90nm×22.4μm for a modulation speed of 400 GHz. The OR efficiency is further increased when introducing the electrically induced OR contribution. The OR characterizes a relatively flat response for a wide range of optical wavelengths from 1.25 μm to 1.7 μm and supports a RF cut-off frequency up to 800 GHz. This efficient OR process paves a new way for realization of high-speed broadband optical detection and demodulation in silicon chips.

All these analysis and results illustrate the key role of PSW in realizing efficient nonlinear effects within short distance and with low power.

Chapter 4

Enhancement of nonlinear effects using hybrid plasmonic waveguides

As mentioned earlier, hybrid plasmonic waveguides (HPW) support a better compromise between confinement and loss when compared with plasmonic slot waveguides. The tight confinement and local enhancement in the subwavelength low refractive index (RI) spacer layer yet allows to efficiently enhance nonlinear optical effects in short distances. Meanwhile, their relative low propagation losses further facilitate the effectiveness of the nonlinear processes. In addition, the existence of the high RI region offers another degree of freedom to tune the performance of HPW for fulfilling phase matching conditions (PMC). Reported nonlinear applications based on HPW include second harmonic generation (SHG) [91, 109, 140], third harmonic generation [112], optical parameter amplification for compromising the loss of SPP mode [139], EO modulators [98, 99] and high Kerr nonlinearity [111].

These excellent properties have encouraged us to exploit HPW in different configurations, as described hereafter. Specifically, in section 4.1 we theoretically investigate the SHG process from the mid-infrared to the near-infrared band in a HPW based on a nonlinear polymer and then address its further enhancement by applying the HPW into a microring resonator (MRR) configuration in section 4.2. In section 4.3, we similarly study the optical parameter amplification process in a symmetric HPW. Based on the effective phase sensitive amplification process, phase regeneration of the phase shift keying optical signal is finally proposed.

4.1 Enhanced second harmonic generation in hybrid plasmonic waveguides

4.1.1 Introduction

Over the last few decades, silicon photonics has been extensively studied to operate near the telecommunication band in the near-infrared (NIR) wavelength region. Recently, the mid-infrared (MIR) silicon photonics has also attracted considerable attention due to the relatively low intrinsic loss of silicon in this waveband range from typically two to eight microns and to the existence of various application areas [2, 191-195], including sensing, medical diagnostics, thermal imaging and free-space communications [196]. It is thus interesting and significant to bridge these two wavelength bands through nonlinear wavelength conversion. Principles and devices based on nonlinear frequency conversion to bridge the MIR-to-NIR gap have been intensively studied [197-199]. Another motivation for this lies in the challenges related to the detection of MIR waves. The size of detectors is usually bulky or a cryogenic environment is often needed, which limits the development of the integration level and hinders the low-power consumption of MIR systems. A MIR-to-NIR conversion then allows circumventing these drawbacks by detecting the converted waves using mature telecom-band photodetectors [199, 200].

Up to date, MIR to NIR proposed converters in silicon photonics have mostly exploited nonlinear four-wave mixing processes in silicon itself [199, 201]. For example, spectral translation of a signal at 2440 nm to the telecom band at 1620 nm was realized based on four-wave mixing in silicon wires [199]. However, the conversion efficiency may be increased by using nonlinear materials with larger nonlinear susceptibilities or lower-order nonlinear processes with larger efficiencies [52]. A promising way is to integrate organic materials with large $\chi^{(2)}$ into silicon waveguides, which is known as silicon-organic hybrid (SOH) technology [35]. For instance, Alloatti et al. proposed a SOH double slot waveguide enabling for the first

time efficient second-order nonlinear optical mixing in silicon photonics with standard technology [162]. In addition, plasmonic based nonlinear devices open up opportunities for further improving the performances of nonlinear processes and scaling down their sizes [20].

Among the planar plasmonic structures that have been proposed, a well-defined configuration called the hybrid plasmonic waveguide (HPW) was proved to enable subwavelength confinement and long propagation distance in the same time [77, 78]. Based on HPW, passive components and nonlinear devices have been studied. For example, Lu et al. [109] and Pigozzo et al. [140] studied efficient second harmonic generation (SHG) processes in $LiNbO_3$ and AlGaAs-based HPW, respectively. However, the nonlinear HPW they proposed are not compatible with silicon photonics.

4.1.2 Waveguide structure and mode analysis

In this manuscript, we propose a silicon-organic hybrid plasmonic waveguide (SOHPW) easily amenable to fabrication with a nonlinear polymer (NP) in an horizontal slot scheme, as shown in Fig. 4.1. The polymer considered here is the doped, crosslinked organic polymer with a refractive index of n = 1.643 and a nonlinear susceptibility of $\chi_{111}^{(2)}$ = 619 pm/V at the wavelength of 1550 nm [35]. Material dispersion for modeling the refractive index of SiO_2, silicon and Ag are taken from Refs. [47], [46] and [49], respectively. Based on this SOHPW, we investigate the second-order frequency conversion between a mid-IR wave (3100 nm) and the main optical wavelength of the near-IR window, i.e. λ = 1550 nm. Using the mode phase matching (MPM) technique, efficient phase-matched SHG is demonstrated from the fundamental waveguide mode at the fundamental frequency (FF) to the second-order waveguide mode at the second harmonic frequency (SHF).

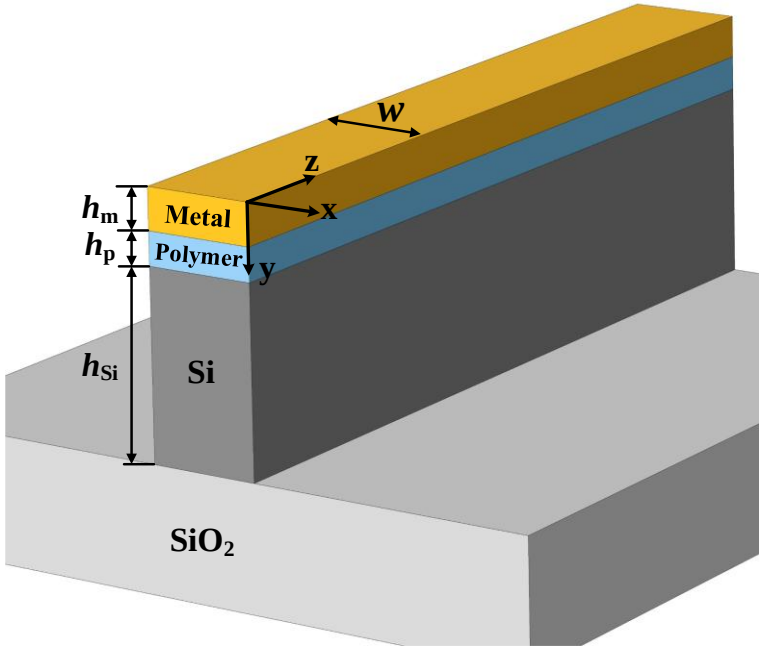

Fig.4.1 Schematic of the nonlinear hybrid plasmonic waveguide: h_{Si} = 480 nm, h_p = 60 nm, h_m = 100 nm.

In the SOHPW, the hybrid modes are the results of the coupling between the SPP mode at the Ag-NP interface and the TM polarized dielectric mode with a high-index silicon as its core. At a given wavelength, the SOHPW supports a plasmonic-like mode with greatly enhanced field in the low-index NP slot for a small-size silicon slab. Conversely, a large-size silicon slab results in a dielectric-like mode with more electromagnetic energy confined into the high-permittivity silicon core and with lower loss [77]. Here, for the FF (λ = 3100 nm), the supported fundamental mode resulting from the coupling between the SPP and the TM_{00} dielectric modes belongs to the plasmonic-like kind. With respect to the SHF with smaller wavelength (λ = 1550 nm), however, the fundamental mode is dielectric-like. In the same time, the second-order mode at SHF resulting from the coupling between SPP mode and TM_{01} dielectric mode is plasmonic-like with a strong confinement in the NP layer. In the next, we thus analyze these three modes and demonstrate that the phase matching condition is possible between the two plasmonic-like modes with correct design of the opto-geometrical parameters.

Using a finite-element-based commercial software (COMSOL), we analyze the modes for different waveguide widths. Fig. 4.2(a), (b) show the mode refractive indices of the 0-th mode at FF (red solid line), the 1-st mode at SH (blue dashed line), and the 0-th mode at SH as a function of w. One sees that the dispersion properties of the two plasmonic-like modes are very similar within a wide range of width. Especially the two cross points at w = 243.3 nm and w = 329.6 nm represent two phase-matching points. Fig. 4.2(c), (d), and (e) give the distributions of the dominant component E_y for the 0-th mode at FF, the 1-st mode at SH, and the 0-th mode at SH, respectively, for w = 329.6 nm. The mode refractive indices (n_{eff}) of the three modes are 1.904005 + 0.002648i, 1.904017 + 0.001571i, and 2.730581 + 1.607207 $\times 10^{-4}$i, respectively. Here the 0-th mode at the SH has lower loss than the one at the FF due to its dielectric-like property.

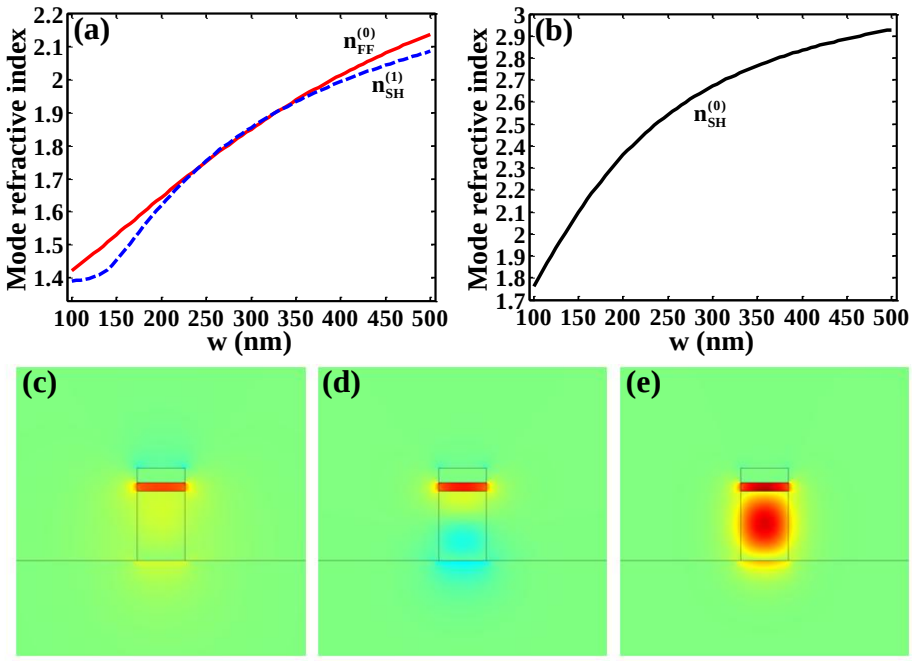

Fig.4.2 (a), (b) Mode refractive indices as a function of the width. E_y distributions of (c) 0-th mode at FF; (d) 1-st mode at SH; and (e) 0-th mode at SH at the phase-matching point of w = 329.6 nm.

In order to more clearly highlight the mode profiles, we plot in Fig. 4.3 the E_y distributions along a y-cutline at x = -0.5w. For the two modes under interest here, i.e.

the 0-th mode at FF and the 1-st mode at SH, the fields are greatly enhanced in the NP slot and there is a change of sign in the silicon part for the 1-st mode at SHF. With respect to the 0-th mode at SHF, the field is mainly in the silicon part and the related loss level of this mode is lower.

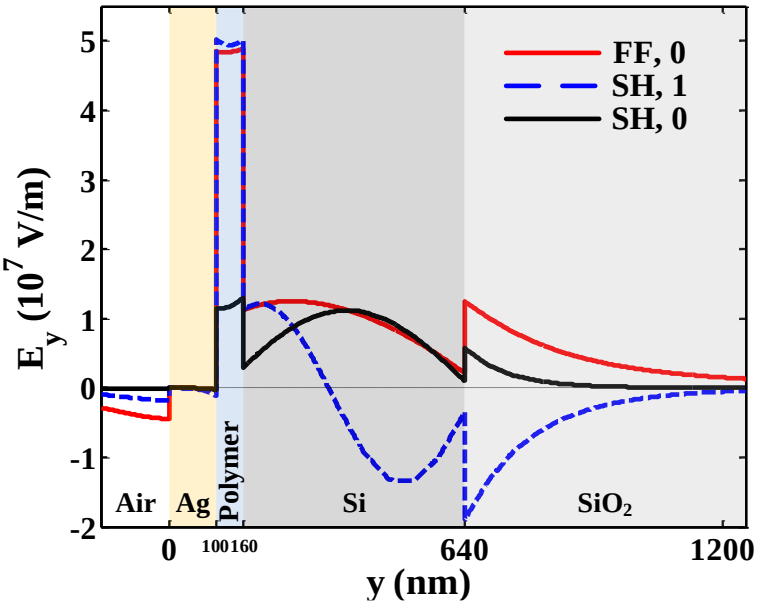

Fig.4.3 distributions on the center line along y-direction (powers of modes have been normalized to 1 W).

4.1.3 Efficient SHG in the proposed hybrid plasmonic waveguide

Then, we investigate the SHG process in this waveguide by solving the nonlinear coupling-wave equations proposed in Chapter 2.

$$\begin{aligned}\frac{\partial A_{FF,0}}{\partial z} &= -\frac{\alpha_{FF,0}}{2}A_{FF,0} + i\frac{\omega}{4}\sum_{m=0}^{1}\kappa_{FF}^{m0}A_{FF,0}^{*}A_{SH,m}\exp(i\Delta\beta_{m0}z)\\ \frac{\partial A_{SH,m}}{\partial z} &= -\frac{\alpha_{SH,m}}{2}A_{SH,m} + i\frac{\omega}{4}\kappa_{SH}^{m0}A_{FF,0}A_{FF,0}\exp(-i\Delta\beta_{m0}z)\end{aligned} \tag{4.1}$$

where A are the slowly varying complex amplitudes, $\Delta\beta_{m0} = \beta_{SH,\,m} - 2\beta_{FF,\,0}$ (m = 0, 1) are the phase mismatch, β = Re(n_{eff})$2\pi/\lambda$ and α = Im(n_{eff})$4\pi/\lambda$ represent the phase propagation constant and attenuation coefficient, respectively. $\kappa_{FF,SH}^{m0}$ (m = 0, 1) are the nonlinear coupling coefficients (NCC), which are defined by

$$\kappa_{FF}^{m0} = \varepsilon_0 \iint \chi^{(2)} : \vec{E}_{SH,m} \vec{E}^{*}_{FF,0} \bullet \vec{E}'_{FF,0} dxdy$$
$$\kappa_{SH}^{m0} = \varepsilon_0 \iint \chi^{(2)} : \vec{E}_{\mathrm{FF},0} \vec{E}_{\mathrm{FF},0} \bullet \vec{E}'_{\mathrm{SH,m}} dxdy \quad (4.2)$$

with $\vec{E}$ being the normalized mode profiles. The calculated NCC values are κ_{10} = 141 $\mathrm{psm^{-1}W^{-1/2}}$ and κ_{00} = 66 $\mathrm{psm^{-1}W^{-1/2}}$, respectively. It is interesting to underline that the NCC between the interacting phase-matched modes with different orders is larger than that between the two fundamental modes. It is known indeed that the 0-th mode of a dielectric waveguide is even with respect to the transverse direction and that the 1-st mode is odd, which usually leads to small NCC between these two kinds of modes. In our case, the 1-st mode at the SHF keeps the odd feature as its tail into the silicon layer undergoes a sign change of the field distribution, but the sign change only occurs in the high-index silicon part. In the nonlinear integration area (NP slot), however, the two signs are the same and both considered phase-matched modes are locally enhanced due to their plasmonic-like natures. This results in a large overlap integration in the nonlinear part between the two modes with different orders.

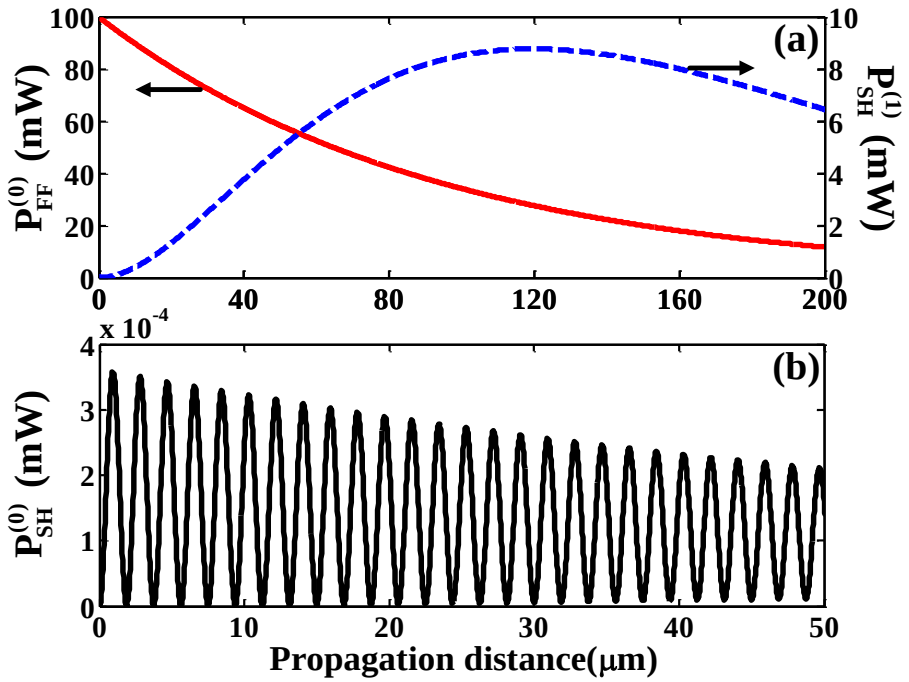

Fig.4.4 Intensity variations in the propagation with pump power of 100 mW.

Fig. 4.4 shows the SHG conversion properties along propagation considering a pump power at FF of only 100 mW (20 dBm). For the 0-th mode at FF shown by the red solid line in Fig. 4.4(a), its power decreases monotonously due to the conversion

process and loss. The conversion mainly contributes to the generation of the 1-st mode at SH (blue dashed line), which reaches its maximum up to 8.8 mW (9.5 dBm) at the propagation distance of 119.65 μm. Compared to this, the generated 0-th mode at SH is very weak and oscillatory along propagation due to phase mismatch and low NCC, as plotted in Fig. 4.4(b). Besides, it should be noted that even with a pump power as low as 10 mW, the nonlinear conversion efficiency, which is defined as $\max\left(P_{SH}\right)/\left[P_{FF}^{2}(0)L_{SH}^{p}(cm)\right]$, with L_{SH}^{p} being the propagation length of the SH mode, is calculated to be 14, which is two orders of magnitude larger than the previously reported value in plasmonic slot waveguides that considered a high pump of 1 W [141].

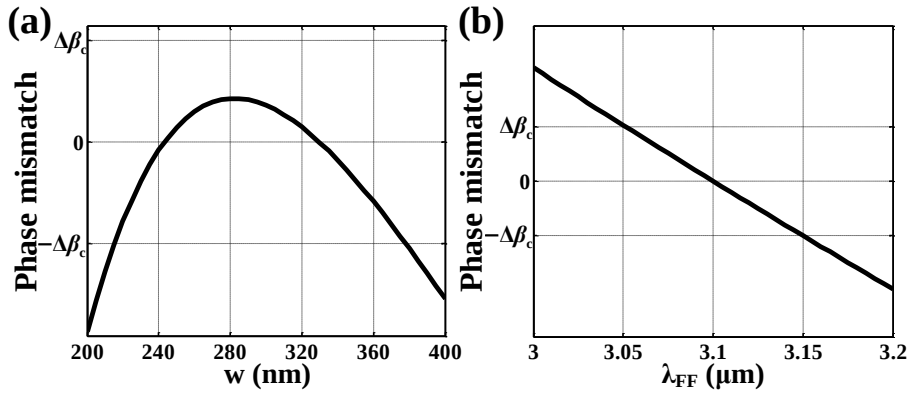

Fig. 4.5 Phase mismatch as functions of (a) width; and (b) wavelength of FF.

We also emphasize the flexibility of the proposed SOHPW geometry for nonlinear conversion with respect to the phase matching condition. The related phase matching tolerance can be written as $|\Delta\beta| < \Delta\beta_c = 2\pi/L$ with the considered device length L [52]. With L = 120 μm, $\Delta\beta_c$ is here of 5.236 $\times 10^4$ rad/m. Fig. 4.5(a) and (b) show the phase mismatch between the 0-th mode at FF and 1-st mode at SH as a function of the waveguide width w and the FF wavelength, respectively. It is shown that the condition $|\Delta\beta| < \Delta\beta_c$ is satisfied for a wide range of width (215 nm – 378 nm) and a wide range of wavelength (3050 nm – 3150 nm). This result is due to the strong similarity of the dispersion properties between the two interacting modes and to the short needed waveguide length.

4.1.4 Conclusion

In conclusion, we propose a nonlinear SOHPW and investigate the efficient SHG process induced in this waveguide. Due to a specific hybridization approach of the involved modes, the nonlinear coupling coefficient between the two involved plasmonic-like modes with different orders is larger than that between the two fundamental modes. The capability of supporting efficient SHG within short distances, big fabrication-error tolerance and broad bandwidth make it very promising for future highly-integrated nanophotonic circuits.

4.2 Further enhancement of second harmonic generation with microring resonators

Microring resonators (MRR) have been proposed to be an attractive component in silicon photonics to reinforce optical nonlinearities and realize efficient and compact nonlinear frequency conversions because of the large field enhancements around resonant wavelengths provided by the MRR. [150, 202-208]. The combination of hybrid plasmonic waveguides (HPW) and MRR has been proposed in several works in which the HPW-based MRR support subwavelength or even submicron radii and large field enhancements in the low-index slot area [99, 103-105, 209]. However, most of these works were focused on the linear response of the MRR. In this work, we apply the same HPW as the one proposed in the previous section into a MRR configuration. By setting both the fundamental frequency (FF) and the second harmonic frequency (SHF) at two different resonant wavelengths, a further enhancement factor of SHG efficiency by almost two orders of magnitude is predicted.

4.2.1 Microring structure and design

The proposed silicon-organic hybrid plasmonic microring resonator (SOHPMR) is shown in Fig. 4.6. The straight access waveguide with width w_a is coupled with the ring through a gap distance of g. The radius and width of the bended waveguide are R and

w, respectively. The cross-section of the HPW is characterized by a NP with a thickness of h_p = 70 nm, well suited to find a phase matching point in a bended waveguide, as shown hereafter. The thicknesses of the Ag and Si layers are h_m = 100 nm and h_{Si} = 480 nm, respectively. The polymer is chosen as the doped, crosslinked organic polymer with a refractive index of n = 1.643 and a nonlinear susceptibility of $\chi^{(2)}_{111}$ = 619 pm/V at the wavelength of 1550 nm [35]. The pump light at the FF of λ_1 = 3.1 μm is coupled into the SOHPMR with reasonable powers (values are given hereafter). The expected SHF at $\lambda_2 = \lambda_1/2$ = 1.55 μm is generated and outputs from the through port of the SOHPMR.

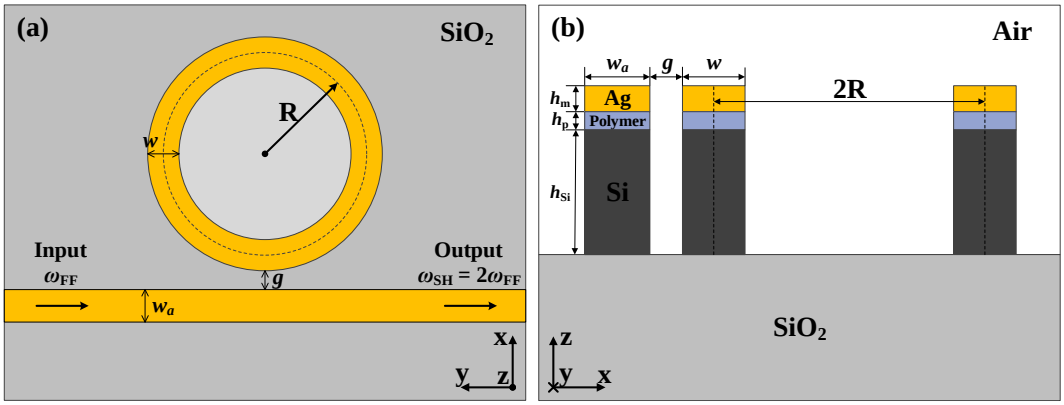

Fig. 4.6 Schematic of the silicon-organic hybrid plasmonic microring resonator. Cross-sectional views along the (a) xy and (b) xz planes.

Such a device can be fabricated by silicon clean room technological processes. Firstly, the polymer can be spin-coated onto the silicon layer and then by defining a mask on the wafer and etching through, the MRR configuration can be defined. Following this, metallic layers can be deposited on top through a lift-off process.

Using the modal phase-matching method, the needed phase-matching condition (PMC) to enhance the nonlinear SHG process can be realized between the fundamental (0-th) mode at FF and the second-order (1-st) mode at SHF in the straight HPW [113]. Based on the same mechanism, the new phase-matching points in the bend-waveguide configuration have been searched. The modal properties of bended waveguides have

been analyzed by 2D axisymmetric simulation in COMSOL. Material dispersion for modeling the refractive index of SiO_2, Si and Ag were taken from Refs. [47], [46] and [49], respectively. Fig. 4.7 shows the difference of the effective refractive index between the interacting two modes as a function of the radius R and width w of the bended waveguide. Note that the fundamental mode of the SHF was not considered in this study. The black line marks out the zero value, i.e. the phase matching line. One can see that the PMC can be fulfilled in the bended HPW as well and that for most of radius values, two phase matching points can be found.

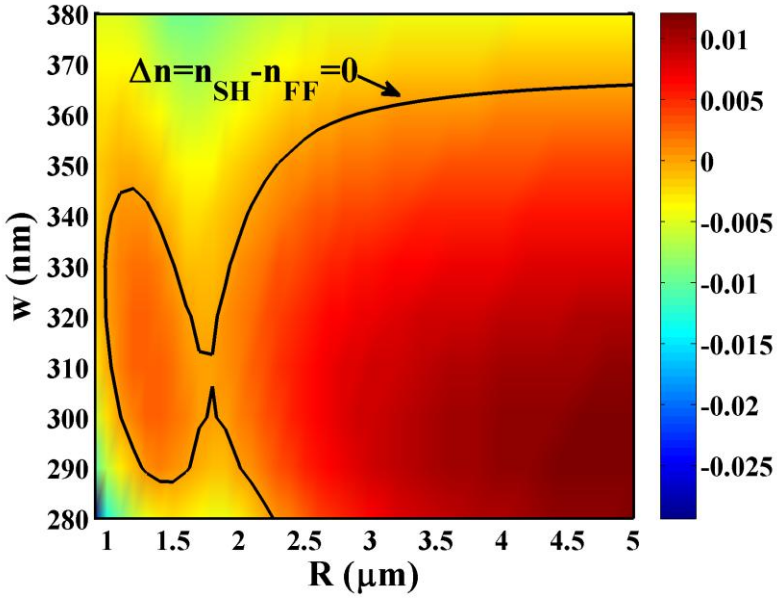

Fig. 4.7 $\Delta n = n_{SH} - n_{FF}$ as functions of the radius and width of the bended waveguides. The black line represents the zero value, i.e. the phase matching line.

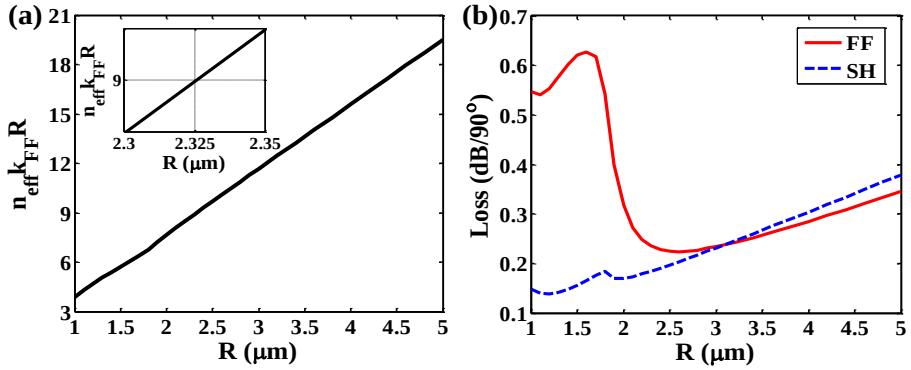

Fig. 4.8 (a) $n_{eff}k_{FF}R$ and (b) loss of a 90° bend at the phase matching line as functions of the radius. The inset in (a) is an enlarged view near $n_{eff}k_{FF}R = 9$.

Next, the locations of the resonant wavelengths for the ring have been adjusted in order to match with the two frequencies of interest for the reinforcement of the SHG process. Stating that a resonance into the ring happens when $n_{eff}k_{FF}R = m$ (m is an integer and known as the azimuthal number of the resonance), where n_{eff} and k_{FF} are the effective refractive index and propagation constant, respectively, the "$n_{eff}k_{FF}R$" quantity has been plotted as a function of radius in Fig. 4.8(a). For each radius value, the larger waveguide width on the top phase matching line has been chosen correspondingly. Combining this condition with the minimization of the 90˚-bending HPW losses for the two frequencies of interest (shown in Fig. 4.8 (b)), the m = 9 value was finally chosen. Optimal radii near 2.6 μm and 2 μm were found for the FF and SHF, respectively, where a minimum loss level was obtained due to the joint contributions from the radiation (increasing exponentially with a radius decrease) and the intrinsic losses of the waveguide resulting from the metal absorption [103]. As shown in the inset of Fig. 4.8(a), the corresponding geometrical parameters for m = 9 are R = 2.325 μm and w = 351 nm ≈ 350 nm, which are the final geometrical parameters that were chosen.

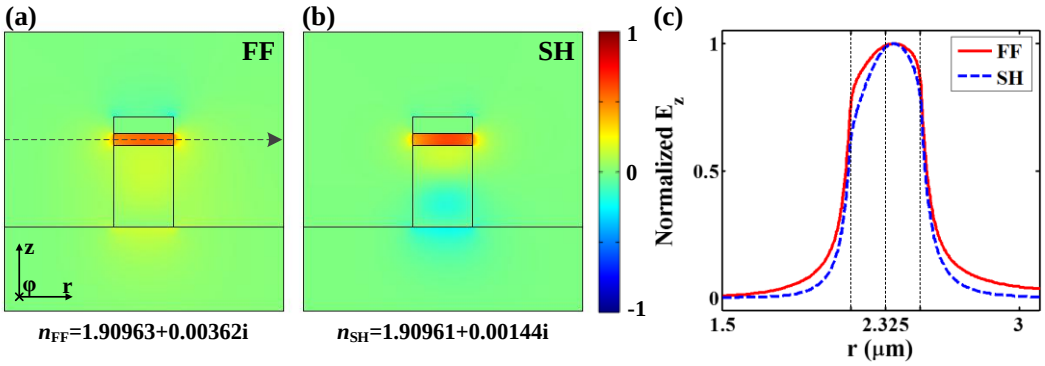

Fig. 4.9 E_z distributions for the phase-matched modes at FF (a) and SH (b) when R = 2.325 μm and w = 351 nm. (c) is the normalized E_z distribution on the center line of the slot along r direction.

The obtained phase-matched field distributions are shown in Fig. 4.9, where Fig. 4.9(a) and (b) plot the E_z distributions of the 0-th mode at FF and 1-st mode at SHF,

respectively. The effective refractive indices of the two modes are n_{FF} = 1.90963+0.00362i and n_{SH} = 1.90961+0.00144i, respectively. Fig. 4.9(c) shows the normalized E_z profiles on the center line of the slot along the r direction, as marked out in Fig. 4.9(a). We can see that the peak value of the field is not located at the center of the waveguide because of the bended-waveguide property.

The width of the access waveguide was then designed as w_a = 358.3 nm ≈ 360 nm in order to maximize the fraction of FF field coupled into the ring. Then, n_{FF} = 1.90968+0.00271i and n_{SH} = 1.91268+0.00139i for the access waveguide. At last, in order to set a comparison benchmark for the SHG efficiency in the ring resonator configuration with previous results, the efficiency of the SHG process in a straight HPW was complementary estimated (with w = 369.2 nm ≈ 370 nm in this case for PMC consideration).

4.2.2 Nonlinear model approach

In this subsection, we derive the enhancement factor for the SHG in a ring resonator when compared to a single waveguide. In a single lossy waveguide propagating along +z direction, the nonlinear coupled equations (NCE) for the SHG are [94]:

$$\begin{aligned}\frac{\partial A_{FF}}{\partial z} &= -\frac{\alpha_{FF}}{2}A_{FF} + i\frac{\omega_{FF}}{4}\kappa_{FF}A_{FF}^{*}A_{SH}\exp(i\Delta\beta z)\\ \frac{\partial A_{SH}}{\partial z} &= -\frac{\alpha_{SH}}{2}A_{SH} + i\frac{\omega_{FF}}{4}\kappa_{SH}A_{FF}A_{FF}\exp(-i\Delta\beta z)\end{aligned} \tag{4.3}$$

where ω_{FF} is the angular frequency of the fundamental frequency (FF). $A_{FF,SH}$ are the slowly varied complex mode amplitudes. $\Delta\beta = \beta_{SH} - 2\beta_{FF}$ is the phase mismatch. $\beta_{FF,SH}$ and $\alpha_{FF,SH}$ represent the phase propagation constant and attenuation coefficient, respectively. And $\kappa_{FF,SH}$ are the nonlinear coupling coefficients, which are defined by:

$$\begin{aligned}\kappa_{FF} &= \varepsilon_0\iint\left\{\chi^{(2)}:\vec{E}_{SH}(x,y)\vec{E}_{FF}^{*}(x,y)\cdot\vec{E}_{FF}{}'(x,y)\right\}dxdy\\ \kappa_{SH} &= \varepsilon_0\iint\left\{\chi^{(2)}:\vec{E}_{FF}(x,y)\vec{E}_{FF}(x,y)\cdot\vec{E}_{SH}{}'(x,y)\right\}dxdy\end{aligned} \tag{4.4}$$

with $\vec{E}_{FF,SH}(x,y)$ and $\vec{E}_{FF,SH}{}'(x,y)$ the mode profiles which have been normalized. $\vec{E}_{FF,SH}{}'(x,y)$ are the modes propagating along –z direction. Under the approximation where the pump is not depleted by the nonlinear conversion process, one can solve Eq. (4.3) analytically to obtain [59]:

$$\begin{aligned} A_{FF} &= A_{FF}(0)\exp(-\frac{\alpha_{FF}}{2}z) \\ A_{SH} &= i\frac{\omega_{FF}}{4}\kappa_{SH}L_{eff}(z)A_{FF}^2(0)\exp(-\frac{\alpha_{SH}}{2}z)+A_{SH}(0)\exp(-\frac{\alpha_{SH}}{2}z) \end{aligned} \tag{4.5}$$

where the effective length is

$$L_{eff}(z)=\frac{1-\exp[-(\alpha_{FF}-\alpha_{SH}/2+i\Delta\beta)z]}{\alpha_{FF}-\alpha_{SH}/2+i\Delta\beta} \tag{4.6}$$

So the SHG efficiency in a lossy waveguide with length of L is:

$$\eta_1=\frac{|A_{SH}(L)|^2}{|A_{FF}(0)|^2}=\frac{\omega_{FF}^2}{16}\kappa_{SH}^2L_{eff}^2(L)\exp(-\alpha_{SH}L)P_{FF}(0) \tag{4.7}$$

Note that this single waveguide can be a straight or a bended waveguide.

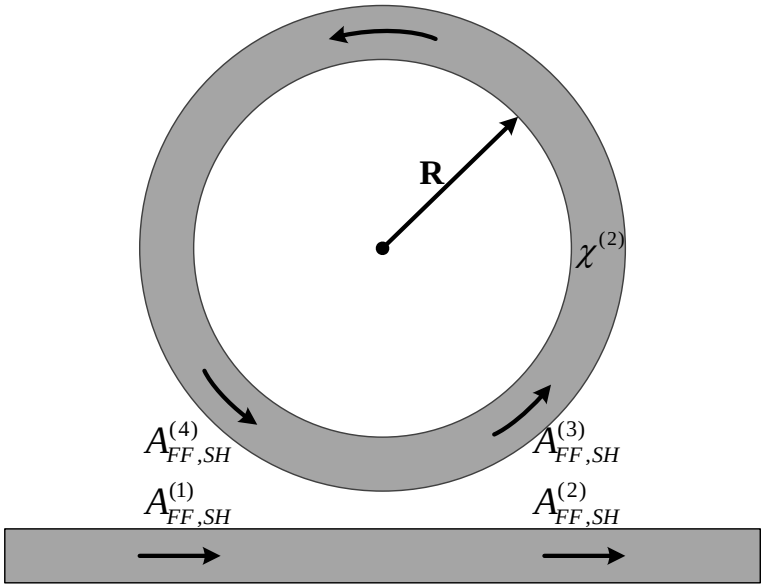

Fig. 4.10 Schematic of second harmonic generation in a single pass micro-ring resonator

Next, we deduce the theory of SHG in a microring resonator (MRR), starting from

the schematic of Fig. 4.10. The interactive waves satisfy the following equations:

$$\begin{aligned} A_{FF,SH}^{(2)} &= t_{FF,SH} A_{FF,SH}^{(1)} + ic_{FF,SH} A_{FF,SH}^{(4)} \\ A_{FF,SH}^{(3)} &= ic_{FF,SH} A_{FF,SH}^{(1)} + t_{FF,SH} A_{FF,SH}^{(4)} \end{aligned} \tag{4.8}$$

The complex mode amplitudes A are normalized, so that their squared magnitude corresponding to the modal power. c and t are coupling and transmission coefficients with $|c|^2+|t|^2=1$. Besides, based on Eq. (4.5), we can obtain:

$$\begin{aligned} A_{FF}^{(4)} &= A_{FF}^{(3)} \exp[(i\beta_{FF} - \frac{\alpha_{FF}}{2})L] \\ A_{SH}^{(4)} &= i\frac{\omega_{FF}}{4}\kappa_{SH} L_{eff}(L)[A_{FF}^{(3)}]^2 \exp[(i\beta_{SH} - \frac{\alpha_{SH}}{2})L] + A_{SH}^{(3)} \exp[(i\beta_{SH} - \frac{\alpha_{SH}}{2})L] \end{aligned} \tag{4.9}$$

where L is the circumference of the microring given by $L = 2\pi R$ with R being the radius of the ring. $L_{eff}(L)$ is the effective length defined in Eq. (4.6). The incident condition of the SHG is:

$$A_{FF}^{(1)} = A_{FF}^{(in)},\ A_{SH}^{(1)} = 0 \tag{4.10}$$

Based on Eq. (4.8) through (4.10), we can obtain:

$$\begin{aligned} A_{FF}^{(2)} &= \left\{ t_{FF} - c_{FF} F_{FF} \exp[(i\beta_{FF} - \frac{\alpha_{FF}}{2})L] \right\} A_{FF}^{(in)} \\ A_{FF}^{(3)} &= iF_{FF} A_{FF}^{(in)} \\ A_{FF}^{(4)} &= iF_{FF} \exp[(i\beta_{FF} - \frac{\alpha_{FF}}{2})L] A_{FF}^{(in)} \\ A_{SH}^{(2)} &= \frac{\omega_{FF}}{4}\kappa_{SH} L_{eff}(L) F_{FF}^2 F_{SH} \exp[(i\beta_{SH} - \frac{\alpha_{SH}}{2})L][A_{FF}^{(in)}]^2 \\ A_{SH}^{(3)} &= -i\frac{\omega_{FF}}{4}\frac{t_{SH}}{c_{SH}}\kappa_{SH} L_{eff}(L) F_{FF}^2 F_{SH} \exp[(i\beta_{SH} - \frac{\alpha_{SH}}{2})L][A_{FF}^{(in)}]^2 \\ A_{SH}^{(4)} &= -i\frac{\omega_{FF}}{4c_{SH}}\kappa_{SH} L_{eff}(L) F_{FF}^2 F_{SH} \exp[(i\beta_{SH} - \frac{\alpha_{SH}}{2})L][A_{FF}^{(in)}]^2 \end{aligned} \tag{4.11}$$

where the $F_{FF,SH}$ are the field enhancement factors, which can be written as:

$$F_{FF,SH} = \frac{c_{FF,SH}}{1 - t_{FF,SH} \exp[(i\beta_{FF,SH} - \alpha_{FF,SH}/2)L]} \tag{4.12}$$

The SHG conversion efficiency is:

$$\eta_2 = \frac{\left|A_{SH}^{(2)}\right|^2}{\left|A_{FF}^{(in)}\right|^2} = \frac{\omega_{FF}^2}{16}\kappa_{SH}^2 L_{eff}^2(L) F_{FF}^4 F_{SH}^2 \exp(-\alpha_{SH} L) P_{FF}^{(in)} \tag{4.13}$$

Compared to the SHG efficiency in a single waveguide of Eq. (4.7), the efficiency in a MRR is enhanced by a factor of $F_{FF}^4 F_{SH}^2$. However, it should be noted that the linear losses of the bended waveguide in the MRR here include the intrinsic loss of the waveguide and the bend radiation loss, which makes them larger than that for a straight waveguide. The real enhancement factor would be thus smaller than $F_{FF}^4 F_{SH}^2$. Specifically, at the considered phase-matching and resonating point considered in this study, where $\beta_{SH} = 2\beta_{FF} = 2m/R$ with m being an integer, the effective length and field enhancement factor are:

$$\begin{aligned} L_{eff}(L) &= \frac{1-\exp[-(\alpha_{FF} - \alpha_{SH}/2)L]}{\alpha_{FF} - \alpha_{SH}/2} \\ F_{FF,SH} &= \frac{c_{FF,SH}}{1 - t_{FF,SH}\exp(-\frac{\alpha_{FF,SH}}{2}L)} \end{aligned} \tag{4.14}$$

On this circumstance, the SHG shows best performance.

In the analytic solution of Eq. (4.5) and Eq. (4.9) for the NCE of Eq. (4.3), we have made an approximation that the pump is not depleted by the nonlinear conversion. Now we confirm the accuracy of this approximation by comparing the analytic solution with the numerical solution obtained by calculating the NCE directly. Fig. 4.11(a) shows the SHG efficiency as a function of the propagation length in the straight HPW when the input pump power of the FF is $P_{FF}^{(in)}$ = 20 mW. The dashed line and solid line are the analytic solution and numerical solution, respectively. When the MRR works at the critical coupling point for the FF, i.e. $t_{FF} = \exp(-\pi\alpha_{FF}R)$, the field enhancement factor in Eq. (4.13) is calculated to be F_{FF} = 2.276. The power of FF in the MRR is $F_{FF}^2 P_{FF}^{(in)}$ = 103.6 mW. Taking this power as the input power of FF, Fig. 4.11(b) shows the

comparison for the bend waveguide with radius of R = 2.325 μm. One can see that, for both the straight and bend waveguides we study in this work, the analytic solution for the NCE is accurate when the length of the waveguide is smaller than 40 μm. For the final structure we choose, the circumference of the ring is $L = 2\pi R$ = 14.6 μm. Based on the above analysis, it is reasonable to apply the analytic solution in Eq. (4.5) and Eq. (4.9). Lastly, it should be noted that this analytic solution is only applicable under the condition of low pump power and short waveguide length. Otherwise the direct calculation of the NCE is required.

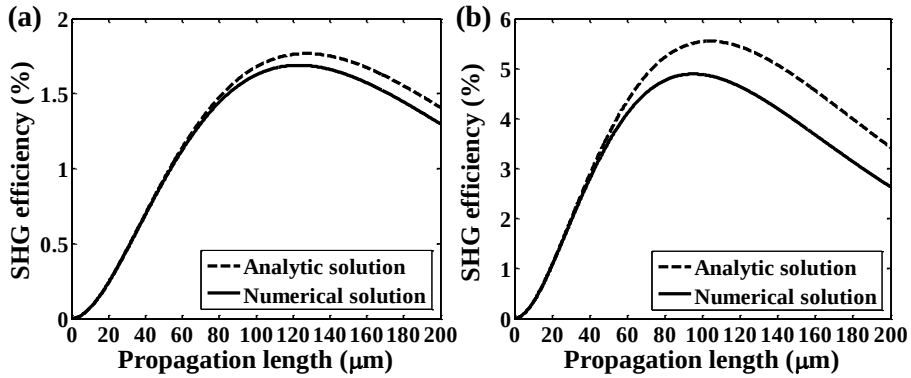

Fig. 4.11 Analytic solution and numerical solution of the SHG efficiency as functions of the propagation length in the (a) straight waveguide and (b) bended waveguide.

4.2.3 Enhanced second harmonic generation in microring resonators

In the first benchmarking single straight HPW considered configuration, the nonlinear coupled coefficient was calculated to be κ_{SH} = 134 $psm^{-1}W^{-1/2}$. Then by using Eq. (4.7), the SHG efficiency was estimated as η_1 = 0.14% for an input pump power $P_{FF}^{(in)}$ = 20 mW and a waveguide length of 14.6 μm corresponding to the unfolded circumference of the microring resonator considered in a second step. Similarly, by using Eq. (4.13), the SHG efficiency was newly obtained in the MRR configuration under the same pumping power condition. The nonlinear coupled coefficient was then κ_{SH} = 130 $psm^{-1}W^{-1/2}$ for the bended waveguide case.

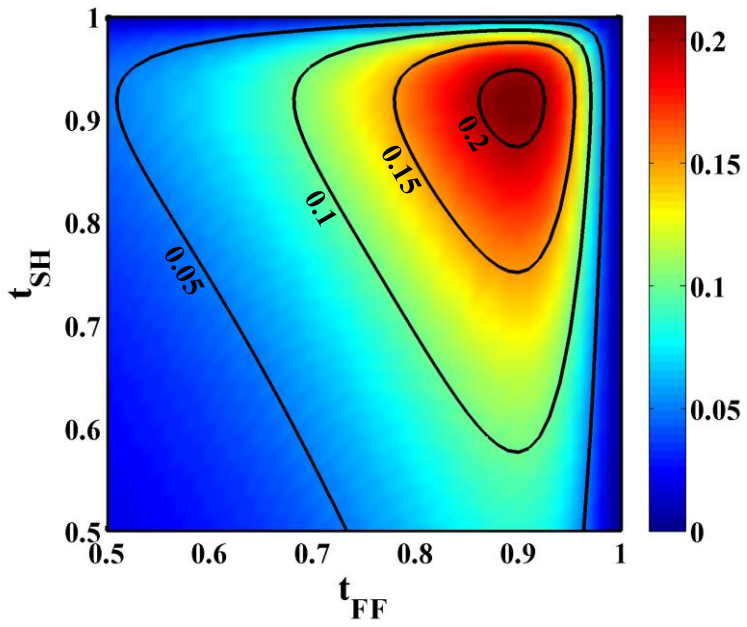

Fig. 4.12 SHG efficiency η_2 as functions of the transmission coefficients for FF t_{FF} and SHF t_{SH}.

Fig. 4.12 shows the final MRR-enhanced SHG efficiency η_2 as a function of the two waveguide-to-ring transmission coefficients for the FF (t_{FF}) and SHF (t_{SH}), respectively. As visible, a peak efficiency up to η_2 = 21% is realized when the MRR works at the critical coupling point for both the FF and SHF, i.e. when $t_{FF} = \exp(-\pi\alpha_{FF}R) = 0.898$ and $t_{SH} = \exp(-\pi\alpha_{SH}R) = 0.918$. A maximum enhancement factor of $\eta_2/\eta_1 = 150$ is then expected. However, it is worth noting that it is not possible to let the FF and SH work at the critical coupling points at the same time in practice. Usually, t_{SH} is larger than t_{FF} for a same MRR because the waveguide mode at SH extends less beyond the waveguide boundary due to smaller wavelength. Despite of this, an optimal point can be envisaged in practice by adjusting the geometrical parameters of the MRR.

All the other geometrical parameters being fixed, the coupling and transmission coefficients of the MRR are only controlled by the thickness of the gap g between the access waveguide and the ring. Fig. 4.13(a) shows the transmission coefficients for the two wavelengths of interest as a function of the gap parameter g. Here the coupling coefficients are calculated by making use of the coupled mode theory for microring

resonators [210, 211]. Fig. 4.13(b) is the corresponding SHG conversion efficiency for different gap thicknesses. As can be seen, there is an optimal gap of g = 175 nm, where the SHG efficiency is η_2 = 13.71 %. Correspondingly, t_{FF} = 0.8088 and t_{SH} = 0.9666, respectively. Fig. 4.13(c) shows the SHG enhancement factor described by $F_{FF}^4 F_{SH}^2$ and the realistic enhancement η_2/η_1 ratio as functions of g. For the optimal gap of 175 nm, a maximum enhancement up to $\eta_2/\eta_1 \sim 100$ is thus possible in practice by changing the straight HPW configuration into the MRR one. Another interesting point lies in the critical point for FF, where no FF light would couple out from the through port. It happens when g = 251 nm. At this point, t_{FF} = 0.898 and t_{SH} = 0.988. The SHG efficiency is then η_2 = 9.2%, which means an MRR-enhancement factor of still 66.

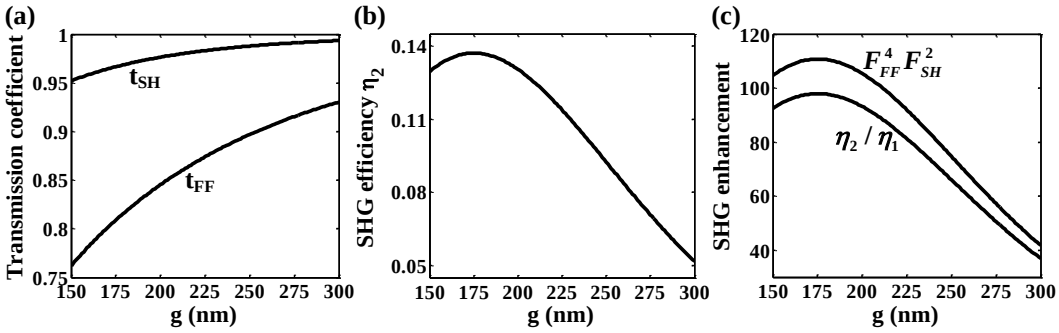

Fig. 4.13 (a) Transmission coefficients for two wavelengths, (b) the final SHG conversion efficiency and (c) enhancement factor in the ring as a function of the gap.

In order to further confirm the veracity of the proposed scheme, we have calculated the transmission spectra of the MRR around the SHF and FF in a three dimensional (3D) structure. The software FDTD Lumerical was used to carry out the 3D full-wave simulation. In the simulation, some efforts have been made to make the model convergent. We have modified the perfect matched layer (PML) settings by increasing the "pml kappa" from the original value of 2 to 10, decreasing the "pml sigma" from the original value of 0.25 to 0.15, and changing the "type of pml" from the original type of standard to stabilized. In the time step setting, we have modified the "dt stability factor" from the original value of 0.99 to 0.8. For the mesh setting, we defined an override mesh region near the metal-polymer interface with mesh size of $dx = dy = dz$

= 5 nm. The mesh accuracy for the remaining regions has been chosen to be 3.

The calculated results are shown in Fig. 4.14. Two resonant wavelengths of 1548.4 nm and 3099 nm are presented. The slight difference over the previous mode analysis is probably due to the applied different mesh sizes and different calculation methods in the finite-element mode analysis and 3D FDTD simulation. The MRR shows small extinction ratios as it works deviating from the critical points especially at the SHF. Fig. 4.14(b) and (d) show the E_z distributions at the SHF and FF, respectively. We can see the MRR resonates at both wavelengths and the azimuthal number at two wavelengths are 9 and 18, respectively. This agrees well with the previous mode analysis.

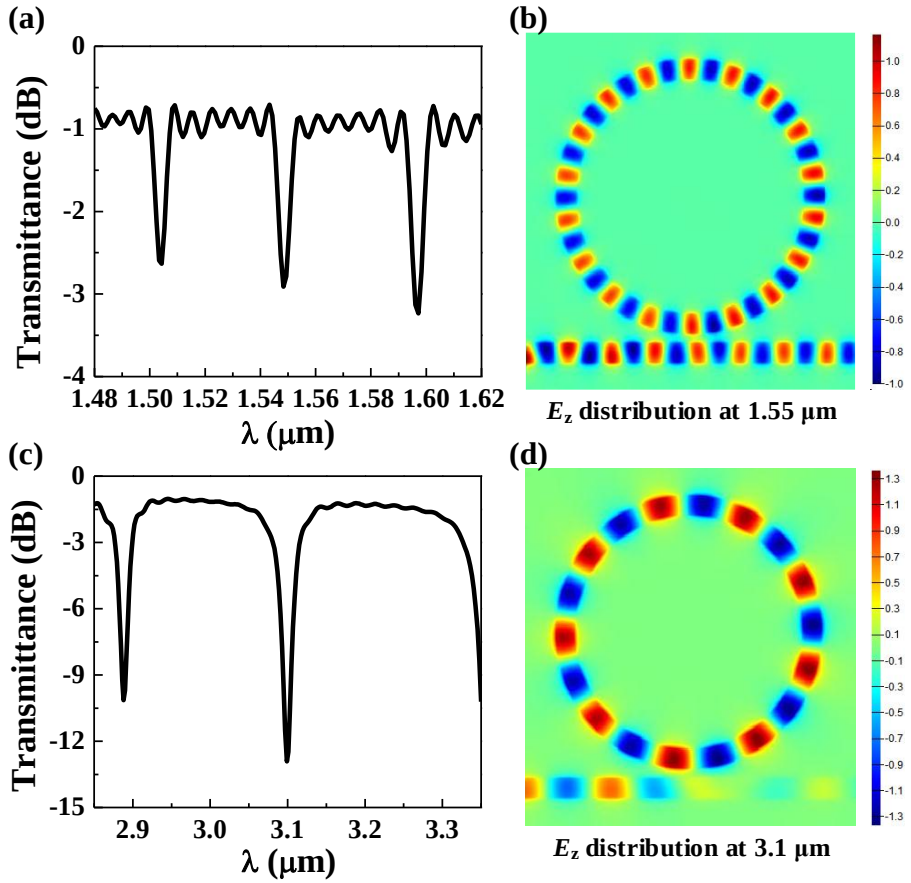

Fig. 4.14 Transmission spectra of the 3D MRR structure around (a) the SHF of 1.55 μm and (c) the FF of 3.1 μm when R=2.325μm, w_a=358.3nm, w=351nm and g=175nm. The two resonant wavelengths are 1548.4 nm and 3099 nm. (b) and (d) are the E_z distributions at SHF and FF, respectively.

In the meantime, we finally estimated the robustness of the present results with respect to the additional optical losses due to the side-wall roughness coming from lithographic and etching steps used to define the investigated structure. In this purpose, we considered the last optimized configuration with loss coefficients of the bended HPW at the FF and SHF given by α_{FF} = 638 dB/cm and α_{SH} = 509 dB/cm, respectively and anticipated from this initial condition an increase of α_{FF} and α_{SH}. The result is plotted in Fig. 4.15, in which the left bottom corner corresponds to the bottom loss level coming from the absorption of the metallic layer and radiation losses only. As shown here, the SHG efficiency only slightly drops from 13% to 10% even for extremely large extrinsic losses eventually coming from the fabrication process. This point and the quantitative results provided by the 3D performed FDTD simulations (Fig. 4.14) assess the strong potential of the proposed approach for SHG enhancement in the ultra-small footprint silicon plasmonic ring resonator structures.

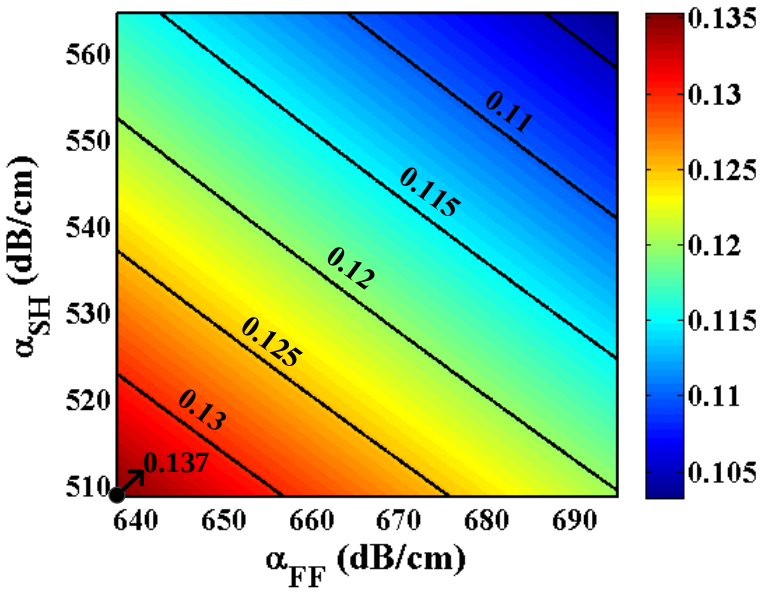

Fig. 4.15 SHG efficiency η_2 as a function of the attenuation coefficients for FF (α_{FF}) and SH (α_{SH}).

4.2.4 Conclusion

To conclude this part, a HPW geometry based on a microring configuration has been proposed to further enhance the second harmonic generation (SHG) process on the

silicon photonics platform. By taking the phase matching, resonance and loss level into consideration, the conversion properties are shown to be improved in three aspects: the needed pump power becomes lower, the size of the device is smaller and the efficiency of the SHG is larger.

In the proposed final geometry, a SHG conversion efficiency of around 13.7% is predicted for a pump power as low as 20 mW and a ring radius of 2.325 μm. This obtained dramatic improvement of the nonlinear efficiency with respect to previous results opens avenues to practical applications using low-power nonlinear SHG-based all-optical on-chip signal processing.

4.3 Phase regeneration of phase shift keying signals in hybrid plasmonic waveguides

4.3.1 Introduction

In the last two sections, hybrid plasmonic waveguides (HPW) have shown the ability to enhance the efficiency of nonlinear mechanisms (mainly SHG) with low power and within short distance. In this section we finish the chapter by showing one possible application of the HPW-enhanced nonlinear effects for on-chip optical signal processing. Specifically, the work is based on a novel symmetric hybrid plasmonic waveguide (SHPW), which consists of a traditional long-range surface plasmon polariton (LRSPP) waveguide with two high-index slabs placed symmetrically near the top and bottom surfaces of the metallic layer [212, 213].

In SHPW, the loss is even lower while the field confinement is comparable when compared to the conventional HPW. The nonlinear effects in this kind of waveguides may be prominent but have not been studied yet to our best knowledge. In this section, we investigate the nonlinear optical parametric amplification (OPA) process induced in a SHPW with nonlinear polymer (NP) as the active materials. The simulation results reveal that it enables efficient OPA within a short distance around 180 μm. Based on

that, we explore a potential application, the phase regeneration of degraded phase shift keying (PSK) signals, which is of great significance in optical signal processing.

4.3.2 Waveguide structure and efficient optical parametric amplification

The SHPW studied in this paper has a similar structure as in [212], with a nanometer size metallic layer sandwiched between two NP layers surrounded by two silicon layers, as shown in Fig. 4.16(a). In the waveguide, the refractive index of silicon at the signal wavelength (SW) of λ_s = 1550 nm and pump wavelength (PW) of λ_p = 775 nm are 3.48 and 3.71, respectively. Metal is defined as silver with a height h_m. The NP has a height h_p and is chosen to be the commercially available M1 organic material consisting of chromophores dispersed in a polymer matrix, with refractive index 1.6 and high nonlinear susceptibility $\chi^{(2)}_{111}$ = 230 pm/V at the wavelength of 1550 nm [162]. Besides, polymer is compatible with silicon and can be periodically poled for the purpose of quasiphase matching [214, 215].

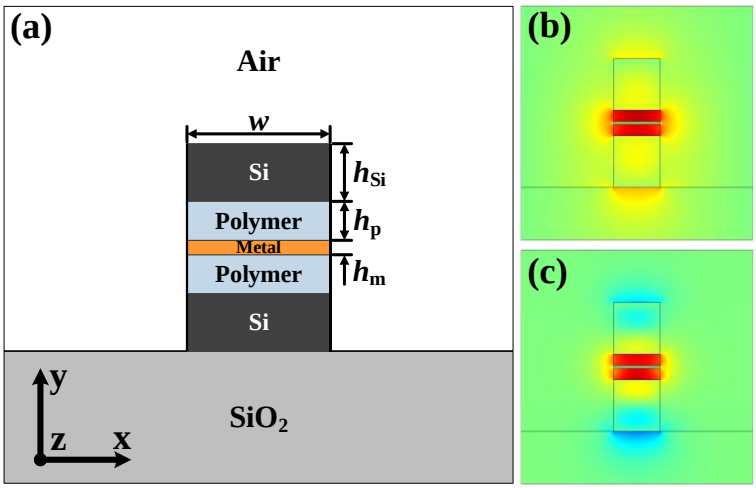

Fig. 4.16 (a) Schematic diagram of the proposed SHPW. E_y distributions at (b) SW of 1550 nm and (c) PW of 775 nm (w = 200 nm, h_m = 10 nm, h_p = 50 nm and h_{Si} = 220 nm).

The related configuration can also be fabricated with clean room technologies. Firstly, the polymer can be spin-coated onto a SOI wafer and then by defining a mask on the wafer and etching through, the waveguide configuration can be defined.

Following this, metallic layers can be deposited on top through a lift-off process. Then, the top polymer layer can be realized with another step of spin-coating. Finally, the top silicon layer which made of amorphous silicon can be deposited by plasma-enhanced chemical vapor deposition technique [216].

Fig. 4.16(b) and (c) show the mode profiles of dominant component E_y at the SW and PW, respectively. The modes are calculated with a finite-element based commercial software (COMSOL Multiphysics) and structural parameters are chosen as: w = 200 nm, h_m = 10 nm, h_p = 50 nm, h_{Si} = 220 nm. It is shown that most of the fields are concentrated and enhanced within and near the low refractive index NP region both at the SW and PW. This results from the discontinuity of the E_y component at the high index contrast interfaces. The effective refractive indices of the hybrid modes are 1.59 + 8.60 $\times 10^{-5}$i and 1.81 + 8.35 $\times 10^{-5}$i at SW and PW, respectively. For the SW, a LRSPP-like hybrid mode [77] comes into being from the strong coupling of the LRSPP mode and the fundamental guided mode. With respect to the PW, however, a more like LRSPP hybrid mode is formed due to the weaker coupling of the LRSPP mode and the second-order guided mode at smaller wavelength, which results in more fields confined in the NP part and larger losses.

Then, we investigate the OPA process in this waveguide by solving the nonlinear coupling-wave equations.

$$\begin{aligned}\frac{\partial A_s}{\partial z} &= -\frac{\alpha_s}{2}A_s + i\frac{\omega_s}{4}\kappa_s A_s^* A_p \exp(i\Delta\beta z)\\ \frac{\partial A_p}{\partial z} &= -\frac{\alpha_p}{2}A_p + i\frac{\omega_s}{4}\kappa_p A_s A_s \exp(-i\Delta\beta z)\end{aligned} \tag{4.15}$$

where $A_{s,p}(z) = \left|A_{s,p}(z)\right|\exp\left[i\varphi_{s,p}(z)\right]$ are the slowly varying complex amplitudes, $\alpha_{s,p}$ are the loss coefficients, $\Delta\beta = \beta_p - 2\beta_s$ is the phase mismatch, and $\kappa_{s,p}$ are the nonlinear coupling coefficients defined by

$$\kappa_s = \varepsilon_0 \iint \chi^{(2)} : \vec{E}_p \vec{E}_s^* \bullet \vec{E}_s' dxdy$$
$$\kappa_p = \varepsilon_0 \iint \chi^{(2)} : \vec{E}_s \vec{E}_s \bullet \vec{E}_p' dxdy \quad (4.16)$$

with $\vec{E}_{s,p}$ being the normalized mode profiles. In the calculation, the two photon absorption (TPA) process in silicon is neglected because most of the field is concentrated in the NP layers and TPA is a third order nonlinear process, being thus weaker than the second order nonlinear exploited process. The losses coming from the amorphous silicon materials, which can be reduced to less than 5 dB/cm in wire waveguides with current technology [216], are also neglected as the needed lengths are very short. The nonlinear coupling coefficient is calculated to be 60 $psm^{-1}W^{-1/2}$. The numerical results of OPA along propagation are displayed in Fig. 4.17 when the incident power $P_p(0)$ and phase $\varphi_p(0)$ of the PW are 1 W and 1.5π, and the incident power $P_s(0)$ and phase $\varphi_s(0)$ at the SW are 0.01 W and 0, respectively. It is shown that the SW is amplified to a peak power of 0.83 W at 168 μm of propagation length. After the peak point, the pumping gain is overcome by the loss and the SW begins to attenuate. Fig. 4.17(b) and (c) show the phase variations of SW and PW in the propagation, respectively. One can see that the phase of SW is unchanged and the phase of PW jumps to 0.5π at the peak position. This can be explained by the phase coupling equations, as derived in [139]. The initial phase of the SW and PW have an important influence on the OPA process. When the incident phase of SW is not zero, the phase changes while propagating until a stable value is obtained [139].

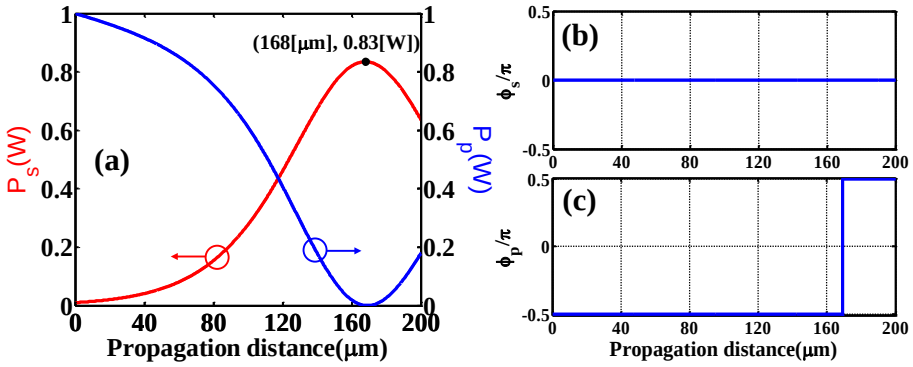

Fig. 4.17 Intensity and phase evolutions in the propagation when $\varphi_s(0) = 0$.

In the next, we analyze the OPA by tuning $\varphi_s(0)$, other conditions being unchanged as in Fig. 4.17. Fig. 4.18 shows the phase evolutions of SW and PW along the propagation for $\varphi_s(0) = 0.2\pi$ (a, b) and 0.8π (c, d), respectively. In these two cases, the amplitude evolutions are very similar to the one shown in Fig. 4.17(a) excepted that the distance to reach the SHG power maximum is 181 μm owing to smaller gain. It is shown that the phase at the SW is going to zero and π and stabilizes after 120 μm of propagation when $\varphi_s(0) = 0.2\pi$ and 0.8π, respectively.

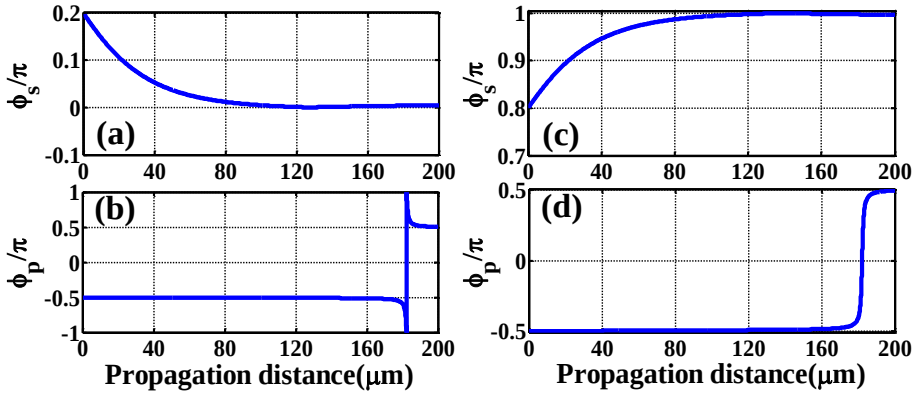

Fig. 4.18 Intensity and phase evolutions in the propagation when (a), (b), $\varphi_s(0) = 0.2\pi$; (c), (d), $\varphi_s(0) = 0.8\pi$.

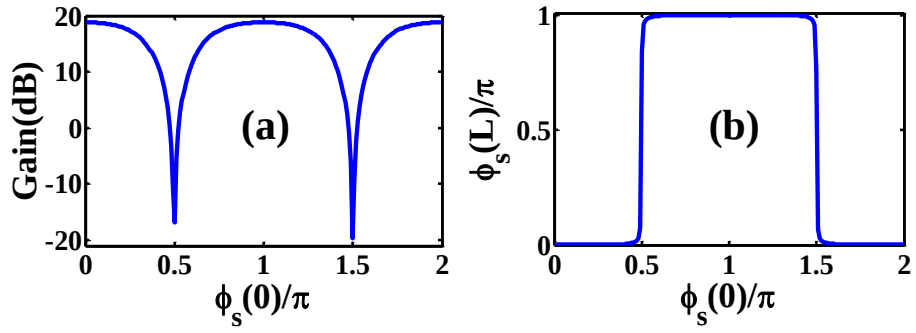

Fig. 4.19 Gain and output phase of SW versus the input phase of SW when L = 150 μm.

The length of the waveguide being now set to L = 150 μm, we plot in Fig. 4.19 the gain of OPA and output phase $\varphi_s(L)$ at the SW versus $\varphi_s(0)$. We can see that the gain changes with the incident phase. In some cases near the notch points, the gain even comes into negative values. More interestingly, if the incident phase at the SW is around π but not differing more than half π, the phase at the SW stabilizes to π. While the input

phase is around zero but not differing more than half π, it then stabilizes to zero, as can be seen in Fig. 4.19(b). This interesting effect is known as 'phase-squeezing' and was measured in the degenerate four-wave mixing phase-sensitive amplifiers based on nonlinear optical fibers [217].

4.3.3 Proposal for phase regeneration

Similarly as in [217], we propose to apply this mechanism to the phase recovery of PSK optical signals but in a highly integrated configuration making using of plasmonic waveguides. PSK optical signals result from a digital modulation scheme that conveys data by modulating the phase of a carrier wave, in which a finite number of phase responses under constant intensity are given. Unfortunately, along propagation, the phases usually deviate from their initial values due to amplitude noise and phase modulation effects. These deviations give rise to bit errors in detection, and should thus be removed by a regeneration mechanism [217]. Here, we assume a binary PSK signal with two phases of 0 and π, and the phase deviation of optical signal is smaller than 0.5π. When put the noised PSK optical signal through the nonlinear waveguide we propose, the phase will come back to the right value before detection.

The advantages of the phase recovery based on the OPA in SHPW lie in two aspects. On one hand, it can regenerate the phase in variable short distances (tolerant from 120 μm to 200 μm). On the other hand, the trip points and stable points are tunable with the control of $\varphi_p(0)$. $\varphi_s(L)$ jumps at $\varphi_s(0)=0.5\varphi_p(0)+0.75\pi$ and $\varphi_s(0)=0.5\varphi_p(0)-0.25\pi$ and stabilizes at $0.5\varphi_p(0)-0.75\pi$ and $0.5\varphi_p(0)+0.25\pi$. Besides, we could also find other applications based on this waveguide nonlinear effect such as phase-sensitive amplification and phase logic processing based on Fig. 4.19(a), which are also significant in all-optical signal processing. Additionally, it should be noted that the performance of the OPA and corresponding phase recovery in SHPW may be improved effectively by fulfilling the phase matching condition by an appropriate design of the geometrical parameters [143].

4.3.4 Conclusion

In conclusion, we propose a nonlinear SHPW and investigate the OPA process induced in this waveguide. Based on the special phase variation property in the OPA, we come up with a potential application in all-optical signal processing, which is phase recovery of PSK signals. The capability of recovery within short distances and tunability makes it promising and competitive in future highly-integrated nanophotonics.

4.4 Chapter summary

In this Chapter, we have investigated effective nonlinear processes in the hybrid plasmonic waveguides (HPW).

(1) We theoretically investigate the quadratic nonlinear property of a silicon-organic HPW with a thin polymer layer deposited on top of a silicon slab and covered by a metal cap. Due to the hybridization property of the waveguide modes, efficient phase-matched SHG from mid-infrared (~ 3.1 μm) to near-infrared wavelength (~ 1.55 μm) is achieved with small fabrication-error sensitivity (225 nm ≤ tolerated waveguide width ≤ 378 nm) and large bandwidth ($\Delta\lambda$ = 100 nm). The SHG yield is as large as 8.8% for a pumping power of 100 mW and waveguide length of 120 μm.

(2) Then, we propose to further enhance the SHG efficiency in the HPW by exploiting the resonant effect of the microring resonator configuration. By making the microring resonator doubly-resonant at the fundamental wavelength of 3.1 μm and second harmonic wavelength of 1.55 μm, the SHG efficiency is enhanced by almost two orders of magnitude when compared to the previous result induced in a straight HPW. A SHG efficiency of 13.71% is predicted for a low pump power of 20 mW in a ring with radius of 2.325 μm. This device provides a potential route for realizing efficient frequency conversion between mid-infrared and near-infrared wavebands on a chip.

(3) Phase regeneration of phase-shift keying signals is theoretically proposed for the first time based on the efficient optical parametric amplification (OPA) process in a highly-nonlinear symmetric HPW. This optimized stacked waveguide with nonlinear polymers has a relatively low loss of about 0.005 dB/μm and an effective nonlinear OPA coupling coefficient up to 60 ps/m/$W^{1/2}$. Phase recovery process was achieved in this waveguide within a length as short as 150 μm.

All these proposals and results illustrate that HPWs are capable of efficiently favoring nonlinear effects within short distances and low optical powers. Together with plasmonic slot waveguides investigated in Chapter 3, silicon plasmonic waveguides related nonlinear enhancement will play a key role in future photonic functionalities. However, this field is still in its young age. Most of the related works have been reported in the way of theoretical calculations, while very few experimental demonstrations have been proposed up to date. Thus, precise experimental fabrication and measurement of nonlinear silicon plasmonic waveguides are strongly expected in the next step of development. In the next chapter, we will present our progress in this regard.

Chapter 5

Progress towards experimental nonlinear plasmonic waveguides

In this chapter, we give all the experimental results that we have obtained by now on the way to demonstrate nonlinear plasmonic waveguides. Among all the integrated plasmonic waveguides, plasmonic slot waveguides (PSWs) have the simplest configuration. We have thus decided to choose them for experimental demonstrations. Firstly, let us briefly remind that various linear and nonlinear PSWs have been demonstrated. For example, Y. Fu et al. proposed all-optical logic gates based on the interference effect in PSW [85]. A. Kriesch et al. demonstrated subdiffraction directional couplers optically excited with high efficiency from free-space using optical Yagi-Uda style antennas at λ_0 = 1550 nm [86]. For nonlinear applications, the aforementioned plasmonic modulators realized by filling the slot of PSW with EO polymers are very compact and able to operate ultra-high speed RF signals [40-44].

In the next sections of this chapter, we will detail the whole adopted process for the PSW demonstration, including the design of their dimensions and in/out tapers for efficient light coupling, the detailed fabrication procedures and optical measurement. The measured results indicate that the fabricated PSWs have good performance in terms of coupling and optical losses. As shown hereafter, a 0.5 dB/μm propagation loss level is experimentally reported at λ = 1.55 μm for a PSW with cross-sectional dimension of 66 nm × 150 nm, for which the theoretical propagation loss is 0.434 dB/μm, meaning an agreement of both levels with a moderate error range of 10.6%.

5.1 Design and optimization of waveguides and coupling tapers

Our final goal is to experimentally demonstrate the high-speed optical detector

proposed in Section 3.3. Due to the undesired ease of oxidation of silver in air, gold has been considered as the plasmonic material in experiments though it has larger absorption loss than silver. The polymer we used in experiments is the M1 EO polymer, which is commercially available from the GIGOPTIX company [218] and has been demonstrated as an effective EO polymer (n = 1.67, r_{33} = 70 pm/V) [219]. Excepted these two differences related to the material choices, the investigated PSW geometry has the same structure as the one proposed in Section 3.3.

Fig. 5.1 shows the schematics of the plasmonic slot waveguide (PSW) and taper couplers that bridge PSW with the in and out silicon waveguides. The whole structure is placed on a silica substrate, and the background top cladding medium material is the M1 polymer. The width and height of the incoming silicon waveguides are w_{Si} = 450 nm and h_{Si} = 220 nm, respectively. The angle and tip width of the taper coupler are defined as θ and d, respectively. The distance between the taper tip and PSW is l.

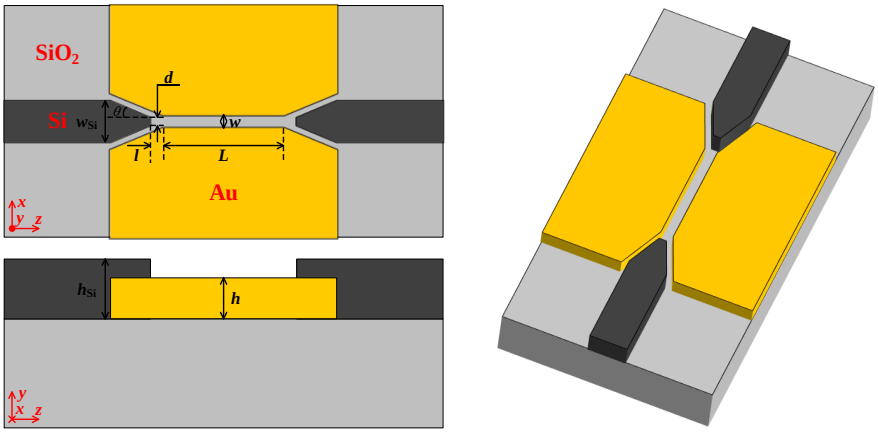

Fig. 5.1 Schematics of the plasmonic slot waveguide and taper couplers that bridge the PSW with silicon strip waveguides.

In a first step, we have designed the geometrical size of the PSW with new material choices for effective generation of electrical signals, ease of fabrication and efficient light coupling. In view of the fabrication tolerance and acceptable loss level, the width of the PSW is first set to w = 100 nm. Then, the height and length of the PSW have been designed by applying a similar optimization process as the one described in

Section 3.3. The related results are shown in Fig. 5.2 and 5.3, from which we can see that the height and length optimizing the normalized optical rectification efficiency are ~140 nm and 8.8 μm, respectively. Thus, w = 100 nm, h = 150 nm and L = 8.8 μm have been firmly chosen. For this PSW configuration, the calculated voltage and current responsivities are 0.2365 V/W and 0.0308 mA/W, respectively. Let us remark that smaller size PSWs may support larger responsivities, while the fabrication and coupling issues would become harder as well.

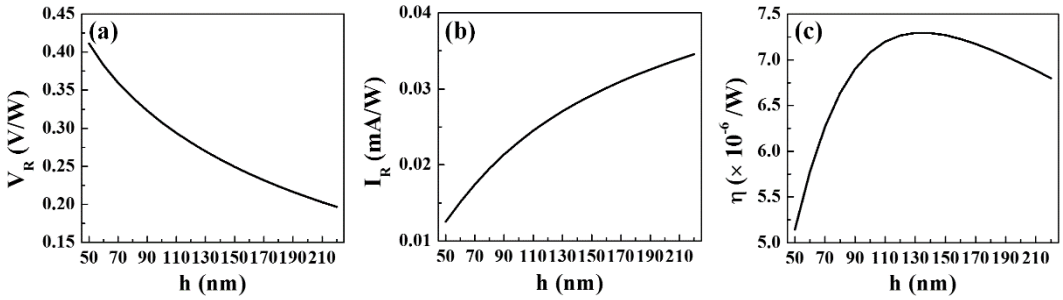

Fig. 5.2 (a) Voltage responsivity, (b) Current responsivity and (c) Normalized efficiency of the optical rectification process in the PSW with 5dB length (where the transmission of the optical mode is -5 dB) as a function of the slot height for a fixed width of w = 100 nm. The metal and the polymer are chosen as gold and M1 polymer, respectively.

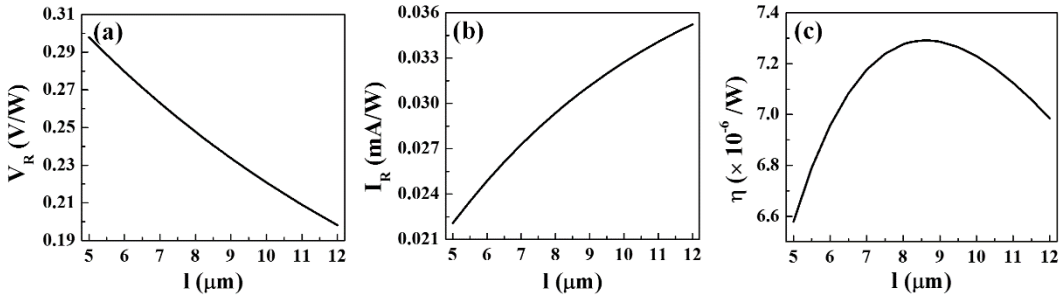

Fig. 5.3 (a) Voltage responsivity, (b) current responsivity and (c) the normalized efficiency of the optical rectification process in the PSW as a function of the waveguide length for fixed slot width w = 100 nm and height h = 150 nm.

The next critical issue is how to efficiently couple light into such a PSW. Many structures have been proposed to do this, such as tapered silicon strip waveguide [40, 42, 72, 220], vertical directional coupling between a silicon strip waveguide and a PSW [221, 222], nanoantenna couplers [86, 223] and metallic gratings [85]. Among these

structures, tapered silicon strip waveguides have properties of high efficiency and broadband coupling. For example, in Ref. [220] J. Tian et al. proposed a theoretical coupling efficiencies up to 88% for a wide wavelength range extended from 1460 nm to 1540 nm by tuning the geometrical parameters and experimentally demonstrated a 35% coupling efficiency. More importantly, this coupling scheme provides a good way to bridge the size gap between conventional microscopic silicon photonics and nanoplasmonics, which is a key point for future plasmonic planar integrated optics. For these reasons, we have chosen to use this coupling principle. By sweeping the geometrical parameters (i.e. d, l and θ) in a series of 3D-FDTD simulations, we have obtained an optimized taper size. In the simulation, an override mesh region with mesh size of $dx = dy = dz = 5$ nm has been added in the metal, slot and taper regions.

Note that in the next whole optimization process, we have fixed the following PSW dimensions: $w = 100$ nm, $h = 150$ nm and $L = 5$ μm and considered an operating wavelength of $\lambda = 1550$ nm. First, we set the taper as $l = 500$ nm and $\theta = 8°$ and swept d, or set the taper as $d = 80$ nm and $\theta = 8°$ and swept l. Results are shown in Fig. 5.4(a) and (b), respectively. As it can be seen, the transmittance T increases when increasing d or when decreasing l. However, one can notice that the width between the silicon taper and metallic slabs becomes very small for too large d values or too small l ones, which makes the fabrication difficult. So we have chosen the following parameters in experiments: $d = 80$ nm and $l = 500$ nm.

Fig. 5.4(c) shows the obtained results for different θ values with fixed $d = 80$ nm and $l = 500$ nm. There exists an optimized value around 8 degrees. Therefore, the final geometry of the taper coupler is designed as $d = 80$ nm, $l = 500$ nm and $\theta = 8°$, for which the total transmittance is $T = 0.301445$ (-5.208 dB) for the PSW length of $L = 5$ μm. The total transmission can be expressed as $T = t^2\exp(-\alpha L)$ where t is the coupling efficiency for a single taper and α is the attenuation coefficient for the slot mode. For the PSW with $w = 100$ nm and $h = 150$ nm, the effective mode index is calculated to be $n_{eff} = 1.957911+0.01823654i$ at $\lambda = 1550$ nm, then $\alpha = 73925$ rad/m. By substituting

this into the total transmittance expression, we get the coupling efficiency of a single taper coupler to be t = 0.6605 (-1.80133 dB).

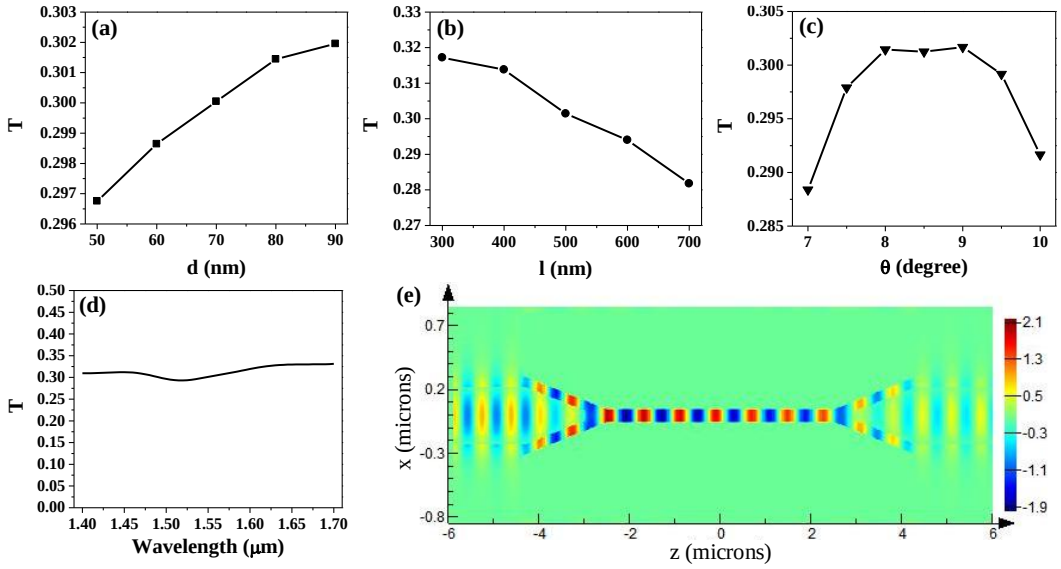

Fig. 5.4 Transmittance of the plasmonic slot waveguide with two taper couplers at λ = 1550 nm as a function of the (a) taper tip width d when l = 500 nm and θ = 8°, (b) gap between the taper and slot l when d = 80 nm and θ = 8°, and (c) taper angle θ when d = 80 nm and l = 500 nm. Other geometrical parameters are set as w_{Si} = 450 nm, h_{Si} = 220 nm, w = 100 nm, h = 150 nm and L = 5 μm. (d) Transmittance as a function of the optical wavelength and (e) electric field component E_x distribution along the propagation when d = 80 nm, l = 500 nm and θ = 8°. All results are obtained by using the software FDTD Lumerical with 3D simulations.

We then investigate the broadband property of the taper coupler and plot the result in Fig. 5.4(d). The taper coupler supports a flat transmission from a wide waveband extended from 1.4 μm to 1.7 μm. Fig. 5.4(e) shows the electric field component E_x distribution along the propagation for the optimized taper geometry. The cross section is located at the middle of the metal. It can be seen that the plasmonic mode in the slot is effectively excited between two tapers.

The excitation of the TE mode in the standard silicon strip waveguide is realized by a conventional grating coupler from a tapered lens fiber. The period, duty cycle and

etching depth of the grating are chosen to be 630 nm, 1:1 and 70 nm, respectively. The typical coupling efficiency of this grating coupler is -5.1 dB [224].

5.2 Fabrication

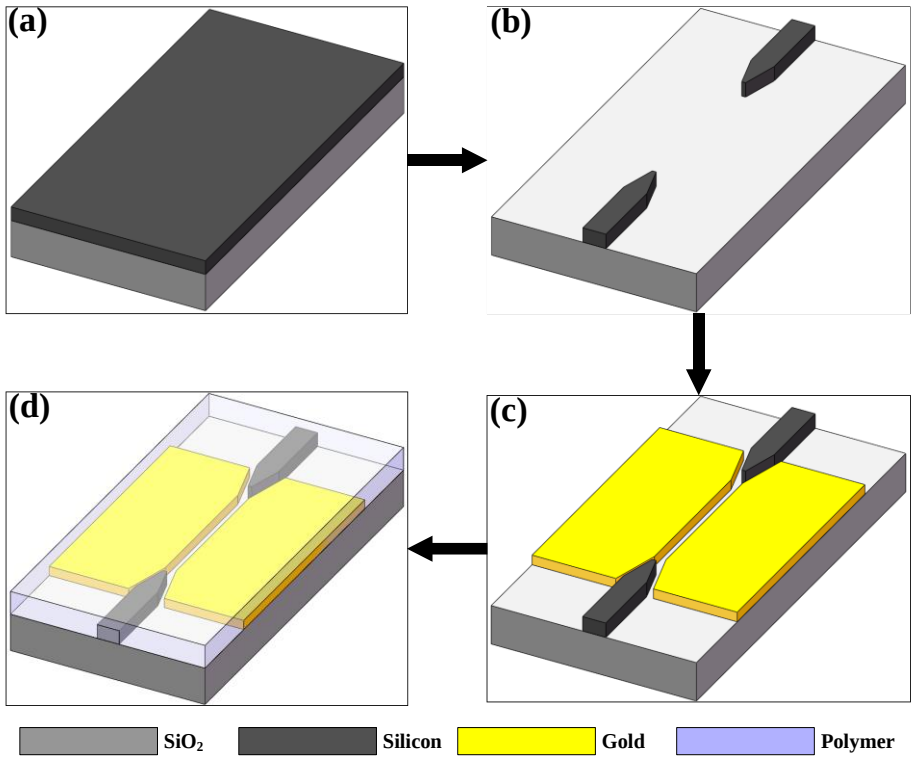

Fig. 5.5 Fabrication procedures of the nonlinear plasmonic slot waveguide.

In view of the possible fabrication errors, we have designed PSWs with different widths. PSWs are fabricated in a four-step process with standard nanofabrication techniques. For the first step, gold markers were deposited onto a SOI wafer with a 220 nm silicon top layer and 3 μm buried oxide layer for the next alignment between different steps. Specifically, the pattern was defined by using electron beam lithography (EBL) with PMMA as the electron beam resist. After development, 10 nm of titanium and 70 nm of gold were successively deposited onto the wafer by an electron beam evaporation (EBE) system. Then a lift-off process was performed in the acetone to obtain the gold markers. Second, as shown in Fig. 5.5(b), silicon strip waveguides with the taper and grating couplers were defined by EBL with ZEP520 as the e-beam resist. The pattern was then transferred to the silicon layer by inductively coupled plasma reactive ion

etching (ICPRIE), resulting in the silicon parts. Third, the metallic slot waveguide was fabricated by another lift-off process with ZEP520 as the e-beam resist. 3nm-thick chromium and 150nm-thick gold layers were evaporated onto the wafer by EBE. The wafer after this procedure is shown in Fig. 5.5(c). Fourth, the M1 polymer was spin-coated onto the wafer. The schematic of the final device is shown in Fig. 5.5(d).

Fig. 5.6(a) and (b) show the optical microscope pictures of the structure after the second and third steps, respectively. The inserted pictures are the partially enlarged displays around the PSW part. Note that the stains in the enlarged pictures are located on the high magnification lens of the object, while the wafer is clear. To have a more detailed view of the fabricated waveguide, we used the scanning electron microscopy (SEM) system and we give the related pictures in Figs. 5.7-5.10.

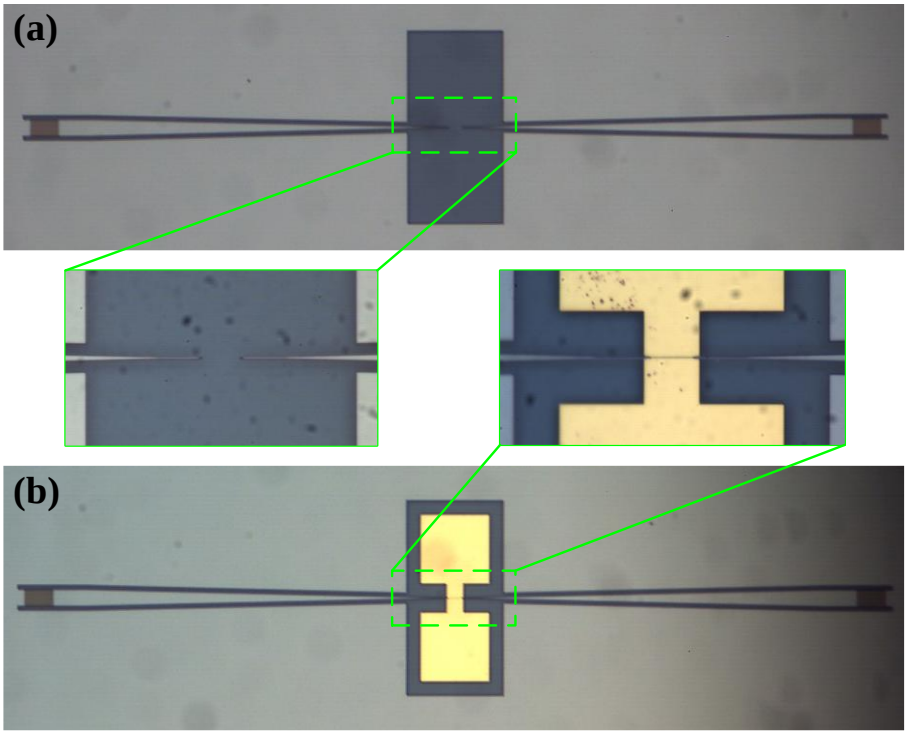

Fig. 5.6 Metallographic microscope pictures after the (a) second (b) third fabrication step.

Fig. 5.7 shows the reference silicon strip waveguide and grating couplers. The width of the fabricated waveguide is ~412 nm, while the designed width in the L-edit layout was 450 nm. This means that fabrication error around 38 nm exists in this fabrication. Fig. 5.8 shows the SEM pictures of the PSW and taper couplers from silicon

strip waveguide. It is clear that the PSW and silicon strip waveguide have a good alignment between each other and pretty smooth sidewalls. We will see in the next section that the fabricated PSW have similar loss level compared with the theoretical value, which further confirms this last point.

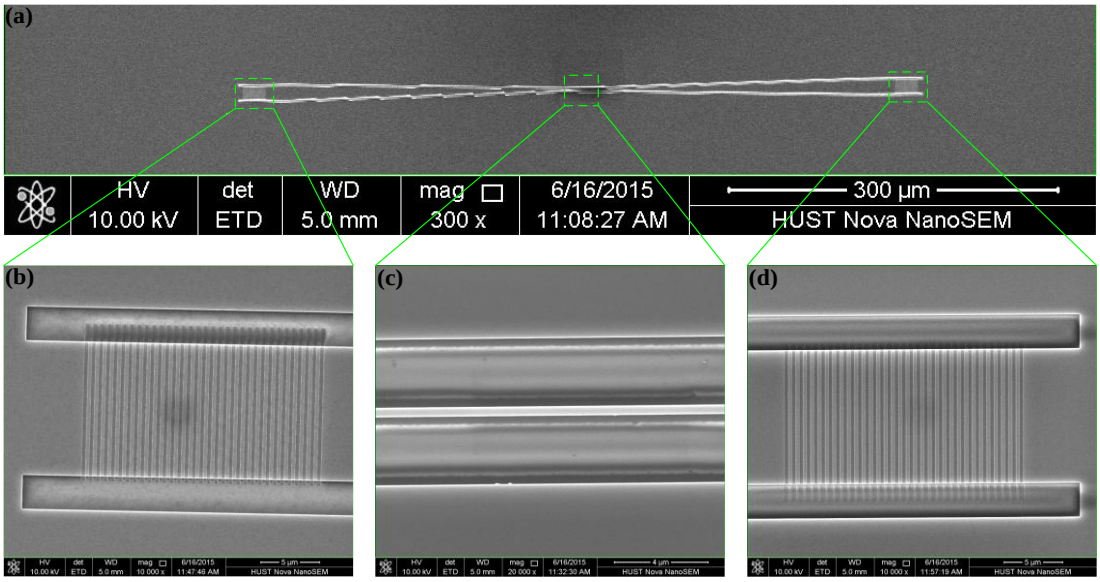

Fig. 5.7 SEM pictures of silicon stripe waveguide and grating couplers before coating the polymer.

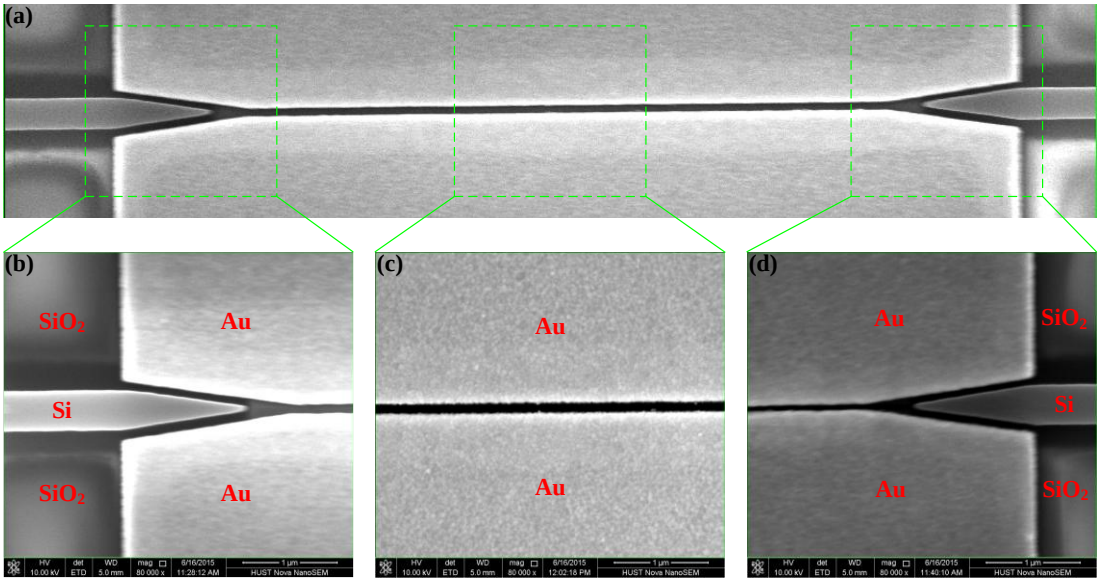

Fig. 5.8 SEM pictures of the fabricated plasmonic slot waveguide and taper couplers before coating the polymer.

Fig.5.9 shows the obtained PSWs for different widths. We have designed PSWs with three different widths of 100 nm, 120 nm and 140 nm. Correspondingly, the fabricated widths are measured to be 65.6 nm, 76.5 nm and 109.3 nm, respectively. This means that the fabricated PSW also have errors around 40 nm, which is an important guideline for future design. Fig. 5.10 shows the PSW with different lengths of (a) 8.8μm and (b) 20μm.

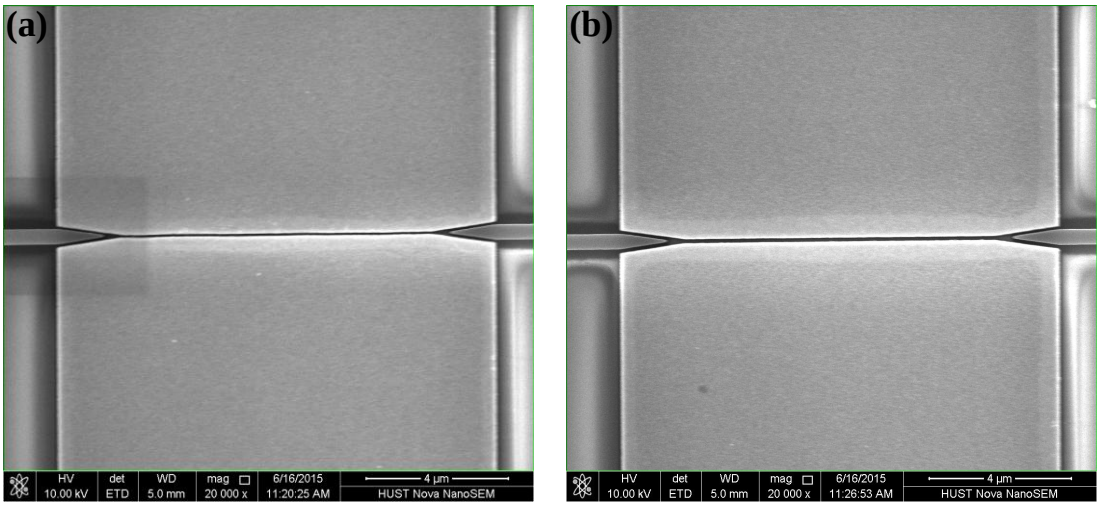

Fig. 5.9 SEM pictures of fabricated plasmonic slot waveguides with different widths before coating the polymer.

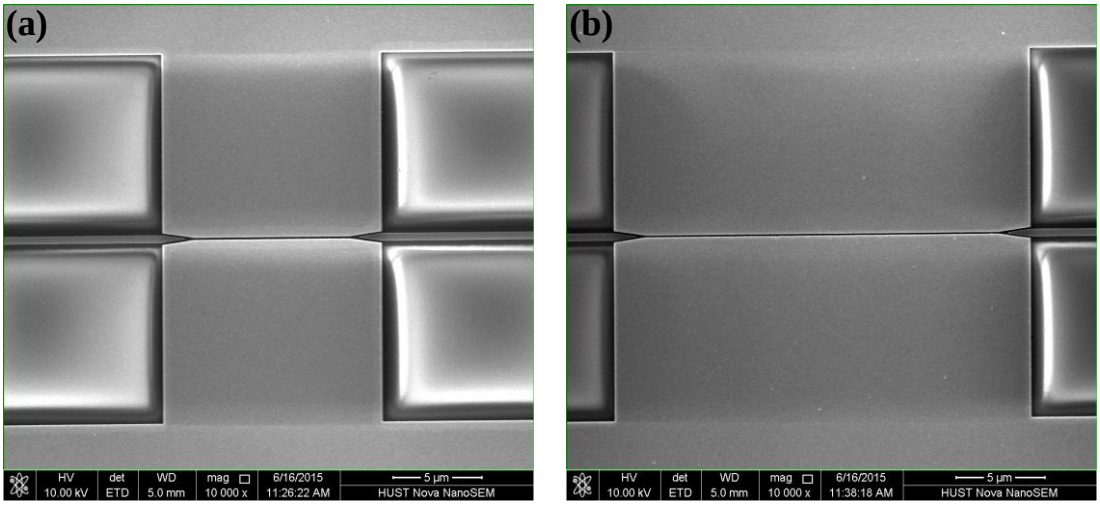

Fig. 5.10 SEM pictures of fabricated plasmonic slot waveguides with different lengths before coating the polymer.

All these pictures were taken before spin-coating the M1 polymer. After the first

measurement of PSWs with air cladding, the polymer was then spin-coated onto the wafer. Using the coating parameters of 500 rpm for 5 seconds and 700 rpm for 40 seconds, a polymer layer with thickness of 2.21 μm was spin-coated onto the wafer. After coating, the film was first oven dried by ramping the temperature from ambient to 50 ℃ at heating rate of 10 ℃/min and held for 2 hours at 50 ℃. Then the film was further dried at 50 ℃ under vacuum (~ 10 Pa) for 12 hours. After this, the polymer was ready for poling.

5.3 Measurement and results

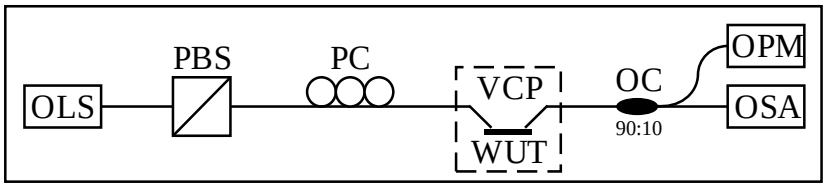

OLS: Optical light source
PBS: Polarization beam splitter
PC: Polarization controller
VCP: Vertical coupling platform
WUT: Wafer under test
OC: Optical coupler
OPM: Optical power meter
OSA: Optical spectrum analyzer

Fig. 5.11 Experimental setup to measure the fabricated waveguides.

After fabrication, we measured the PSW with a vertical coupling system. The measurement setup is shown in Fig. 5.11. Firstly, we measured the PSW without coating the polymer. To determine the losses of the plasmonic sections, PSW with lengths of 8.8 μm, 10 μm and 20 μm were tested. Fig. 5.12(a) plots the loss of the PSW section as a function of the wavelength for w = 65.6 nm and different waveguide lengths. When we focused the propagation property at λ = 1550 nm, loss of 0.5 dB/μm were found for the PSW with w = 65.6 nm. The 8.8 μm, 10 μm and 20 μm long plasmonic sections contributed at the levels of 11.439 dB, 11.877 dB and 17.067 dB to the total losses, respectively. The main contribution to the fiber-to-fiber losses were from the grating couplers, contributing to 12.237 dB of loss for each waveguide. Losses in the feeding silicon strip waveguide and photonic-plasmonic taper couplers added another 7 dB. The high losses of photonic-plasmonic taper couplers were due to the fact that

the above optimized process in the design part was performed for the configuration with a polymer top cladding instead of an air top cladding, as here.

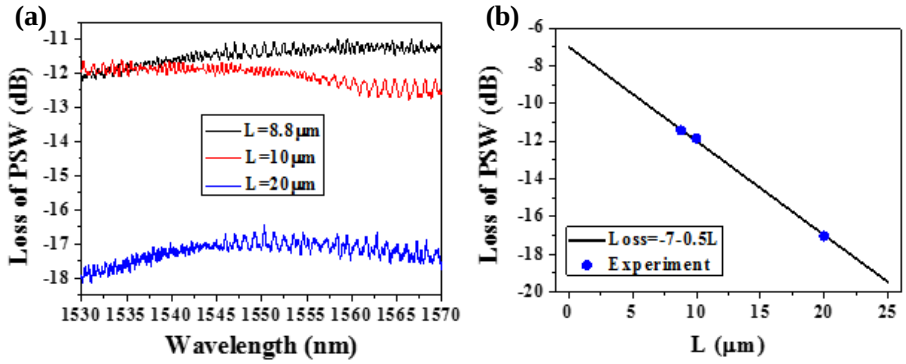

Fig. 5.12 (a) Experimental measured loss of PSW with width of 65.6 nm and different waveguide length as a function of wavelength. (b) Loss of PSW at λ = 1550 nm as a function of the waveguide length. A linear slope indicates taper loss of 7 dB and PSW propagation losses of 0.5 dB/μm.

We recalculated the PSW mode with w = 65.6 nm and h = 150 nm by using COMSOL and got an effective mode index of n_{eff} = 1.43491+0.01233i. The corresponding loss is α = 0.434 dB/μm, which is near to the measured value of 0.5 dB/μm. The additional scattering loss from the roughness of sidewall is thus estimated to be 0.066 dB/μm. Another source of this difference comes from the 3 nm chromium adhere layer, which was omitted in the mode calculation.

This whole loss may seem to be very large when compared with the one in dielectric waveguides, which can be less than 1 dB/cm in silicon waveguides. However, as mentioned in Chapter 2, one of the advantages of plasmonic waveguides lies in realizing desired function within very short lengths (typically no more than several propagation distances). Thus, the whole losses in plasmonic devices can still be low. A good example is the recently proposed all-plasmonic Mach-Zehnder modulator [44], in which the insertion loss is 8 ± 1 dB due to a short length of 10 μm. This is not too far away from well-engineered high-speed silicon modulators reporting insertion losses of 4–7 dB with smaller bandwidths.

Then, we cover the wafer with the M1 polymer. Using the spin-coating parameter of 500 rpm for 5 seconds and 700 rpm for 40 seconds, a polymer film with thickness of 2.21 μm and good homogeneity is coated onto the wafer. The PSW with polymer cladding is tested with the same setup shown in Fig. 5.11. The results and comparison with air cladding can be seen in Table 5.1. All the values are taken at λ = 1550 nm. We can see that the loss level of the PSW with polymer cladding is similar to the one with air cladding, which means that the loss from the polymer absorption is small. Interestingly, contrary to the air cladding, the PSW with polymer cladding has smaller losses for larger widths. For the width of w = 109.3 nm and length of L = 8.8 μm, the loss contribution from the PSW section is only around 8.785 dB. This matter of fact can be explained as follows. In the optimization design of the taper couplers, the width of the PSW was taken as w = 100 nm. As a result, the closer to 100 nm the width is, the lower the loss.

Cladding	***L* (μm)**	***w* (nm)**	**PSW loss (dB)**
Air	8.8	65.6	11.439
Air	8.8	76.5	12.933
Air	8.8	109.3	15.741
Air	10	65.6	11.877
Air	10	76.5	13.815
Air	10	109.3	17.81
Polymer	8.8	65.6	12.89
Polymer	8.8	76.5	11.917
Polymer	8.8	109.3	9.206
Polymer	10	65.6	13.993
Polymer	10	76.5	12.82
Polymer	10	109.3	11.88

Table 5.1 Measured loss of PSWs for different cladding materials and sizes at λ = 1550 nm

In order to investigate the nonlinear optical rectification effect in the nonlinear PSW, we need to pole the polymer with proper poling condition. According to the datasheet of the M1 polymer, the poling condition we have applied is shown in Fig.

5.13. Firstly, the temperature of the sample was heated from ambient to the polymer transition temperature of 140 ℃ with a ramping rate of 10 ℃/min. Then the temperature was maintained and a voltage was applied between the two metallic slabs with two electrode probes. The voltage was increased gradually until the electrical field in the slot reached 110 V/μm. The voltage and temperature were kept for 5 seconds. After poling, the poling voltage (used at poling temperature) was maintaind for 3 minutes and the temperature of the sample dropt off to the ambient. In the end, the voltage was taken out.

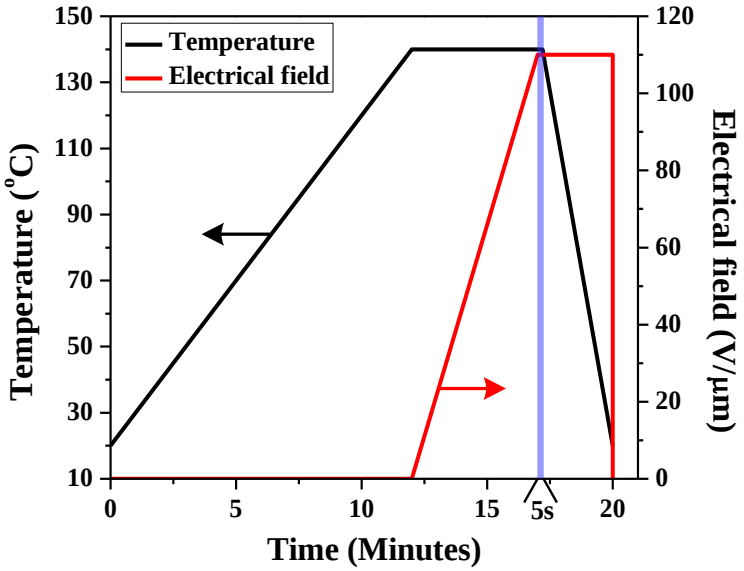

Fig. 5.13 Poling condition of the M1 polymer.

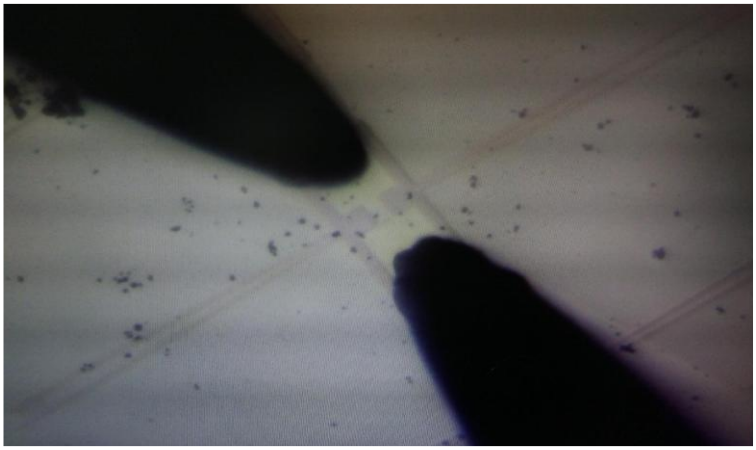

Fig. 14 Diagram of the electrodes contact for the plasmonic slot waveguide in the poling process and measurement. The two black tips are the probes.

Note that in the whole poling process, a poling chamber purging with nitrogen continuously is needed to extrude air. Since this poling condition is not so easy to achieve, our experiment gets stuck in this step at present. Right now, we are trying to solve this difficult point. The electrical contact between electrodes of the PSW and outside in the poling process and future measurement are realized by impaling the nonconducting polymer layer with two probe tips. Fig. 5.14 shows the microscope pictures.

In the future, after solving the poling problem of polymer, we will begin to test the nonlinear property of the fabricated PSW.

5.4 Chapter summary

To conclude this chapter, we have experientally demonstrated PSWs fabricated in our clean room. The plasmonic modes in fabricated PSWs are successifully excited with a tapered silicon strip waveguide configuration. The measured linear losses are near to the theoretical ones, indicating a good performance of the PSW. After spin-coating the EO polymer M1 onto the wafer, the PSWs kept this good performance.

Beyond the linear propagation properties, we now aim at demonstrating the nonlinear response of the fabricated PSWs. At present, we are on the step to efficiently pole the polymer. In the next step, our goal is to demonstrate the optical rectification effect in the PSW and finally apply it to compact high-speed detectors. Meanwhile, the performance of our experimental configuration can be improved in terms of grating couplers and active nonlinear materials. For example, D. Benedikovic et al. recently proposed a grating coupler with a coupling efficiency of -1.3 dB [225].

Chapter 6

Conclusion and future steps

With further increase of bandwidth demand and integration density, the expectations for new integrated devices include ultra-compact size, ultrahigh speed, low cost and low power consumption. However, the conventional integrated electronic and dielectric photonic devices can hardly satisfy all these demands. In recent years, plasmonics has come into being a promising platform to meet some of these requirements due to its ability to confine the optical and electrical modes beyond the diffraction limit, support ultrafast response time down to femtosecond scale and merge photonics and electronics at nanoscale dimensions.

The strong confinement and enhancement of electromagnetic fields in plasmonic structures makes them very ideal for nonlinear applications. The nonlinear plasmonic devices based on free space beams have been investigated extensively, while the research dedicated to their integrated nonlinear plasmonic counterparts has just come in a pretty early phase.

In this dissertation, under the foundation of a joint PhD program between the Paris-Sud University (Orsay/France, supervisor: Eric Cassan) and the Huazhong University of Science and Technology (Wuhan/China, supervisor: Xinliang Zhang), I have conducted a series of theoretical and experimental research dedicated to plasmonic based integrated nonlinear devices and related optical signal processing. The research achievements and contributions in the full text can be summed up in the following respects:

(1) A theoretical model of nonlinear coupled-wave equations (NCE) was derived in detail. The proposed NCE can be used to analyze various nonlinear effects in lossy plasmonic waveguides. Then, based on the NCE, four key factors to enhance the nonlinear effects were presented to guide the design of high-performance nonlinear

integrated devices. A conclusion that plasmonic waveguides can support intense nonlinear effects in short distance was obtained.

(2) Efficient second harmonic generation (SHG) from 1550 nm to 775 nm in plasmonic slot waveguides (PSW) was theoretically investigated. The needed phase matching condition was satisfied through the modal phase-matching method by an appropriate design of the waveguide opto-geometrical parameters. The SHG signal generated in the starting waveguide is three orders of magnitude higher than those previously reported. Then, the SHG performance was further improved by increasing the refraction index asymmetry of the structure. The obtained device length is shorter than 20 μm and the normalized SHG conversion efficiency comes up to more than 1×10^5 $W^{-1}cm^{-2}$.

(3) The possible realization of an active electro-optical control of the nonlinear SHG mechanism in a PSW was theoretically investigated. Both the conventional SHG and the electrically induced SHG were taken into account with a moderate pump power of 40 mW at the fundamental wavelength of 1550 nm. The generated power of the second harmonic wave can be modulated by the applied voltage in a quadratic and almost linear forms for centro-symmetric and noncentro-symmetric nonlinear polymers integrated in the slot, respectively. Converted power up to 140 μW within a short distance of only 16 μm was predicted for a voltage of 10 V. This mechanism may open a new route to realize high-speed advanced modulations or inversely to detect ultrafast electrical signals.

(4) The nonlinear optical rectification (OR) process induced in a PSW with an electro-optic polymer infiltrated into the slot was investigated. An electrical signal was generated between the two metal slabs when an intensity-modulated optical signal was injected into the PSW. Optimization of the geometrical parameters was performed to obtain the highest OR efficiency. Specifically, a voltage responsivity over 1V/W and a normalized OR efficiency of 2.25×10^{-4} W^{-1} were predicted in a compact PSW with active size of 50nm×90nm×22.4μm for a modulation speed of

400 GHz. The OR efficiency is further increased when introducing the electrically induced OR contribution. The OR is characterized by a relatively flat response for a wide range of optical wavelengths from 1.25 μm to 1.7 μm and supports a RF cut-off frequency up to 800 GHz. This efficient OR process paves a new way for realization of high-speed broadband optical detection and demodulation schemes in silicon chips.

(5) Efficient SHG from mid-infrared (~ 3.1 μm) to near-infrared wavelength (~ 1.55 μm) in the hybrid plasmonic waveguide (HPW) was theoretically investigated. Due to the hybridization property of the waveguide modes, efficient phase-matched SHG is achieved with small fabrication-error sensitivity (225 nm < tolerated waveguide width < 378 nm) and large bandwidth (~ 100 nm). The SHG yield is as large as 8.8% for a pumping power of 100 mW and waveguide length of 120 μm. Then the SHG efficiency was further improved by two orders of magnitudes by exploiting the resonant effect of the microring resonator configuration. By making the microring resonator doubly-resonant at the fundamental wavelength of 3.1μm and second harmonic wavelength of 1.55μm, a SHG efficiency of 13.71% is predicted for a low pump power of 20 mW in a ring with radius of 2.325 μm. This device provides a potential route for realizing efficient frequency conversion between mid-infrared and near-infrared wavebands on a chip.

(6) Phase regeneration of phase-shift keying signals is theoretically proposed for the first time based on the efficient optical parametric amplification (OPA) process in a highly-nonlinear symmetric HPW. This optimized stacked waveguide with nonlinear organic materials has a relatively low loss of about 0.005 dB/μm and an effective nonlinear OPA coupling coefficient up to 60 $psm^{-1}W^{-1/2}$. Phase recovery process was achieved in this waveguide within a length as short as 150 μm.

(7) Plasmonic slot waveguides were experimentally fabricated. Firstly, the optimized dimensions of PSWs and the taper couplers between the classical dielectric silicon

strip waveguides and the PSWs were obtained through numerical simulations. Then, the fabrication steps were introduced. The measured results indicate that the fabricated PSW with size of 66 nm × 150 nm has loss of 0.5 dB/μm, which is near to the theoretical level. Then, the PSWs were spin-coated with EO polymer M1 as the first step to demonstrate the OR effect.

All the above research indicate that silicon plasmonic waveguides open promising solutions to enhance nonlinear effects within short distance while managing the loss issue at an acceptable level, which has great potential for the realization of ultra-compact and low power integrated functionalities such as wavelength converters, logical gates, modulators/switches and detectors.

In the same time, the high-quality fabrication and measurement of compact plasmonic waveguides, especially nonlinear plasmonic waveguides, remains a challenge when compared with dielectric photonic waveguides. At present, we have successfully spin-coated the EO polymer onto the PSW wafer. Future steps of our work include:

(1) Poling the EO polymer. This is a difficult point due to the needed harsh poling environment.

(2) Measuring the OR effect after poling in the PSW.

In conclusion, CMOS-compatible plasmonic waveguides are widely considered as a prospective basic element to implement future on-chip subwavelength electronic–photonic integrated circuits. In the future, plasmonic on-chip electronic-photonic integrated circuits and chip-to-chip interconnects are likely to be able to combine optical sources, interconnects, modulators, and detectors on the same chip, within subdiffraction-limited dimensions [226-228]. Such an integrated photonic technology could revolutionize the bandwidth, speed, size, cost, and power requirements of modern computational networks, enabling more efficient solutions to increasingly complex problems. As soon as we can overcome the high loss bottleneck, a new plasmonic

revolution may begin. Actually, for this biggest challenge in the field of plasmonics, researchers have managed to figure out some potential methods to deal with the optical losses in metallic systems [50]. For example, many new plasmonic materials beyond gold and silver have been proposed [48, 229, 230]. Or in another way, the field of integrated computation devices in the foreseeable future is to effectively utilize the potential of the three available technologies (electronics, photonics, and plasmonics) so that they may compensate the weaknesses of each other, i.e. the losses in plasmonics with photonics, the size of photonics with plasmonics, and the interface to the outside world with electronics [231].

Appendix

Numerical method to analyze nonlinear effects

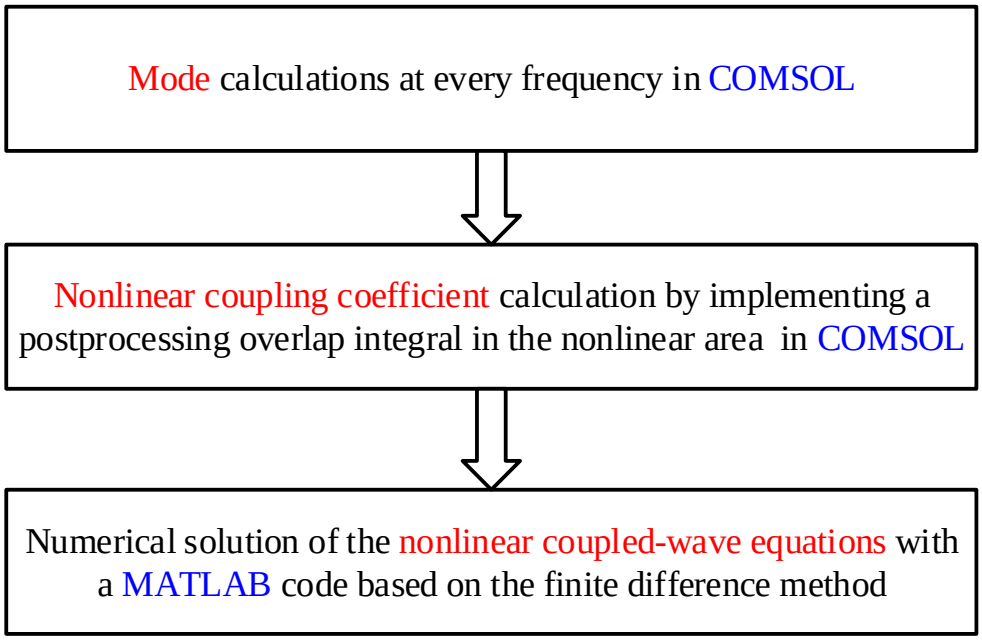

Fig. A1 Flow chart of the numerical method to analyze different kinds of nonlinear effects in an integrated waveguide.

All the simulations proposed in this dissertation to analyze various nonlinear effects induced in an integrated waveguide have been based on a numerical processing as shown in Fig. A1. In the first step, we calculate the mode profiles at every frequency of the related nonlinear effect by using the finite-element-based commercial software COMSOL. Then, the nonlinear coupling coefficient as expressed in Eq. (2.13) is calculated through a postprocessing of "*Derived Values* → *Integration* → *Surface Integration*" in the nonlinear area of the waveguide cross-section in COMSOL. After this, we can substitute this obtained nonlinear coupling coefficient into the nonlinear coupled-wave equation and finally solve it with a self-made MATLAB code based on the finite difference method.

The following is the typical code to obtain the result in Fig. 3.6 for analyzing the second harmonic generation process in the plasmonic slot waveguide.

```
%Code to calculate the second harmonic generation
clc
clear
L=100e-6;                       %Length of the waveguide, unit: m
dz=1e-8;                        %Resolution of the calculation, unit: m
z=(0:dz:L);
alpha1=29068;                   %Loss coefficient of the FF mode, unit: 1/m
alpha2=46839;                   %Loss coefficient of the SH mode, unit: 1/m
kappa1=2.92e-10;                %Nonlinear coupling coefficient at FF, unit:
                                 s/m/sqrt(W)
kappa2=conj(kappa1);            %Nonlinear coupling coefficient at FF, unit:
                                 s/m/sqrt(W)
dbeta=0;                        %Phase mismatching
omega=(2*pi*3e8/1.55e-6);       %Angular frequency of the FF

P1_in=1;                        %Input pump power of FF, unit: W
A1_in=sqrt(P1_in);
P2_in=0;                        %Input power of SH, unit: W
A2_in=sqrt(P2_in);
phi1_0=0;
phi2_0=0;

A1=A1_in*exp(i*phi1_0);  AA1=[A1];
A2=A2_in*exp(i*phi2_0);  AA2=[A2];
%Calculate the nonlinear coupled-wave equation with finite difference method
    for m=1:length(z)-1
        A1=A1+dz*(-alpha1*A1...
            +i*0.25*omega*kappa1*conj(A1)*A2*exp(i*(dbeta)*z(m)));
        AA1=[AA1; A1];
        A2=A2+dz*(-alpha2*A2...
            +i*0.25*omega*kappa2*A1^2*exp(-i*(dbeta)*z(m)));
        AA2=[AA2; A2];
    end
P1=abs(AA1).^2;
P2=abs(AA2).^2;
P2_max=max(P2);                  %Peak efficiency
z_max=z(find(P2==P2_max))*1e6;   %Peak position, unit:um

%Plot the result
[ax,h1,h2]=plotyy(z*1e6,abs(AA1).^2,z*1e6,abs(AA2).^2);
    set(ax(1),'ylim',[0 P1_in],'ytick',[0:P1_in/5:P1_in]);
    set(ax(2),'ylim',[0 P1_in/4],'ytick',[0:P1_in/4/5:P1_in/4]);
    set(ax(1),'ycolor','k');
```

```
    set(ax(2),'ycolor','k');
    set(ax(1),'linewidth',2.5);
    set(ax(2),'linewidth',2.5);
    set(ax(1),'xlim',[0 L*1e6],'xtick',[0:20:L*1e6]);
    set(ax(2),'xlim',[0,L*1e6],'xtick',[0:20:L*1e6]);
    set(ax(1),'fontsize',30,'fontname','Times New Roman',
              'FontWeight','Bold');
    set(ax(2),'fontsize',30,'fontname','Times New Roman',
              'FontWeight','Bold');
    set(h1,'color', 'r','linewidth',4);
    set(h2,'color', 'b','linewidth',4, 'linestyle', '--');
    hh1=get(ax(1),'ylabel');
    set(hh1,'string','P_F_F(W)');
    set(hh1,'fontsize',30,'fontname','Times New Roman',
            'FontWeight','Bold','color','r');
    hh2=get(ax(2),'ylabel');
    set(hh2,'string','P_S_H(W)');
    set(hh2,'fontsize',30,'fontname','Times New Roman',
            'FontWeight','Bold','color','b','rotation',270);
    xlabel('Propagation distance(\mum)');
hold on;
plot(z_max,P2_max*4,'k.','MarkerSize',30);
mm=['(',num2str(z_max),'[\mum], ',num2str(P2_max),'[W])'];
text(z_max-8,P2_max*4+0.1,mm,'fontname','Times New Roman',
                             'fontsize',25,'fontweight','bold');
```

Bibliography

1. R. G. H. van Uden, R. A. Correa, E. A. Lopez, F. M. Huijskens, C. Xia, G. Li, A. Schülzgen, H. de Waardt, A. M. J. Koonen, and C. M. Okonkwo, "Ultra-high-density spatial division multiplexing with a few-mode multicore fibre," Nat. Photonics **8**, 865-870 (2014).
2. B. Jalali, and S. Fathpour, "Silicon photonics," J. Lightwave Technol. **24**, 4600-4615 (2006).
3. R. Soref, "The past, present, and future of silicon photonics," IEEE J. Sel. Top. Quant. **12**, 1678-1687 (2006).
4. W. Bogaerts, M. Fiers, and P. Dumon, "Design challenges in silicon photonics," IEEE J. Sel. Top. Quant. **20**, 1-8 (2014).
5. P. Dong, Y.-K. Chen, G.-H. Duan, and T. Neilson David, "Silicon photonic devices and integrated circuits," Nanophotonics **3**, 215-228 (2014).
6. A. Novack, M. Streshinsky, R. Ding, Y. Liu, E.-J. Lim Andy, G.-Q. Lo, T. Baehr-Jones, and M. Hochberg, "Progress in silicon platforms for integrated optics," Nanophotonics **3**, 205-214 (2014).
7. J. E. Bowers, "Silicon Photonic Integrated Circuits," in *Optical Fiber Communication Conference*(Optical Society of America, Los Angeles, California, 2015), p. W1B.1.
8. H. Subbaraman, X. Xu, A. Hosseini, X. Zhang, Y. Zhang, D. Kwong, and R. T. Chen, "Recent advances in silicon-based passive and active optical interconnects," Opt. Express **23**, 2487-2511 (2015).
9. J. Leuthold, C. Koos, and W. Freude, "Nonlinear silicon photonics," Nat. Photonics **4**, 535-544 (2010).
10. Y. Okawachi, A. L. Gaeta, and M. Lipson, "Breakthroughs in Nonlinear Silicon Photonics 2011," IEEE Photonics J. **4**, 601-606 (2012).
11. R. Salem, M. A. Foster, A. C. Turner, D. F. Geraghty, M. Lipson, and A. L. Gaeta, "Signal regeneration using low-power four-wave mixing on silicon chip," Nat. Photonics **2**, 35-38 (2008).
12. B. Kuyken, T. Ideguchi, S. Holzner, M. Yan, T. W. Hänsch, J. Van Campenhout, P. Verheyen, S. Coen, F. Leo, R. Baets, G. Roelkens, and N. Picqué, "An octave-spanning mid-infrared frequency comb generated in a silicon nanophotonic wire waveguide," Nat. Commun. **6** (2015).
13. G. E. Moore, "Cramming more components onto integrated circuits (Reprinted from Electronics, pg 114-117, April 19, 1965)," Proceedings of the IEEE **86**, 82-85 (1998).
14. M. Smit, J. van der Tol, and M. Hill, "Moore's law in photonics," Laser Photonics Rev. **6**, 1-13 (2012).
15. M. L. Brongersma, and V. M. Shalaev, "The Case for Plasmonics," Science **328**, 440-441 (2010).
16. W. L. Barnes, A. Dereux, and T. W. Ebbesen, "Surface plasmon subwavelength optics," Nature **424**, 824-830 (2003).
17. E. Ozbay, "Plasmonics: merging photonics and electronics at nanoscale dimensions," Science **311**, 189-193 (2006).
18. D. K. Gramotnev, and S. I. Bozhevolnyi, "Plasmonics beyond the diffraction limit," Nat. Photonics **4**, 83-91 (2010).
19. J. A. Schuller, E. S. Barnard, W. S. Cai, Y. C. Jun, J. S. White, and M. L. Brongersma, "Plasmonics for extreme light concentration and manipulation," Nat. Mater. **9**, 193-204 (2010).

20. M. Kauranen, and A. V. Zayats, "Nonlinear plasmonics," Nat. Photonics **6**, 737-748 (2012).
21. C. Langrock, S. Kumar, J. E. McGeehan, A. E. Willner, and M. M. Fejer, "All-optical signal processing using chi((2)) nonlinearities in guided-wave devices," J. Lightwave Technol. **24**, 2579-2592 (2006).
22. Y. Ben-Ezra, U. Mahlab, M. Haridim, and B. I. Lembrikov, "Applications of All-Optical Signal Processing in Modern Optical Communications," in *Transparent Optical Networks, 2007. ICTON '07. 9th International Conference on*(2007), pp. 328-331.
23. D. Zhang, and J. Zhu, "The application of the all-optical signal processing on the optical communication," in *Information Networking and Automation (ICINA), 2010 International Conference on*(2010), pp. V2-386-V382-389.
24. A. E. Willner, O. F. Yilmaz, W. Jian, W. Xiaoxia, A. Bogoni, Z. Lin, and S. R. Nuccio, "Optically Efficient Nonlinear Signal Processing," IEEE J. Sel. Top. Quant. **17**, 320-332 (2011).
25. A. E. Willner, S. Khaleghi, M. R. Chitgarha, and O. F. Yilmaz, "All-Optical Signal Processing," J. Lightwave Technol. **32**, 660-680 (2014).
26. D. Dimitropoulos, V. Raghunathan, R. Claps, and B. Jalali, "Phase-matching and nonlinear optical processes in silicon waveguides," Opt. Express **12**, 149-160 (2004).
27. R. L. Espinola, J. I. Dadap, R. M. Osgood, S. J. McNab, and Y. A. Vlasov, "C-band wavelength conversion in silicon photonic wire waveguides," Opt. Express **13**, 4341-4349 (2005).
28. C. Koos, L. Jacome, C. Poulton, J. Leuthold, and W. Freude, "Nonlinear silicon-on-insulator waveguides for all-optical signal processing," Opt. Express **15**, 5976-5990 (2007).
29. Q. Lin, O. J. Painter, and G. P. Agrawal, "Nonlinear optical phenomena in silicon waveguides: Modeling and applications," Opt. Express **15**, 16604-16644 (2007).
30. L. H. Yin, and G. P. Agrawal, "Impact of two-photon absorption on self-phase modulation in silicon waveguides," Opt. Lett. **32**, 2031-2033 (2007).
31. M. A. Foster, A. C. Turner, M. Lipson, and A. L. Gaeta, "Nonlinear optics in photonic nanowires," Opt. Express **16**, 1300-1320 (2008).
32. H. K. Tsang, and Y. Liu, "Nonlinear optical properties of silicon waveguides," Semicond. Sci. Tech. **23** (2008).
33. I. D. Rukhlenko, M. Premaratne, and G. P. Agrawal, "Nonlinear Silicon Photonics: Analytical Tools," IEEE J. Sel. Top. Quant. **16**, 200-215 (2010).
34. T. W. Baehr-Jones, and M. J. Hochberg, "Polymer Silicon Hybrid Systems: A Platform for Practical Nonlinear Optics†," The Journal of Physical Chemistry C **112**, 8085-8090 (2008).
35. J. Leuthold, W. Freude, J. M. Brosi, R. Baets, P. Dumon, I. Biaggio, M. L. Scimeca, F. Diederich, B. Frank, and C. Koos, "Silicon organic hybrid technology—A platform for practical nonlinear optics," Proceedings of the IEEE **97**, 1304-1316 (2009).
36. J. Leuthold, C. Koos, W. Freude, L. Alloatti, R. Palmer, D. Korn, J. Pfeifle, M. Lauermann, R. Dinu, S. Wehrli, M. Jazbinsek, P. Gunter, M. Waldow, T. Wahlbrink, J. Bolten, H. Kurz, M. Fournier, J. M. Fedeli, Y. Hui, and W. Bogaerts, "Silicon-Organic Hybrid Electro-Optical Devices," IEEE J. Sel. Top. Quant. **19**, 3401413-3401413 (2013).
37. Z. Xingyu, A. Hosseini, L. Xiaohui, H. Subbaraman, and R. T. Chen, "Polymer-Based Hybrid-Integrated Photonic Devices for Silicon On-Chip Modulation and Board-Level Optical Interconnects," IEEE J. Sel. Top. Quant. **19**, 3401115-3401115 (2013).

38. C. Koos, P. Vorreau, T. Vallaitis, P. Dumon, W. Bogaerts, R. Baets, B. Esembeson, I. Biaggio, T. Michinobu, F. Diederich, W. Freude, and J. Leuthold, "All-optical high-speed signal processing with silicon-organic hybrid slot waveguides," Nat. Photonics **3**, 216-219 (2009).
39. C. Koos, J. Leuthold, W. Freude, M. Kohl, L. Dalton, W. Bogaerts, A. L. Giesecke, M. Lauermann, A. Melikyan, S. Koeber, S. Wolf, C. Weimann, S. Muehlbrandt, K. Koehnle, J. Pfeifle, R. Palmer, L. Alloatti, D. Elder, T. Wahlbrink, and J. Bolten, "Silicon-Organic Hybrid (SOH) and Plasmonic-Organic Hybrid (POH) Integration," in *Optical Fiber Communication Conference*(Optical Society of America, Los Angeles, California, 2015), p. Tu2A.1.
40. A. Melikyan, K. Koehnle, M. Lauermann, R. Palmer, S. Koeber, S. Muehlbrandt, P. C. Schindler, D. L. Elder, S. Wolf, W. Heni, C. Haffner, Y. Fedoryshyn, D. Hillerkuss, M. Sommer, L. R. Dalton, D. Van Thourhout, W. Freude, M. Kohl, J. Leuthold, and C. Koos, "Plasmonic-organic hybrid (POH) modulators for OOK and BPSK signaling at 40 Gbit/s," Opt. Express **23**, 9938-9946 (2015).
41. C. Haffner, W. Heni, Y. Fedoryshyn, D. L. Elder, A. Melikyan, B. Baeuerle, J. Niegemann, A. Emboras, A. Josten, F. Ducry, M. Kohl, L. R. Dalton, D. Hillerkuss, C. Hafner, and J. Leuthold, "High-speed plasmonic Mach-Zehnder modulator in a waveguide," in *Optical Communication (ECOC), 2014 European Conference on*(2014), pp. 1-3.
42. A. Melikyan, L. Alloatti, A. Muslija, D. Hillerkuss, P. C. Schindler, J. Li, R. Palmer, D. Korn, S. Muehlbrandt, D. V. Thourhout, B. Chen, R. Dinu, M. Sommer, C. Koos, M. Kohl, W. Freude, and J. Leuthold, "High-speed plasmonic phase modulators," Nat. Photonics **8**, 229-233 (2014).
43. W. Heni, A. Melikyan, C. Haffner, Y. Fedoryshyn, B. Baeuerle, A. Josten, J. Niegemann, D. Hillerkuss, M. Kohl, D. Elder, L. Dalton, C. Hafner, and J. Leuthold, "Plasmonic Mach-Zehnder Modulator with >70 GHz Electrical Bandwidth Demonstrating 90 Gbit/s 4-ASK," in *Optical Fiber Communication Conference*(Optical Society of America, Los Angeles, California, 2015), p. Tu2A.2.
44. C. Haffner, W. Heni, Y. Fedoryshyn, J. Niegemann, A. Melikyan, D. L. Elder, B. Baeuerle, Y. Salamin, A. Josten, U. Koch, C. Hoessbacher, F. Ducry, L. Juchli, A. Emboras, D. Hillerkuss, M. Kohl, L. R. Dalton, C. Hafner, and J. Leuthold, "All-plasmonic Mach–Zehnder modulator enabling optical high-speed communication at the microscale," Nat. Photonics **9**, 525-528 (2015).
45. S. A. Maier, *Plasmonics: fundamentals and applications* (Springer Verlag, 2007).
46. M. J. Weber, *Handbook of optical materials* (CRC Press, 2003).
47. R. Kitamura, L. Pilon, and M. Jonasz, "Optical constants of silica glass from extreme ultraviolet to far infrared at near room temperature," Appl. Optics **46**, 8118-8133 (2007).
48. P. R. West, S. Ishii, G. V. Naik, N. K. Emani, V. M. Shalaev, and A. Boltasseva, "Searching for better plasmonic materials," Laser Photonics Rev. **4**, 795-808 (2010).
49. P. B. Johnson, and R. W. Christy, "Optical Constants of the Noble Metals," Phys. Rev. B **6**, 4370-4379 (1972).
50. J. B. Khurgin, "How to deal with the loss in plasmonics and metamaterials," Nat. Nanotechnol. **10**, 2-6 (2015).
51. M. L. Brongersma, "Introductory lecture: nanoplasmonics," Faraday Discussions **178**, 9-36 (2015).
52. R. W. Boyd, *Nonlinear Optics* (Academic, 2008).
53. E. Garmire, "Nonlinear optics in daily life," Opt. Express **21**, 30532-30544 (2013).
54. Z. Zalevsky, and I. Abdulhalim, *Integrated nanophotonic devices* (Elsevier, 2010).
55. S. Sederberg, and A. Y. Elezzabi, "Coherent Visible-Light-Generation Enhancement in Silicon-

Based Nanoplasmonic Waveguides via Third-Harmonic Conversion," Phys. Rev. Lett. **114**, 227401 (2015).

56. G. P. Agrawal, *Nonlinear Fiber Optics* (Academic Press, 2013).
57. R. M. Osgood, N. C. Panoiu, J. I. Dadap, X. Liu, X. Chen, I. W. Hsieh, E. Dulkeith, W. M. J. Green, and Y. A. Vlasov, "Engineering nonlinearities in nanoscale optical systems: physics and applications in dispersion-engineered silicon nanophotonic wires," Adv. Opt. Photon. **1**, 162-235 (2009).
58. A. W. Snyder, and D. L. John, "Optical waveguide theory," (Chapman and Hall, London New York, 1983).
59. Z. Ruan, G. Veronis, K. L. Vodopyanov, M. M. Fejer, and S. Fan, "Enhancement of optics-to-THz conversion efficiency by metallic slot waveguides," Opt. Express **17**, 13502-13515 (2009).
60. J. R. Krenn, B. Lamprecht, H. Ditlbacher, G. Schider, M. Salerno, A. Leitner, and F. R. Aussenegg, "Non–diffraction-limited light transport by gold nanowires," EPL (Europhysics Letters) **60**, 663 (2002).
61. H. Ditlbacher, A. Hohenau, D. Wagner, U. Kreibig, M. Rogers, F. Hofer, F. R. Aussenegg, and J. R. Krenn, "Silver Nanowires as Surface Plasmon Resonators," Phys. Rev. Lett. **95**, 257403 (2005).
62. S. Lal, J. H. Hafner, N. J. Halas, S. Link, and P. Nordlander, "Noble Metal Nanowires: From Plasmon Waveguides to Passive and Active Devices," Accounts of Chemical Research **45**, 1887-1895 (2012).
63. M. Quinten, A. Leitner, J. R. Krenn, and F. R. Aussenegg, "Electromagnetic energy transport via linear chains of silver nanoparticles," Opt. Lett. **23**, 1331-1333 (1998).
64. M. L. Brongersma, J. W. Hartman, and H. A. Atwater, "Electromagnetic energy transfer and switching in nanoparticle chain arrays below the diffraction limit," Phys. Rev. B **62**, R16356-R16359 (2000).
65. S. A. Maier, P. G. Kik, and H. A. Atwater, "Observation of coupled plasmon-polariton modes in Au nanoparticle chain waveguides of different lengths: Estimation of waveguide loss," Appl. Phys. Lett. **81**, 1714-1716 (2002).
66. S. A. Maier, P. G. Kik, H. A. Atwater, S. Meltzer, E. Harel, B. E. Koel, and A. A. G. Requicha, "Local detection of electromagnetic energy transport below the diffraction limit in metal nanoparticle plasmon waveguides," Nat. Mater. **2**, 229-232 (2003).
67. S. I. Bozhevolnyi, V. S. Volkov, E. Devaux, J. Y. Laluet, and T. W. Ebbesen, "Channel plasmon subwavelength waveguide components including interferometers and ring resonators," Nature **440**, 508-511 (2006).
68. D. F. P. Pile, T. Ogawa, D. K. Gramotnev, Y. Matsuzaki, K. C. Vernon, K. Yamaguchi, T. Okamoto, M. Haraguchi, and M. Fukui, "Two-dimensionally localized modes of a nanoscale gap plasmon waveguide," Appl. Phys. Lett. **87**, - (2005).
69. G. Veronis, and S. Fan, "Guided subwavelength plasmonic mode supported by a slot in a thin metal film," Opt. Lett. **30**, 3359-3361 (2005).
70. L. Liu, Z. Han, and S. He, "Novel surface plasmon waveguide for high integration," Opt. Express **13**, 6645-6650 (2005).
71. G. Veronis, and S. Fan, "Modes of Subwavelength Plasmonic Slot Waveguides," J. Lightwave Technol. **25**, 2511-2521 (2007).
72. Z. Han, A. Y. Elezzabi, and V. Van, "Experimental realization of subwavelength plasmonic slot

waveguides on a silicon platform," Opt. Lett. **35**, 502-504 (2010).

73. P. Berini, "Plasmon-polariton waves guided by thin lossy metal films of finite width: Bound modes of symmetric structures," Phys. Rev. B **61**, 10484 (2000).
74. P. Berini, R. Charbonneau, N. Lahoud, and G. Mattiussi, "Characterization of long-range surface-plasmon-polariton waveguides," J. Appl. Phys. **98**, 043109 (2005).
75. A. Boltasseva, T. Nikolajsen, K. Leosson, K. Kjaer, M. S. Larsen, and S. I. Bozhevolnyi, "Integrated optical components utilizing long-range surface plasmon polaritons," J. Lightwave Technol. **23**, 413-422 (2005).
76. M. Z. Alam, J. Meier, J. S. Aitchison, and M. Mojahedi, "Super Mode Propagation in Low Index Medium," in *Conference on Lasers and Electro-Optics/Quantum Electronics and Laser Science Conference and Photonic Applications Systems Technologies*(Optical Society of America, Baltimore, Maryland, 2007), p. JThD112.
77. R. F. Oulton, V. J. Sorger, D. A. Genov, D. F. P. Pile, and X. Zhang, "A hybrid plasmonic waveguide for subwavelength confinement and long-range propagation," Nat. Photonics **2**, 496-500 (2008).
78. D. Dai, and S. He, "A silicon-based hybrid plasmonic waveguide with a metal cap for a nano-scale light confinement," Opt. Express **17**, 16646-16653 (2009).
79. M. Wu, Z. H. Han, and V. Van, "Conductor-gap-silicon plasmonic waveguides and passive components at subwavelength scale," Opt. Express **18**, 11728-11736 (2010).
80. T. Holmgaard, and S. I. Bozhevolnyi, "Theoretical analysis of dielectric-loaded surface plasmon-polariton waveguides," Phys. Rev. B **75**, 245405 (2007).
81. J. Grandidier, S. Massenot, G. C. des Francs, A. Bouhelier, J. C. Weeber, L. Markey, A. Dereux, J. Renger, M. U. González, and R. Quidant, "Dielectric-loaded surface plasmon polariton waveguides: Figures of merit and mode characterization by image and Fourier plane leakage microscopy," Phys. Rev. B **78**, 245419 (2008).
82. S. Randhawa, A. V. Krasavin, T. Holmgaard, J. Renger, S. I. Bozhevolnyi, A. V. Zayats, and R. Quidant, "Experimental demonstration of dielectric-loaded plasmonic waveguide disk resonators at telecom wavelengths," Appl. Phys. Lett. **98**, 161102 (2011).
83. V. R. Almeida, Q. Xu, C. A. Barrios, and M. Lipson, "Guiding and confining light in void nanostructure," Opt. Lett. **29**, 1209-1211 (2004).
84. http://www.comsol.com/.
85. Y. Fu, X. Hu, C. Lu, S. Yue, H. Yang, and Q. Gong, "All-Optical Logic Gates Based on Nanoscale Plasmonic Slot Waveguides," Nano. Lett. **12**, 5784-5790 (2012).
86. A. Kriesch, S. P. Burgos, D. Ploss, H. Pfeifer, H. A. Atwater, and U. Peschel, "Functional Plasmonic Nanocircuits with Low Insertion and Propagation Losses," Nano. Lett. **13**, 4539-4545 (2013).
87. G. D. Osowiecki, E. Barakat, A. Naqavi, and H. P. Herzig, "Vertically coupled plasmonic slot waveguide cavity for localized biosensing applications," Opt. Express **22**, 20871-20880 (2014).
88. X. Yang, X. Hu, Z. Chai, C. Lu, H. Yang, and Q. Gong, "Tunable ultracompact chip-integrated multichannel filter based on plasmon-induced transparencies," Appl. Phys. Lett. **104**, 221114 (2014).
89. W. S. Cai, W. Shin, S. H. Fan, and M. L. Brongersma, "Elements for Plasmonic Nanocircuits with Three-Dimensional Slot Waveguides," Advanced Materials **22**, 5120-+ (2010).
90. I. D. Rukhlenko, M. Premaratne, and G. P. Agrawal, "Nonlinear propagation in silicon-based plasmonic waveguides from the standpoint of applications," Opt. Express **19**, 206-217 (2011).

91. S. B. Hasan, C. Rockstuhl, T. Pertsch, and F. Lederer, "Second-order nonlinear frequency conversion processes in plasmonic slot waveguides," J. Opt. Soc. Am. B **29**, 1606-1611 (2012).
92. A. Kriesch, D. Ploss, J. Wen, and U. Peschel, "Nonlinear switching in a purely plasmonic directional coupler," in *Advanced Photonics Congress*(Optical Society of America, Colorado Springs, Colorado, 2012), p. JM5A.47.
93. T. Wu, Y. Sun, X. Shao, P. P. Shum, and T. Huang, "Efficient phase-matched third harmonic generation in an asymmetric plasmonic slot waveguide," Opt. Express **22**, 18612-18624 (2014).
94. J. Zhang, E. Cassan, D. Gao, and X. Zhang, "Highly efficient phase-matched second harmonic generation using an asymmetric plasmonic slot waveguide configuration in hybrid polymer-silicon photonics," Opt. Express **21**, 14876-14887 (2013).
95. J. Zhang, E. Cassan, and X. Zhang, "Electrically controlled second-harmonic generation in silicon-compatible plasmonic slot waveguides: a new modulation scheme," Opt. Lett. **39**, 4001-4004 (2014).
96. J. Zhang, L. Shi, Y. Wang, E. Cassan, and X. Zhang, "On-chip high-speed optical detection based on an optical rectification scheme in silicon plasmonic platform," Opt. Express **22**, 27504-27514 (2014).
97. R. F. Oulton, V. J. Sorger, T. Zentgraf, R.-M. Ma, C. Gladden, L. Dai, G. Bartal, and X. Zhang, "Plasmon lasers at deep subwavelength scale," Nature **461**, 629-632 (2009).
98. X. Sun, L. Zhou, X. Li, Z. Hong, and J. Chen, "Design and analysis of a phase modulator based on a metal-polymer-silicon hybrid plasmonic waveguide," Appl. Optics **50**, 3428-3434 (2011).
99. F. Lou, D. Dai, L. Thylen, and L. Wosinski, "Design and analysis of ultra-compact EO polymer modulators based on hybrid plasmonic microring resonators," Opt. Express **21**, 20041-20051 (2013).
100. F. Lou, Z. Wang, D. Dai, L. Thylen, and L. Wosinski, "Experimental demonstration of ultra-compact directional couplers based on silicon hybrid plasmonic waveguides," Appl. Phys. Lett. **100**, 241105-241104 (2012).
101. J. Niklas Caspers, and M. Mojahedi, "Measurement of a compact colorless 3 dB hybrid plasmonic directional coupler," Opt. Lett. **39**, 3262-3265 (2014).
102. M. Z. Alam, J. S. Aitchison, and M. Mojahedi, "Polarization-independent hybrid plasmonic coupler for a silicon on insulator platform," Opt. Lett. **37**, 3417-3419 (2012).
103. D. X. Dai, Y. C. Shi, S. L. He, L. Wosinski, and L. Thylen, "Silicon hybrid plasmonic submicron-donut resonator with pure dielectric access waveguides," Opt. Express **19**, 23671-23682 (2011).
104. H. S. Chu, Y. Akimov, P. Bai, and E. P. Li, "Submicrometer radius and highly confined plasmonic ring resonator filters based on hybrid metal-oxide-semiconductor waveguide," Opt. Lett. **37**, 4564-4566 (2012).
105. S. Y. Zhu, G. Q. Lo, and D. L. Kwong, "Performance of ultracompact copper-capped silicon hybrid plasmonic waveguide-ring resonators at telecom wavelengths," Opt. Express **20**, 15232-15246 (2012).
106. F. Lou, D. X. Dai, and L. Wosinski, "Ultracompact polarization beam splitter based on a dielectric-hybrid plasmonic-dielectric coupler," Opt. Lett. **37**, 3372-3374 (2012).
107. X. Sun, M. Z. Alam, S. J. Wagner, J. S. Aitchison, and M. Mojahedi, "Experimental demonstration of a hybrid plasmonic transverse electric pass polarizer for a silicon-on-insulator platform," Opt. Lett. **37**, 4814-4816 (2012).
108. J. Zhang, E. Cassan, and X. Zhang, "Wideband and Compact TE-Pass/TM-Stop Polarizer Based on

a Hybrid Plasmonic Bragg Grating for Silicon Photonics," J. Lightwave Technol. **32**, 1383-1386 (2014).

109. F. F. Lu, T. Li, X. P. Hu, Q. Q. Cheng, S. N. Zhu, and Y. Y. Zhu, "Efficient second-harmonic generation in nonlinear plasmonic waveguide," Opt. Lett. **36**, 3371-3373 (2011).
110. S. Aldawsari, and B. R. West, "Hybrid plasmonic waveguides for nonlinear applications," in *Photonics Global Conference (PGC), 2012*(2012), pp. 1-4.
111. A. Pitilakis, and E. E. Kriezis, "Highly nonlinear hybrid silicon-plasmonic waveguides: analysis and optimization," J. Opt. Soc. Am. B **30**, 1954-1965 (2013).
112. T. Wu, P. P. Shum, X. Shao, T. Huang, and Y. Sun, "Third harmonic generation from mid-IR to near-IR regions in a phase-matched silicon-silicon-nanocrystal hybrid plasmonic waveguide," Opt. Express **22**, 24367-24377 (2014).
113. J. Zhang, E. Cassan, and X. Zhang, "Efficient second harmonic generation from mid-infrared to near-infrared regions in silicon-organic hybrid plasmonic waveguides with small fabrication-error sensitivity and a large bandwidth," Opt. Lett. **38**, 2089-2091 (2013).
114. J. Zhang, P. Zhao, E. Cassan, and X. Zhang, "Phase regeneration of phase-shift keying signals in highly nonlinear hybrid plasmonic waveguides," Opt. Lett. **38**, 848-850 (2013).
115. J. Zhang, E. Cassan, and X. Zhang, "Enhanced mid-to-near-infrared second harmonic generation in silicon plasmonic microring resonators with low pump power," Photon. Res. **2**, 143-149 (2014).
116. H. Kogenlnik, "2. Theory of dielectric waveguides," in *Integrated Optics*(Springer Berlin / Heidelberg, 1975), pp. 13-81.
117. A.-S. B.-B. Dhia, G. Dakhia, C. Hazard, and L. Chorfi, "Diffraction by a Defect in an Open Waveguide: A Mathematical Analysis Based on a Modal Radiation Condition," SIAM Journal on Applied Mathematics **70**, 677-693 (2009).
118. R. W. Boyd, and G. L. Fischer, "Nonlinear optical materials," Elsevier Science, 6237-6244 (2001).
119. G. I. Stegeman, and W. E. Torruellas, "Nonlinear Materials for Information Processing and Communications," Philosophical Transactions of the Royal Society of London. Series A: Mathematical, Physical and Engineering Sciences **354**, 745-756 (1996).
120. M. Dinu, F. Quochi, and H. Garcia, "Third-order nonlinearities in silicon at telecom wavelengths," Appl. Phys. Lett. **82**, 2954-2956 (2003).
121. A. D. Bristow, N. Rotenberg, and H. M. van Driel, "Two-photon absorption and Kerr coefficients of silicon for 850-2200 nm," Appl. Phys. Lett. **90** (2007).
122. Q. Lin, J. Zhang, G. Piredda, R. W. Boyd, P. M. Fauchet, and G. P. Agrawal, "Dispersion of silicon nonlinearities in the near infrared region," Appl. Phys. Lett. **91** (2007).
123. F. Gholami, S. Zlatanovic, A. Simic, L. Liu, D. Borlaug, N. Alic, M. P. Nezhad, Y. Fainman, and S. Radic, "Third-order nonlinearity in silicon beyond 2350 nm," Appl. Phys. Lett. **99** (2011).
124. D. J. Moss, R. Morandotti, A. L. Gaeta, and M. Lipson, "New CMOS-compatible platforms based on silicon nitride and Hydex for nonlinear optics," Nat. Photonics **7**, 597-607 (2013).
125. J. Clark, and G. Lanzani, "Organic photonics for communications," Nat. Photonics **4**, 438-446 (2010).
126. L. R. Dalton, S. Benight, D. Elder, and J. Song, "Integration of New Organic Electro-Optic Materials into Silicon and Silicon Nitride Photonics and into Metamaterial and Plasmonic Device Structures," in *Frontiers in Optics 2011/Laser Science XXVII*(Optical Society of America, San Jose, California,

2011), p. FWBB1.
127. J. D. Luo, and A. K. Y. Jen, "Highly Efficient Organic Electrooptic Materials and Their Hybrid Systems for Advanced Photonic Devices," IEEE J. Sel. Top. Quant. **19** (2013).
128. GuT, PetroneN, J. F. McMillan, A. van der Zande, YuM, G. Q. Lo, D. L. Kwong, HoneJ, and C. W. Wong, "Regenerative oscillation and four-wave mixing in graphene optoelectronics," Nat. Photonics **6**, 554-559 (2012).
129. S. A. Mikhailov, "Theory of the nonlinear optical frequency mixing effect in graphene," Physica E: Low-dimensional Systems and Nanostructures **44**, 924-927 (2012).
130. J. D. Cox, and F. Javier García de Abajo, "Electrically tunable nonlinear plasmonics in graphene nanoislands," Nat. Commun. **5** (2014).
131. C. Donnelly, and D. T. H. Tan, "Ultra-large nonlinear parameter in graphene-silicon waveguide structures," Opt. Express **22**, 22820-22830 (2014).
132. Y. Enami, C. T. Derose, D. Mathine, C. Loychik, C. Greenlee, R. A. Norwood, T. D. Kim, J. Luo, Y. Tian, A. K.-Y. Jen, and N. Peyghambarian, "Hybrid polymer/sol–gel waveguide modulators with exceptionally large electro–optic coefficients," Nat. Photonics **1**, 180-185 (2007).
133. E. M. McKenna, A. S. Lin, A. R. Mickelson, R. Dinu, and D. Jin, "Comparison of r33 values for AJ404 films prepared with parallel plate and corona poling," J. Opt. Soc. Am. B **24**, 2888-2892 (2007).
134. R. Palmer, S. Koeber, D. L. Elder, M. Woessner, W. Heni, D. Korn, M. Lauermann, W. Bogaerts, L. Dalton, W. Freude, J. Leuthold, and C. Koos, "High-Speed, Low Drive-Voltage Silicon-Organic Hybrid Modulator Based on a Binary-Chromophore Electro-Optic Material," J. Lightwave Technol. **32**, 2726-2734 (2014).
135. B. Esembeson, M. L. Scimeca, T. Michinobu, F. Diederich, and I. Biaggio, "A High-Optical Quality Supramolecular Assembly for Third-Order Integrated Nonlinear Optics," Advanced Materials **20**, 4584-4587 (2008).
136. A. Leszczynska, J. Njuguna, K. Pielichowski, and J. R. Banerjee, "Polymer/montmorillonite nanocomposites with improved thermal properties. Part I. Factors influencing thermal stability and mechanisms of thermal stability improvement," Thermochim. Acta **453**, 75-96 (2007).
137. S. V. Rao, K. Moutzouris, and M. Ebrahimzadeh, "Nonlinear frequency conversion in semiconductor optical waveguides using birefringent, modal and quasi-phase-matching techniques," Journal of Optics A: Pure and Applied Optics **6**, 569 (2004).
138. M. M. Fejer, G. Magel, D. H. Jundt, and R. L. Byer, "Quasi-phase-matched second harmonic generation: tuning and tolerances," Quantum Electronics, IEEE Journal of **28**, 2631-2654 (1992).
139. F. F. Lu, T. Li, J. Xu, Z. D. Xie, L. Li, S. N. Zhu, and Y. Y. Zhu, "Surface plasmon polariton enhanced by optical parametric amplification in nonlinear hybrid waveguide," Opt. Express **19**, 2858-2865 (2011).
140. F. M. Pigozzo, D. Modotto, and S. Wabnitz, "Second harmonic generation by modal phase matching involving optical and plasmonic modes," Opt. Lett. **37**, 2244-2246 (2012).
141. S. B. Hasan, C. Rockstuhl, T. Pertsch, and F. Lederer, "Second-order nonlinear frequency conversion processes in plasmonic slot waveguides," J. Opt. Soc. Am. B **29**, 1606-1611 (2012).
142. J. C. Quail, and H. J. Simon, "Second-harmonic generation with phase-matched long-range and short-range surface plasmons," J. Appl. Phys. **56**, 2589-2591 (1984).

143. A. R. Davoyan, I. V. Shadrivov, and Y. S. Kivshar, "Quadratic phase matching in nonlinear plasmonic nanoscale waveguides," Opt. Express **17**, 20063-20068 (2009).
144. M. Hochberg, T. Baehr-Jones, G. Wang, J. Huang, P. Sullivan, L. Dalton, and A. Scherer, "Towards a millivolt optical modulator with nano-slot waveguides," Opt. Express **15**, 8401-8410 (2007).
145. S. Afshar V, and T. M. Monro, "A full vectorial model for pulse propagation in emerging waveguides with subwavelength structures part I: Kerr nonlinearity," Opt. Express **17**, 2298-2318 (2009).
146. K. J. Vahala, "Optical microcavities," Nature **424**, 839-846 (2003).
147. T. F. Krauss, "Why do we need slow light?," Nat. Photonics **2**, 448-450 (2008).
148. T. Baba, "Slow light in photonic crystals," Nat. Photonics **2**, 465-473 (2008).
149. M. Cazzanelli, F. Bianco, E. Borga, G. Pucker, M. Ghulinyan, E. Degoli, E. Luppi, V. Véniard, S. Ossicini, and D. Modotto, "Second-harmonic generation in silicon waveguides strained by silicon nitride," Nat. Mater. **11**, 148-154 (2011).
150. J. S. Levy, M. A. Foster, A. L. Gaeta, and M. Lipson, "Harmonic generation in silicon nitride ring resonators," Opt. Express **19**, 11415-11421 (2011).
151. R. E. P. de Oliveira, M. Lipson, and C. J. S. de Matos, "Electrically Controlled Silicon Nitride Ring Resonator for Quasi-phase Matched Second-harmonic Generation," in *CLEO: Science and Innovations*(Optical Society of America2012).
152. T. Y. Ning, H. Pietarinen, O. Hyvarinen, R. Kumar, T. Kaplas, M. Kauranen, and G. Genty, "Efficient second-harmonic generation in silicon nitride resonant waveguide gratings," Opt. Lett. **37**, 4269-4271 (2012).
153. M. L. Brongersma, and P. G. Kik, *Surface plasmon nanophotonics* (Springer, 2007).
154. M. I. Stockman, "Nanoplasmonics: past, present, and glimpse into future," Opt. Express **19**, 22029-22106 (2011).
155. W. S. Cai, A. P. Vasudev, and M. L. Brongersma, "Electrically Controlled Nonlinear Generation of Light with Plasmonics," Science **333**, 1720-1723 (2011).
156. Z. Wu, X. Hu, Z. Yu, W. Hu, F. Xu, and Y. Lu, "Nonlinear plasmonic frequency conversion through quasiphase matching," Phys. Rev. B **82**, 155107 (2010).
157. M. I. Stockman, D. J. Bergman, C. Anceau, S. Brasselet, and J. Zyss, "Enhanced second-harmonic generation by metal surfaces with nanoscale roughness: nanoscale dephasing, depolarization, and correlations," Phys. Rev. Lett. **92**, 057402 (2004).
158. P. Schon, N. Bonod, E. Devaux, J. Wenger, H. Rigneault, T. W. Ebbesen, and S. Brasselet, "Enhanced second-harmonic generation from individual metallic nanoapertures," Opt. Lett. **35**, 4063-4065 (2010).
159. B. Z. Steinberg, "Parametric plasmonics and second harmonic generation in particle chains," Opt. Express **19**, 25843-25853 (2011).
160. J. Richter, A. Steinbrück, T. Pertsch, A. Tünnermann, and R. Grange, "Plasmonic Core–Shell Nanowires for Enhanced Second-Harmonic Generation," Plasmonics, 1-6 (2012).
161. G. T. Reed, and A. P. Knights, *Silicon photonics* (Wiley Online Library, 2008).
162. L. Alloatti, D. Korn, C. Weimann, C. Koos, W. Freude, and J. Leuthold, "Second-order nonlinear silicon-organic hybrid waveguides," Opt. Express **20**, 20506-20515 (2012).
163. M. Jazbinsek, L. Mutter, and P. Gunter, "Photonic Applications With the Organic Nonlinear Optical Crystal DAST," IEEE J. Sel. Top. Quant. **14**, 1298-1311 (2008).

164. R. Thomas, Z. Ikonic, and R. W. Kelsall, "Silicon based plasmonic coupler," Opt. Express **20**, 21520-21531 (2012).
165. R. W. Terhune, P. D. Maker, and C. M. Savage, "Optical Harmonic Generation in Calcite," Phys. Rev. Lett. **8**, 404-406 (1962).
166. C. G. Bethea, "Electric field induced second harmonic generation in glass," Appl. Optics **14**, 2435-2437 (1975).
167. K. Kikuchi, and K. Tada, "Theory of electric field-induced optical second harmonic generation in semiconductors," Optical and Quantum Electronics **12**, 199-205 (1980).
168. R. Kashyap, "Phase-matched periodic electric-field-induced second-harmonic generation in optical fibers," J. Opt. Soc. Am. B **6**, 313-328 (1989).
169. P. S. Weitzman, J. J. Kester, and U. Osterberg, "Electric field induced second harmonic generation in germanium doped silica planar waveguides," Electron Lett. **30**, 697-698 (1994).
170. R. E. P. de Oliveira, and C. J. S. de Matos, "Quasi-phase-matched second harmonic generation in silicon nitride ring resonators controlled by static electric field," Opt. Express **21**, 32690-32698 (2013).
171. H. Kishida, T. Hasegawa, Y. Iwasa, T. Koda, Y. Tokura, H. Tachibana, M. Matsumoto, S. Wada, T. T. Lay, and H. Tashiro, "Electric-field-induced second-harmonic generation mediated by one-dimensional excitons in polysilanes," Phys. Rev. B **50**, 7786-7792 (1994).
172. D. Xiao, E. Ramsay, D. T. Reid, B. Offenbeck, and N. Weber, "Optical probing of a silicon integrated circuit using electric-field-induced second-harmonic generation," Appl. Phys. Lett. **88**, 114107-114103 (2006).
173. O. A. Aktsipetrov, A. A. Fedyanin, A. V. Melnikov, E. D. Mishina, A. N. Rubtsov, M. H. Anderson, P. T. Wilson, M. ter Beek, X. F. Hu, J. I. Dadap, and M. C. Downer, "dc-electric-field-induced and low-frequency electromodulation second-harmonic generation spectroscopy of Si(001)-SiO_{2} interfaces," Physical Review B **60**, 8924-8938 (1999).
174. D. Taguchi, M. Weis, T. Manaka, and M. Iwamoto, "Probing of carrier behavior in organic electroluminescent diode using electric field induced optical second-harmonic generation measurement," Appl. Phys. Lett. **95**, 263310-263310-263313 (2009).
175. H. Kishida, K. Hirota, T. Wakabayashi, H. Okamoto, H. Kokubo, and T. Yamamoto, "Third-order optical nonlinearity in regio-controlled polythiophene films," Appl. Phys. Lett. **87**, 121902-121903 (2005).
176. M. Bass, P. A. Franken, J. F. Ward, and G. Weinreich, "Optical Rectification," Phys. Rev. Lett. **9**, 446-448 (1962).
177. T. J. Carrig, G. Rodriguez, T. Sharp Clement, A. J. Taylor, and K. R. Stewart, "Generation of terahertz radiation using electro‐optic crystal mosaics," Appl. Phys. Lett. **66**, 10-12 (1995).
178. A. Nahata, D. H. Auston, C. Wu, and J. T. Yardley, "Generation of terahertz radiation from a poled polymer," Appl. Phys. Lett. **67**, 1358-1360 (1995).
179. A. Nahata, and T. F. Heinz, "Generation of subpicosecond electrical pulses by optical rectification," Opt. Lett. **23**, 867-869 (1998).
180. S. Graf, H. Sigg, and W. Bächtold, "High-frequency electrical pulse generation using optical rectification in bulk GaAs," Appl. Phys. Lett. **76**, 2647-2649 (2000).
181. Y.-Q. Lu, M. Xiao, and G. J. Salamo, "Coherent microwave generation in a nonlinear photonic

crystal," IEEE J. Quantum Elect. **38**, 481-485 (2002).

182. V. Loyo-Maldonado, H. K. Lee, C. R. Stanley, S. V. Rao, K. Moutzouris, M. Ebrahimzadeh, and J. S. Aitchison, "Generation of ultrashort electrical pulses in semiconductor waveguides," Photonics Technology Letters, IEEE **15**, 428-430 (2003).
183. Q. Wu, M. Litz, and X. C. Zhang, "Broadband detection capability of ZnTe electro-optic field detectors," Appl. Phys. Lett. **68**, 2924-2926 (1996).
184. T. Baehr-Jones, M. Hochberg, G. Wang, R. Lawson, Y. Liao, P. Sullivan, L. Dalton, A. Jen, and A. Scherer, "Optical modulation and detection in slotted Silicon waveguides," Opt. Express **13**, 5216-5226 (2005).
185. G. M. Mikheev, R. G. Zonov, A. N. Obraztsov, A. P. Volkov, and Y. P. Svirko, "Quick-response film photodetector of high-power laser radiation based on the optical rectification effect," Tech. Phys. **51**, 1190-1196 (2006).
186. J. Zhang, J. D. Bull, and T. E. Darcie, "Microwave photonic signal detection using phase-matched optical rectification in an AlGaAs waveguide," IEEE Photonic Tech. L. **19**, 2012-2014 (2007).
187. T. Baehr-Jones, J. Witzens, and M. Hochberg, "Theoretical Study of Optical Rectification at Radio Frequencies in a Slot Waveguide," Quantum Electronics, IEEE Journal of **46**, 1634-1641 (2010).
188. D. R. Ward, F. Hüser, F. Pauly, J. C. Cuevas, and D. Natelson, "Optical rectification and field enhancement in a plasmonic nanogap," Nat. Nanotechnol. **5**, 732-736 (2010).
189. B. Lau, M. A. Swillam, and A. S. Helmy, "Hybrid orthogonal junctions: wideband plasmonic slot-silicon waveguide couplers," Opt. Express **18**, 27048-27059 (2010).
190. J. Zhang, E. Cassan, and X. Zhang, "Electrically controlled second harmonic generation in silicon-compatible plasmonic slot waveguides: a new modulation scheme," Opt. Lett. (2014).
191. Z. Fang, and C. Z. Zhao, "Recent Progress in Silicon Photonics: A Review," ISRN Optics **2012**, 27 (2012).
192. R. Soref, "Mid-infrared photonics in silicon and germanium," Nat. Photonics **4**, 495-497 (2010).
193. G. Z. Mashanovich, M. M. Milosevic, M. Nedeljkovic, N. Owens, B. Q. Xiong, E. J. Teo, and Y. F. Hu, "Low loss silicon waveguides for the mid-infrared," Opt. Express **19**, 7112-7119 (2011).
194. A. Spott, Y. Liu, T. W. Baehr-Jones, R. Ilic, and M. Hochberg, "Mid-infrared photonics in silicon," presented at the *Proc. SPIE 7917*, Nonlinear Frequency Generation and Conversion: Materials, Devices, and Applications X, San Francisco, California, USA2011.
195. M. M. Milosevic, M. Nedeljkovic, T. M. Ben Masaud, E. Jaberansary, H. M. H. Chong, N. G. Emerson, G. T. Reed, and G. Z. Mashanovich, "Silicon waveguides and devices for the mid-infrared," Appl. Phys. Lett. **101**, 121105 (2012).
196. R. Soref, "Toward silicon-based longwave integrated optoelectronics (LIO)," in *Proc. SPIE 6898, Silicon Photonics III*, J. A. Kubby, and G. T. Reed, eds. (San Jose, CA, 2008), p. 689809.
197. B. Jalali, "SILICON PHOTONICS Nonlinear optics in the mid-infrared," Nat. Photonics **4**, 506-508 (2010).
198. S. Zlatanovic, J. S. Park, S. Moro, J. M. C. Boggio, I. B. Divliansky, N. Alic, S. Mookherjea, and S. Radic, "Mid-infrared wavelength conversion in silicon waveguides using ultracompact telecom-band-derived pump source," Nat. Photonics **4**, 561-564 (2010).
199. X. P. Liu, B. Kuyken, G. Roelkens, R. Baets, R. M. Osgood, and W. M. J. Green, "Bridging the mid-infrared-to-telecom gap with silicon nanophotonic spectral translation," Nat. Photonics **6**, 667-671

(2012).

200. E. K. Tien, Y. W. Huang, S. M. Gao, Q. Song, F. Qian, S. K. Kalyoncu, and O. Boyraz, "Discrete parametric band conversion in silicon for mid-infrared applications," Opt. Express **18**, 21981-21989 (2010).
201. B. Kuyken, X. Liu, R. M. Osgood, Y. A. Vlasov, G. Roelkens, R. Baets, and W. M. J. Green, "Frequency conversion of mid-infrared optical signals into the telecom band using nonlinear silicon nanophotonic wires," presented at the Optical Fiber Communication Conference and Exposition (OFC/NFOEC), 2011 and the National Fiber Optic Engineers Conference, Los Angeles, CA2011.
202. C. Xiong, W. Pernice, K. K. Ryu, C. Schuck, K. Y. Fong, T. Palacios, and H. X. Tang, "Integrated GaN photonic circuits on silicon (100) for second harmonic generation," Opt. Express **19**, 10462-10470 (2011).
203. W. H. P. Pernice, C. Xiong, C. Schuck, and H. X. Tang, "Second harmonic generation in phase matched aluminum nitride waveguides and micro-ring resonators," Appl. Phys. Lett. **100** (2012).
204. Z. A. F. Bi, A. Rodriguez, H. Hashemi, D. Duchesne, M. Loncar, K. M. Wang, and S. G. Johnson, "High-efficiency second-harmonic generation in doubly-resonant $\chi^{(2)}$ microring resonators," Opt. Express **20**, 7526-7543 (2012).
205. A. C. Turner, M. A. Foster, A. L. Gaeta, and M. Lipson, "Ultra-low power parametric frequency conversion in a silicon microring resonator," Opt. Express **16**, 4881-4887 (2008).
206. M. Ferrera, D. Duchesne, L. Razzari, M. Peccianti, R. Morandotti, P. Cheben, S. Janz, D. X. Xu, B. E. Little, S. Chu, and D. J. Moss, "Low power four wave mixing in an integrated, micro-ring resonator with Q=1.2 million," Opt. Express **17**, 14098-14103 (2009).
207. A. Pasquazi, R. Ahmad, M. Rochette, M. Lamont, B. E. Little, S. T. Chu, R. Morandotti, and D. J. Moss, "All-optical wavelength conversion in an integrated ring resonator," Opt. Express **18**, 3858-3863 (2010).
208. Z. Q. Li, S. M. Gao, Q. A. Liu, and S. L. He, "Modified model for four-wave mixing-based wavelength conversion in silicon micro-ring resonators," Opt. Commun. **284**, 2215-2221 (2011).
209. X. Y. Zhang, A. Hu, J. Z. Wen, T. Zhang, X. J. Xue, Y. Zhou, and W. W. Duley, "Numerical analysis of deep sub-wavelength integrated plasmonic devices based on Semiconductor-Insulator-Metal strip waveguides," Opt. Express **18**, 18945-18959 (2010).
210. K. Okamoto, *Fundamentals of optical waveguides* (Academic press, 2010).
211. Y. Liu, T. Chang, and A. E. Craig, "Coupled mode theory for modeling microring resonators," Opt. Eng. **44**, 084601-084601-084606 (2005).
212. Y. Bian, Z. Zheng, X. Zhao, J. Zhu, and T. Zhou, "Symmetric hybrid surface plasmon polariton waveguides for 3D photonic integration," Opt. Express **17**, 21320-21325 (2009).
213. L. Chen, T. Zhang, X. Li, and W. Huang, "Novel hybrid plasmonic waveguide consisting of two identical dielectric nanowires symmetrically placed on each side of a thin metal film," Opt. Express **20**, 20535-20544 (2012).
214. G. Martin, S. Ducci, R. Hierle, D. Josse, and J. Zyss, "Quasiphase matched second-harmonic generation from periodic optical randomization of poled polymer channel waveguides," Appl. Phys. Lett. **83**, 1086-1088 (2003).
215. J. J. Ju, J. Kim, J. Y. Do, M.-s. Kim, S. K. Park, S. Park, and M.-H. Lee, "Second-harmonic generation in periodically poled nonlinear polymer waveguides," Opt. Lett. **29**, 89-91 (2004).

216. S. Zhu, G. Q. Lo, and D. L. Kwong, "Low-loss amorphous silicon wire waveguide for integrated photonics: effect of fabrication process and the thermal stability," Opt. Express **18**, 25283-25291 (2010).
217. R. Slavík, F. Parmigiani, J. Kakande, C. Lundström, M. Sjödin, P. A. Andrekson, R. Weerasuriya, S. Sygletos, A. D. Ellis, and L. Grüner-Nielsen, "All-optical phase and amplitude regenerator for next-generation telecommunications systems," Nat. Photonics **4**, 690-695 (2010).
218. http://www.gigoptix.com/.
219. L. Alloatti, D. Korn, R. Palmer, D. Hillerkuss, J. Li, A. Barklund, R. Dinu, J. Wieland, M. Fournier, J. Fedeli, H. Yu, W. Bogaerts, P. Dumon, R. Baets, C. Koos, W. Freude, and J. Leuthold, "42.7 Gbit/s electro-optic modulator in silicon technology," Opt. Express **19**, 11841-11851 (2011).
220. J. Tian, S. Yu, W. Yan, and M. Qiu, "Broadband high-efficiency surface-plasmon-polariton coupler with silicon-metal interface," Appl. Phys. Lett. **95**, 013504 (2009).
221. C. c. Delacour, S. Blaize, P. Grosse, J. M. Fedeli, A. l. Bruyant, R. Salas-Montiel, G. Lerondel, and A. Chelnokov, "Efficient Directional Coupling between Silicon and Copper Plasmonic Nanoslot Waveguides: toward Metal−Oxide−Silicon Nanophotonics," Nano. Lett. **10**, 2922-2926 (2010).
222. R. Salas-Montiel, A. Apuzzo, C. Delacour, Z. Sedaghat, A. Bruyant, P. Grosse, A. Chelnokov, G. Lerondel, and S. Blaize, "Quantitative analysis and near-field observation of strong coupling between plasmonic nanogap and silicon waveguides," Appl. Phys. Lett. **100**, 231109-231109-231104 (2012).
223. A. Andryieuski, V. A. Zenin, R. Malureanu, V. S. Volkov, S. I. Bozhevolnyi, and A. V. Lavrinenko, "Direct Characterization of Plasmonic Slot Waveguides and Nanocouplers," Nano. Lett. **14**, 3925-3929 (2014).
224. T. Dirk, L. Frederik Van, A. Melanie, B. Wim, T. Dries Van, B. Peter, and B. Roel, "Grating Couplers for Coupling between Optical Fibers and Nanophotonic Waveguides," Japanese Journal of Applied Physics **45**, 6071 (2006).
225. D. Benedikovic, C. Alonso-Ramos, P. Cheben, J. H. Schmid, S. Wang, D.-X. Xu, J. Lapointe, S. Janz, R. Halir, A. Ortega-Moñux, J. G. Wangüemert-Pérez, I. Molina-Fernández, J.-M. Fédéli, L. Vivien, and M. Dado, "High-directionality fiber-chip grating coupler with interleaved trenches and subwavelength index-matching structure," Opt. Lett. **40**, 4190-4193 (2015).
226. J. A. Dionne, L. A. Sweatlock, M. T. Sheldon, A. P. Alivisatos, and H. A. Atwater, "Silicon-Based Plasmonics for On-Chip Photonics," IEEE J. Sel. Top. Quant. **16**, 295-306 (2010).
227. K. Jin Tae, and P. Suntak, "The Design and Analysis of Monolithic Integration of CMOS-Compatible Plasmonic Waveguides for On-Chip Electronic-Photonic Integrated Circuits," J. Lightwave Technol. **31**, 2974-2981 (2013).
228. J. Leuthold, C. Hoessbacher, S. Muehlbrandt, A. Melikyan, M. Kohl, C. Koos, W. Freude, V. Dolores-Calzadilla, M. Smit, I. Suarez, J. Martínez-Pastor, E. P. Fitrakis, and I. Tomkos, "Plasmonic Communications: Light on a Wire," Opt. Photon. News **24**, 28-35 (2013).
229. G. V. Naik, V. M. Shalaev, and A. Boltasseva, "Alternative Plasmonic Materials: Beyond Gold and Silver," Advanced Materials **25**, 3264-3294 (2013).
230. F. J. Garcia de Abajo, R. Sapienza, M. Noginov, F. Benz, J. Baumberg, S. Maier, D. Graham, J. Aizpurua, T. Ebbesen, A. Pinchuk, J. Khurgin, K. Matczyszyn, J. T. Hugall, N. van Hulst, P. Dawson, C. Roberts, M. Nielsen, L. Bursi, M. Flatte, J. Yi, O. Hess, N. Engheta, M. Brongersma, V. Podolskiy,

V. Shalaev, E. Narimanov, and A. Zayats, "Plasmonic and new plasmonic materials: general discussion," Faraday Discussions **178**, 123-149 (2015).

231. N. Kinsey, M. Ferrera, V. M. Shalaev, and A. Boltasseva, "Examining nanophotonics for integrated hybrid systems: a review of plasmonic interconnects and modulators using traditional and alternative materials [Invited]," J. Opt. Soc. Am. B **32**, 121-142 (2015).

Enhancement of nonlinear effects using silicon plasmonic structures

With the rapid increasing bandwidth of data transmission and signal processing, integrated electronics encounters strong bottlenecks. Silicon photonics provides a low-cost solution to overcome some of these bottlenecks by introducing on-chip optical links. After a decade of development, silicon photonics is now the most active discipline and most promising platform within the field of integrated optics. However, in the process of further development, new stumbling blocks emerge, among which the fact that the size of photonic devices is limited by the diffraction limit, which results in a large mismatch between photonic and electronic components. Plasmonics seems to be an ideal solution to overcome this obstacle thanks to its ability to confine the optical field into nanoscales beyond the diffraction limit. Meanwhile, the localized strong field enhancement in plasmonic structures enhances interaction of light and matter, which is promising for nonlinear applications.

In this dissertation, we combine the plasmonic and organic technologies onto the silicon photonics platform to create silicon plasmonic organic structures and investigate the nonlinear effects induced in them. Silicon plasmonic organic structures combine the advantages of silicon with ultra-compact performance of plasmonics and ultrafast property of organic materials that have great potentials in nonlinear integrated optics.

A full-vectorial nonlinear coupled-wave equation model which is valid for lossy plasmonic waveguides is proposed and then utilized to analyze the nonlinear effects in silicon plasmonic waveguides. This dissertation addresses the use of two kinds of plasmonic waveguides, plasmonic slot waveguide (PSW) and hybrid plasmonic waveguide (HPW), for nonlinear applications. Specifically, enhanced conventional and electrically induced second harmonic generation and optical rectification effect in PSW and enhanced second harmonic generation in HPW and ring resonators are proposed. The mode phase matching technique is applied for the phase matching of the nonlinear processes. Based on the effective nonlinear effects within short distances, possible applications in optical signal processing such as phase regeneration, modulation and detection are envisaged.

Design, fabrication and measurement of PSW are also provided. By spin-coating a commercially available second order nonlinear polymer, preliminary results regarding the nonlinear response of the PSW are investigated.